Two-Photon Spectroscopy of Trapped Atomic Hydrogen

by

Claudio Lenz Cesar

Submitted to the Department of Physics
in partial fulfillment of the requirements for the degree of

Doctor of Philosophy

at the

MASSACHUSETTS INSTITUTE OF TECHNOLOGY

November 1995

Author . . . .
Department of Physics
November 30, 1995

Certified by . . . .
Daniel Kleppner
Lester Wolfe Professor of Physics
Thesis Supervisor

Accepted by . . . .
George Koster
Chairman, Graduate Committee

Two-Photon Spectroscopy of Trapped Atomic Hydrogen

by

Claudio Lenz Cesar

Submitted to the Department of Physics
on November 30, 1995, in partial fulfillment of the
requirements for the degree of
Doctor of Philosophy

Abstract

We have performed two-photon laser spectroscopy on the 1S-2S transition in trapped atomic hydrogen. The measured linewidth allows for *in situ* determination of the sample temperature. We predicted and observed transitions between trap states due to momentum transfer between the laser intensity profile and the quantized atomic motion perpendicular to the laser beam. In this regime, with the appearance of sidebands, the resolution is no longer limited by time-of-flight and we have achieved fractional spectral resolution of 1.7×10^{-12}, limited by laser jitter. We have also measured 2S decay lifetimes around 110ms, close to the natural radiative decay time of 122ms. The estimated sensitivity should allow us to detect as few as 10^7 Bose-Einstein condensate atoms with the present apparatus.

Thesis Supervisor: Daniel Kleppner
Title: Lester Wolfe Professor of Physics

... and Jacob served 7 years

for Rachel ...

... I dedicate these 7 years

to Raquel for her love, strength and support ...

Acknowledgments

This work is far from being the result of a single man's work or even one group's generation. In order to keep this short I will mention only the people with whom I interacted directly.

I thank Dan Kleppner and Tom Greytak for their support, open-mindness and presence, especially in the last hard years of this work. I credit Dan Kleppner for trying to make this dissertation a readable, "scientifically correct", document.

Working with John Doyle, Jon Sandberg and I.Albert Yu in the first half of this work was a pleasant, learning experience. Mike Yoo always had the perfect joke or story to end our lunch.

The true essence of a group that I received, I tried to pass along to the second generation. Dale Fried, Adam Polcyn and Tom Killian, with their dedication and good work made it possible to obtain the experimental data in this thesis. I will definitely remember the hamock that Dale setup in the lab, where we used to take turns between measurements in the all-night/day runs. A. Nick Marden will bring more joy to the group and I recomend presenting him with the group's "golden" symbol after his oral exam. Good luck, and let me know when you achieve BEC. Jon Goldman worked very hard with us for a summer.

Peggy Berkowitz is a very special and supportive friend. Carol Costa, you are incredibly efficient and it was great to count with your support. Janet Sahlstrom, quite an artist, didn't we have a good time talking about life at MIT?

The friendship with Michael Faas, Tineke, Reiko Oda and Laurent Lellouch will

make this world small. I will always remember the fun we had in that active social life. Reiko, you are quite special and I am sure we will be meeting many times throughout the planet.

After a long unsocial period we had the pleasant surprise of meeting Misha and Tania Brodsky and Olivier and Gretchen Klein. I am sure we will have more time together, far from this place. Gretchen you are brilliant in your creations and we hope to be reading about this young artist who takes over Paris (and, of course, Brasil) in the years ahead.

I also would like to thank Beatrice Kleppner and Betsy Greytak for the good times in their places. Sharon Peled, keep up with the "force" and you will finish your PhD and we will waiting for you to celebrate.

When we used to be active members of the Brazilian club at MIT we cultivated many special relationships. Among those are Isabel e Manuel Conde, Rodrigo Paiva, Manuel Cruz, Monica Rocha, Cecilia Hedin-Pereira, Susandeise e Juliana Puga. I am glad a new generation is keeping the BSA alive and better than ever, Marcos Gurgel, Marysilvia e Rodrigo Capaz, Claudio Chammon, Gladis and many new people that I didn't even have the chance to meet.

We are glad for having met so many special brazilians in the church. Ruy and Martha Costa, Alderi Matos, Neuza e Divino Rosa, Sonia, Isabel, Claudette e Nelson, Claudete, Zelita and so many others. Ruy e Martha, brazil waits for you. We will always remeber Bart and Priscilla Kelson and Octavio Lima and Kristy. Octavio preached inspired sermons with an experimental approach to faith. Isabella and Esdras, despite your protest, we still think you are the most uncomplicated people

we met in Boston. Keep that violin sounding heavenly.

Jose Rios Leite has always been a source of encoragement.

CNPq has financed the first half of our time in this country. ETFCE, and our many friends there, have provided me with an incredible support, and our ties with this school will last while we last.

Raquel's mother, Ana, spent a good time with us taking care of the kids. My parents, Homero e Hulda Lenz Cesar, not only gave us (their kids) love, attention and support, but spent a long time tutoring us personally. I wish we (I and Raquel) will be able to do the same for Lucas and Leticia. Lucas and Leticia, you have given me the experience of a special love. Even though these have been two tough years, we will make it up for you.

With the many arrangements for a long trip back home, I am sure that I forgot to mention many names and I will be ashamed when I remember those names (this is actually going to happen in the airplane). I apologise a priori.

Hope to see you all very soon,

Claudio Lenz Cesar

Contents

List of Figures

Chapter 1

Introduction

This chapter starts with a discussion of research with cold hydrogen including recent work in our laboratory. Next, we present a historical perspective on this experiment including a background on trapping, cooling, and detection of spin-polarized hydrogen. This will lead us to the subject of this dissertation — two-photon spectrocopy of trapped hydrogen. An overview of the experimental and theoretical developments reported in this thesis is presented. The last section outlines the organization of this dissertation.

1.1 Why study Hydrogen?

There is little contention among physicists about the central role played by the study of hydrogen on the development of modern physics. The examples range from Bohr's quantization rules to the development of quantum electrodynamics, which was motivated by the discovery of the Lamb shift. Because it is so simple and can be used to

test the basic theories of physics, "hydrogen" and "fundamental physics" are considered synonymous in a physicist's thesaurus. And indeed, hydrogen is the best studied atom in nature.

It is then acceptable, if not obvious, to ask a modified version of the question above: why do we still bother to study hydrogen when we already know so much about it? As we will see, research with cold, spin-polarized, hydrogen has opened new frontiers in the study of fundamental physics[1, 2, 3]. The range and depth of this research is astounding as I shall illustrate with only two examples involving recent developments in our laboratory.

Recent progress in lasers and experimental atomic techniques have made it possible to measure the 1S-2S transition frequency in hydrogen to high precision allowing an accuracy on the Rydberg constant of a few parts in 10^{11} [4, M.Weitz, et al.; and B.de Beauvoir, et al. By simultaneously comparing it with the 2S-4P (or 2S-4S,D) transition frequency, the Lamb shift for the 1S state has been determined to 5 parts in 8×10^5[5, 6]. Discrepancy between theory and experiments prompted a theoretical effort to evaluate additional corrections in the QED calculation[7]. These experiments also pointed out the significance of inconsistencies between measurements of the proton radius. Lattice QCD may be able to predict the proton radius[5]. In this case the hydrogenic spectrum may become a test bed for QCD.

Although progress in hydrogen spectroscopy has been impressive, the $0.65 Hz$ natural linewidth of the 1S-2S two-photon transition (@243nm) is still far from being realized. Transit-time, or time-of-flight, has been the dominant broadening mechanism in atomic beam experiments. The work described in this thesis represents a new era in

the spectroscopy of this transition. With trapped atoms, time-of-flight broadening is no longer a fundamental limit to the resolution. We have provided a theoretical prediction for the elimination of time-of-flight broadening. We have confirmed the prediction experimentally and have observed the highest reported resolution on the 1S-2S two-photon transition [4, see reports by Cesar, et al.; Biraben, et. al.; and Weitz, et. al. in]. Most importantly, we have demonstrated the potential for orders of magnitude improvement beyond our current resolution, which is limited by laser frequency jitter. Resolution close to the natural linewidth of the 1S-2S transition, with a large signal to noise ratio, should be possible. This would have profound implications to the fundamental measurements described above, and also to frequency standards and metrology.

The research towards high resolution spectroscopy of hydrogen is symbiotic with, and a consequence of, the pursuit of Bose-Einstein condensation(BEC) in hydrogen. While BEC requires low temperatures, the spectroscopy benefits from low temperatures through the narrowing of the lines and decrease in all systematics. Through the sensitive and accurate probing of spectroscopy we hope to detect BEC in our sample of spin-polarized hydrogen.

Research towards BEC in weakly interacting systems started many years ago in spin-polarized hydrogen. The development of forced evaporative cooling in our laboratory revolutionized the achievement of low temperatures. Three groups recently reported on the observation of BEC in alkalis using the techniques of laser cooling followed by evaporative cooling in alkalis[8, 9, 10]. With the developments reported in this thesis our group is now in a position to observe and study BEC in hydrogen.

Once BEC is generated in our lab we should be able to study such phenomena as superfluidity, collisions, and coherent atomic beams. The observation of BEC in weakly interacting atomic systems is the beginning of a new and exciting era in physics with implications across the boundaries of physics.

1.2 Background on Trapping, Cooling and Detection of Hydrogen

A thorough description of trapping, cooling and bolometric detection in our system can be found in the thseis of John Doyle[11]. Here I give a brief overview.

Atomic hydrogen can be stabilized against forming molecules by polarizing its spins. The prediction, by W.Stwalley and L.Nosanow[12], that polarized hydrogen would remain gaseous as $T \to 0$ ignited the experimental efforts to generate BEC at high densities ($10^{19}cm^{-3}$). The research employed atoms in the b-state ($H \downarrow$), one of the hyperfine states of hydrogen in its ground electronic state (see Fig. 1-1). These attempts at generating BEC with high compression of $H \downarrow$ eventually failed due to surface and three body recombination.

At that time, to overcome these problems, Harald Hess[13] proposed trapping and evaporatively cooling $H \uparrow$, hydrogen in another hyperfine state (see Fig. 1-1). $H \uparrow$ is a low field seeker and it can be trapped in a static magnetic field configuration with a minimum in free space. A trap provides thermal decoupling from the walls. It can allow the achievement of extremely high temperatures, as in the case of plasmas, or extremely low temperatures, as in our case.

Unfortunately, hydrogen does not have a convenient laser line for optical cooling like the alkalis. Therefore one must rely on cryogenic techniques to load the trap. The important parameters for the loading of such a trap are the magnetic energy and the nature of elastic and inelastic collisions among atoms and between atoms and surfaces.
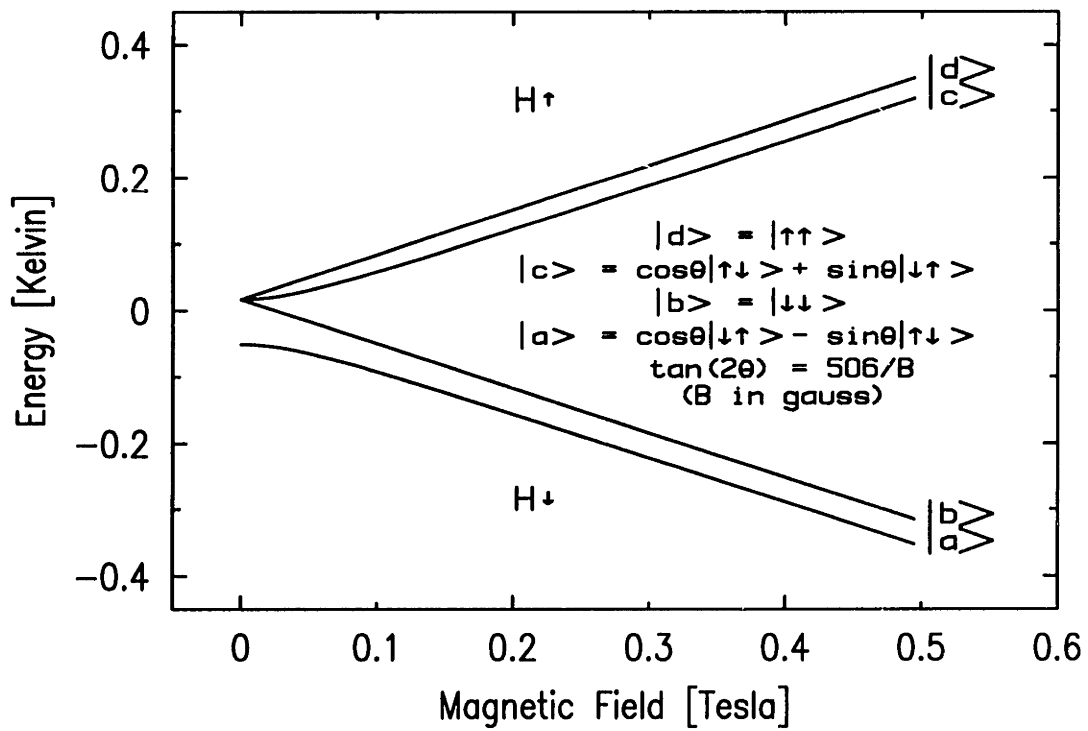
Figure 1-1: Hyperfine diagram for the 1S state of hydrogen. The first arrow in the ket represents the electron spin and the second labels the proton spin. $|d> \Rightarrow H \uparrow$ is the low field seeker state that we trap.

The energy of hydrogen in the ground electronic state is shown in Fig.1-1, as a function of the magnitude of the magnetic field. For the d-state, the one we trap, the energy is essentially μB, where the Bohr magneton $\mu_B = 5.051 \times 10^{-24} erg/gauss$. A more convenient unit for our purpose is the characteristic temperature-field combination $T = \mu_B B/k = 67.2(B/gauss)\mu K$. With current superconducting magnet technology, trapping fields of over $1T$ are routinely achieved, permiting a trap depth of $0.67K$.

In order to obtain enough atoms at temperature lower than $0.67K$ one has to start with a reasonably cold sample as required by the Boltzmann distribution. For temperatures below $10K$, hydrogen would imediately stick to any surface except liquid He. These considerations led to a technology in which a cell with a wall temperature of $100mK$ is coated with superfluid ^4He, in an apparatus cooled by a He dilution refrigerator.

The magnetic trap, in a Ioffe-Pritchard[14] configuration, consists of linear quadrupoles, confining the atoms in the radial direction, and pinch coils for axial confinement (see Fig.1-2). An axial bias solenoid provides control of the minimum field in the trap center. Avoiding a field zero in the trap is important to prevent atom loss through non-adiabatic depolarization of their spins ("Majorana flips").

The atoms are produced in an RF discharge. Atoms in the d-state are caught in the trap by dissipating their energy in collisions within the gas and with the wall. After loading, the sample is cooled by forced evaporation, that is, hot atoms are slowly allowed to escape from the trap while the sample thermalizes. By varying the shape of the trap as the sample cools, the density can be controlled independently of
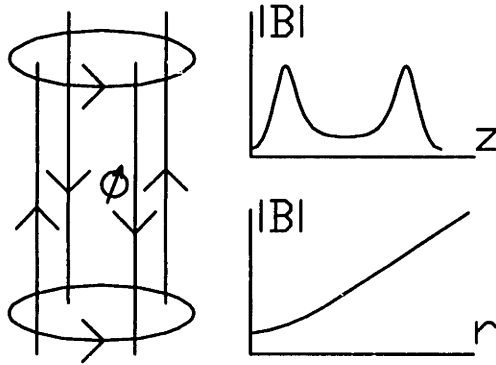
Figure 1-2: Sketch of the Ioffe-Pritchard magnets configuration. Bias magnet not shown.

the temperature allowing the system to follow different paths in $n - T$ phase space. We typically obtain $10^{10} - 10^{12}$ atoms at temperatures ranging from $< 50\mu K - 40mK$ at densities of $10^{12} - 10^{14} cm^{-3}$.

In order to detect the atoms we have employed a bolometric technique that detects recombination heat $(H + H \rightarrow H_2 + \Delta E)$ from atoms that have escaped the trap into a zero field region (where recombination is possible). We measure the energy distribution of the atoms by recording the power deposited onto the bolometer as we lower the trap threshold energy linearly in time. By fitting the energy distribution to a Maxwell-Boltzmann distribution we can assign a temperature to the sample.

Although the bolometric detection is simple, elegant and sensitive, it fails at very low temperatures. At temperatures below $100\mu K$, signal/noise becomes a serious limitation and we encounter atom escape time problems. The finite time it takes for the atoms to leave the trap once they are above threshold becomes incompatible with the requirements for a dump time faster than the thermalization time. The bolometer is also inapropriate for the detection of BEC. The fact that this detection requires

effectively destroying the trap is also not compatible with the detection of the trap's ground state population, especially when considering the escape time problem.

Therefore, there was a need for a better detection system. The spectroscopic detection is described next.

1.3 1S-2S Two-Photon Spectroscopy of Trapped Hydrogen: Overview and Current Status

In principle, high-resolution laser spectroscopy has a number of features that make it the most desirable detection technique for this trapped sample. It allows for "in situ" measurement of the atoms in the trap. With a high sensitivity, few atoms need to interact with the laser, meaning low destructiveness. The sensitivity actually increases as the temperature decreases and as density increases, which means better signal/noise as BEC is approached. With high resolution, an accurate measurement of temperature is possible. The two-photon character of this transition should allow for a clear signature of the transition and unique spectroscopic measurements as we later discuss. Adding to all these benefits, there are numerous spectroscopic experiments that can be performed in this system. In addition the system has the potential for a new frequency standard.

I shall quickly describe the major features of experiment while leaving the details to chapter 5. The levels diagram is depicted in Fig.1-3. The metastable $2S$ level has two wonderful features for a fluorescence experiment: it decays fast if an electric field
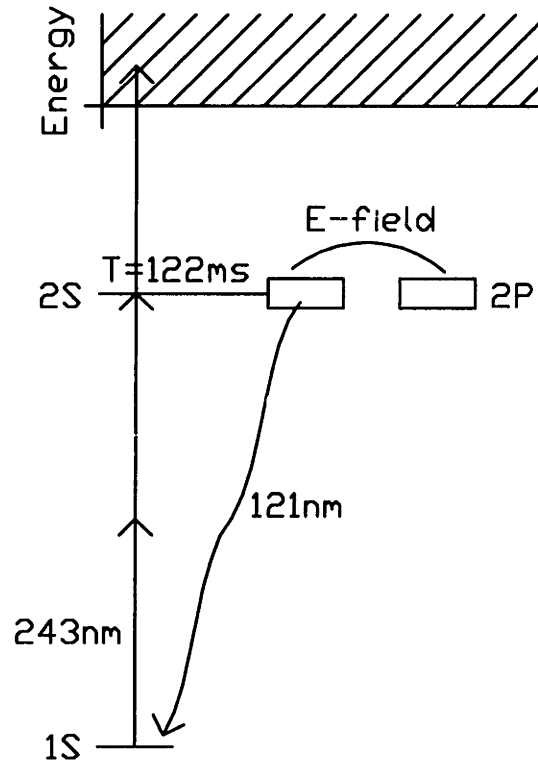
Figure 1-3: Electronic levels of interest. The quenching E-field broadens the 2S state and cause it to decay fast by emission of a Lyman$_\alpha$ photon. Photoionization of the 2S is of concern for high resolution spectroscopy. Not shown is the small change in 1S-2S transition frequency due to magnetic field.

is applied, and the emitted radiation is at twice the excitation frequency. These two features are explored in time and frequency descrimination.

The 243nm CW laser beam is passed along the axis of the trap and retro-reflected to produce the standing wave required for Doppler-free excitation. The beam is switched on and off and the quenching E-field is applied. The resulting Lyman$_\alpha$ fluorescence is detected by a micro-channel plate (MCP), with an overall efficiency of 5×10^{-6}, and recorded in a counter. By scanning the laser frequency we generate a spectrum that can be used to obtain information about the sample.

With a time-of-flight broadened spectrum, the linewidth is determined by the time

it takes an atom with energy kT to cross the laser beam waist. Therefore, in this limit, the linewidth measures the sample temperature. Indeed, we have succesfully measured sample temperatures from the spectral linewidths, obtaining good agreement with the bolometric technique down to $200\mu K$. Currently, our laser has a frequency jitter that fluctuates at about $2kHz$ which prevents us from consistently measuring temperatures below $200\mu K$. Doppler shift between different parts of the apparatus may be fully responsible for this jitter. We are presently addresing this issue.

While this laser frequency instability prevents us from diagnosing our path down to BEC, it would not prevent us from detecting a condensate with more than 10^7 atoms. As expected, we have observed large increases in signal/noise as we approach the conditions for BEC and are able to detect atoms optically when the bolometer signal had already disapeared under its noise floor.

The time-of-flight spectrum is a result of the atomic motion transverse to the laser beam. With atoms confined in a trap, one should treat their translational motion quantum mechanically. This is essential when the energy separation between adjacent trap levels becomes comparable to the experimental resolution. We should, a priori, expect the semiclassical result to be a limiting case of this quantum mechanical treatment.

We have treated this problem in Chapter 2. The quantum treatment brings about the picture of momentum transfer between the laser beam intensity profile and the translational motion of the atoms. By absorbing the photons the atoms jump from one trap state to another trap state. The cost in energy for this transition is provided by the photons, resulting in a shift of the resonant frequency for this particular transition.

If the trap is harmonic, transitions between trap states result in an energy change that is a multiple of the trap oscillation frequency. The result of these calculations is that the spectrum is composed of multiple lines - i.e. it displays sidebands. The underlying envelope of these lines is a typical time-of-flight broadened spectrum. In this quantum regime, time-of-flight is no longer a limitation and one can achieve close to natural linewidth. These predictions were confirmed experimentally as we show in Chapter 5. Under this regime, we were able to obtain the highest resolution reported to date on this line.

We have also treated the small Zeeman effect on the 1S-2S transition using this quantized formalism. This formalism makes these calculations simple and we have computed spectra predicting the broadening and shift of the line for a given set of parameters. This calculation will come handy when our laser system is capable of resolving 20Hz lines.

We have addressed the issue of two-photon spectroscopy of BEC. We have calculated the enhancement of spontaneous emission due to the condensate and found it to be very small. Therefore, we expect to observe high resolution structures in the spectroscopy of the condensate. A new idea for cooling a hypothetical atom into the condensate (of the same species) is also presented.

We have measured 2S decay lifetimes of the order of the natural decay lifetime, and we have performed some saturation studies. We have also attempted to measure a density shift of the line, as a recent prediction suggests[15] but were unable to. Most of these measurements are not worth refining until the laser jitter is minimized. When that happens, all these studies can be pursued in a reliable and precise way.

This dissertation is organized as follows. This Chapter (1) provides an overview of this research. In Chapter 2 we quantize the atomic motion in the trap and develop a formalism to compute the 1S-2S Doppler-free lineshapes. We also consider the Zeeman effect on the 1S-2S transition. A calculation regarding two-photon spectroscopy of the Bose condensate is carried out in Chapter 3. A discussion about photoionization and saturation completes Chapter 3. The experimental setup and operation is described in Chapter 4. Data is presented and discussed in Chapter 5. Chapter 6 concludes and suggests future implementations.

Chapter 2

Spectroscopy of Quantized Trap

States

We consider the effect of atomic motion tranverse to the laser beams in two photon Doppler-free spectroscopy. We reinterprete the time-of-flight broadening mechanism in terms of momentum exchange between the laser intensity profile and the atomic motion. This momentum transfer is quantized in the case of trapped atoms. The formalism is developed for the case of gaussian laser beams and harmonic traps, but it can be easily modified to account for other configurations. The computed spectra show quantized features that should be easily seen experimentally provided that the trap oscillation frequency can be made bigger than the typical dephasing rates and experimental resolution. As a practical application we compute the spectral lineshapes for hydrogen trapped in an inhomogeneous magnetic field where we take into account the small difference in magnetic moment between the $1S$ and $2S$ states.

2.1 Introduction

Cooling and trapping of atoms and ions has become a major subject of research in atomic physics. The goals include the study of cold collisions and collective quantum behavior[1, 8, 9, 10, 16], high precision spectroscopy, the development of improved standards, and tests of fundamental theories of physics.

These trapped atoms and ions are often studied by optical spectroscopy, and in order to understand the spectra one has to account for the effect of the trap on the lineshape. The trapping potential affects the translational (external) motion of these trapped particles and in the case of neutral atoms the trapping fields directly affect the electronic (internal) energy states. The trap energy level spacing, for most neutral atom traps, is usually much smaller than the optical transition linewidth. In those cases, the external motion of the atoms can usually be treated classically. For trapped ions however, the energy separation between adjacent trap states can be easily resolved with narrow transitions[17, 18]. In this case it is clear that quantization of the external motion is required.

The translational motion of the particles gives rise, in a semiclassical treatment, to time-of-flight broadening which is usually the dominant broadening mechanism in two-photon Doppler-free spectroscopy. The time-of-flight broadening comes about due to the finite time an atom takes to cross the laser beam. This sampling time results in a broadening of the frequency spectrum of the laser as "seen" by the atom. The semiclassical calculation of the time-of-flight Doppler-free two-photon spectroscopy lineshape was originally carried out by C.Bordé[19]. Biraben et. al.[20]

showed that this broadening is given by the Fourier transform of the time varying laser intensity as seen by the atom.

Hydrogen, being light, has a relatively high oscillation frequency in a weak magnetic trap compared to the natural linewidth of the dipole forbidden $1S - 2S$ transition. Consequently, quantum effects associated with the translational motion in the trap are important. When an atom, in a well defined trap eigenstate, absorbs photons it will either stay in the same trap eigenstate or make a transition to another eigenstate. In the latter case there will be a shift in the spectral line caused by the change in translational energy. The different set of allowed translational transitions results in a spectrum made up of a "comb" of lines. These discrete lines resemble Ramsey fringes, and in fact they have much in common. One can think of these trapped atoms as bouncing back and forth through the laser beam. If coherence is not lost between trips the spectrum will contain interference fringes. Dephasing mechanisms due to trap perturbations or collisions, for example, broaden not only the internal energy levels but also the trap eigenstates. If this broadening becomes comparable to the level separation then it no longer make sense to talk about a trap eigenstate. In this case the fringes are not visible and the spectrum looks like a single broad line.

This work gives a quantitative description of the lineshape of two-photon Doppler-free spectroscopy of trapped atoms. In addition, it provides a novel physical picture for the phenomenon of time-of-flight broadening. In the following sections we describe the system of interest and state our basic assumptions. Using perturbation theory we then calculate the probability of exciting an atom from any given trap state. We compute single atom spectra and the spectra of a thermalized sample. We conclude by
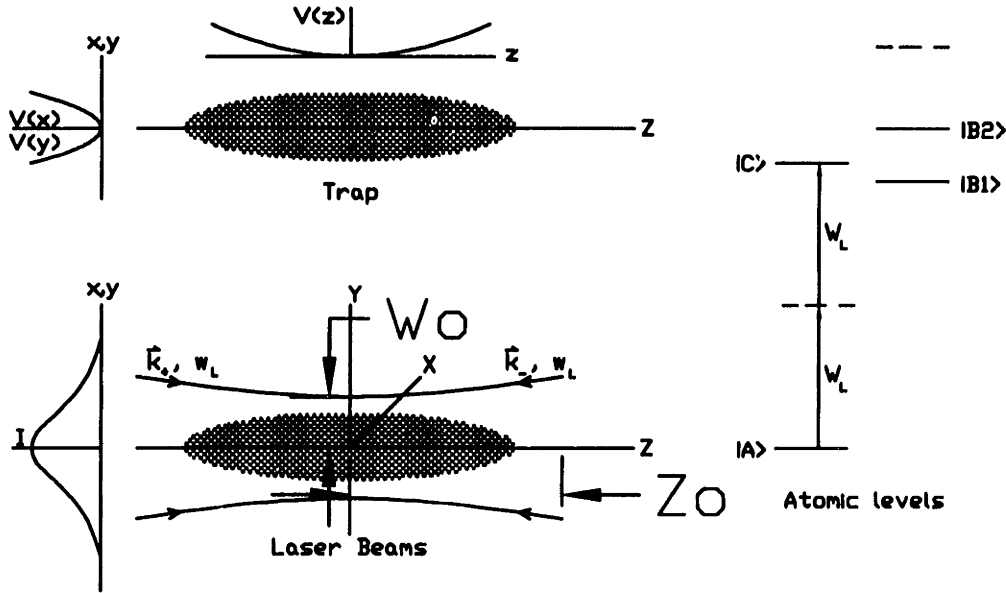
Figure 2-1: Laser beam, trap shape and internal atomic energy levels.

applying the formalism to the particular case of magnetically trapped spin-polarized hydrogen.

2.2 The system and basic assumptions

Our system consists of a cloud of atoms, trapped in a harmonic potential well. These atoms are excited by two-photon absorption from a laser beam propagating along the axis of the trap as shown in Fig.2-1. The states of concern are the ground state $|A>$, intermediate states $|B>$ and final state $|C>$. The electric dipole matrix elements vanish between $|A>$ and $|C>$ but have the values μ_{ab} and μ_{bc} between these states and the intermediate states. We assume a large one-photon detuning so that real transitions from $|A>$ to $|B>$ do not occur.

It is convenient to describe the center-of-mass motion using Cartesian coordinates

with translational states $|n_x, n_y, n_z>$, where n_x, n_y, and n_z are quantum numbers. We assume the trap to be harmonic and cylindrically symmetric. The hamiltonian for the atom's center of mass motion is

$$H_{cm} = \sum_{j=x,y,z} [\frac{P_j^2}{2m} + \frac{1}{2}m\Omega_j^2 R_j^2] = \sum_{j=x,y,z} \hbar\Omega_j(n_j + 1/2) \qquad (2.1)$$

where $\Omega_x = \Omega_y \equiv \Omega$ is the radial angular frequency. We introduce the parameter α:

$$\alpha \equiv \sqrt{m\Omega/\hbar} \qquad (2.2)$$

α is related to the rms size of the wavefunctions: $< x_j^2 >^{1/2} = \sqrt{j + 1/2}/\alpha$. The rms momentum is $< p_j^2 >^{1/2} = \hbar\alpha\sqrt{j + 1/2}$.

The laser beam is taken to be gaussian, monochromatic and linearly polarized. The beam propagates along the z axis and has a minimum waist at $z = 0$ with a waist radius w_0. The beam area is twice its minimum value at $z = \pm z_0$, where z_0, the divergence length, is given by $z_0 = \pi w_0^2/\lambda$. To carry out Doppler-free spectroscopy the beam is retro-reflected onto itself. We identify the fields propagating in the $+z$ and $-z$ directions by E_+ and E_-, respectively. The spatial dependence of the field amplitude is[21]:

$$E_+(r,z) = E_{0_+} \frac{w_0}{w(z)} exp\left(i[kz + \eta(z)] - r^2 \left[\frac{1}{w^2(z)} - \frac{ik}{2R(z)} \right] \right) \qquad (2.3)$$

where,

$\eta(z) = tn^{-1}(z/z_0)$, $w^2(z) = w_0^2[1 + z^2/z_0^2]$, $R(z) = z(1 + z_0^2/z^2)$. $E_-(r,z)$ is

obtained by exchanging z with $-z$ in the expressions above.

The radiation field is treated classically and the broadening due to spontaneous

emission and other sources is introduced phenomenologically through a normalized

lineshape. We assume, for now, that the electron energy levels are unaffected by the

trapping potential. In Section 2.6.1 we will treat the specific case of magnetically

trapped hydrogen where there are small energy shifts due to the trapping field.

The atom-radiation interaction hamiltonian in the dipole approximation, keeping

only the frequencies responsible for absorption, is:

$$V(\vec{r},t) = \sum_{j=+,-} \frac{1}{2}\vec{\mu}_{op} \cdot \vec{\epsilon} E_j(r,z)e^{-i\omega_L t} \qquad (2.4)$$

where μ_{op} is the electric dipole moment operator, $\vec{\epsilon}$ is the beam polarization, and

ω_L is the laser frequency. To simplify the notation we will drop the vectorial form.

2.3 Perturbation theory - low intensity

Applying perturbation theory to second order in the E-field, and using the interaction representation, we obtain the amplitude for the transition from $|A, j>$ to $|C, f>$ (where index j or f, represents a set of 3 indexes to describe x, y, z):

$$C_{j \to f}^{(2)}(t) = \sum_{b,n} \frac{A_j^{(0)}}{(i\hbar)^2} \int_0^t dt'' \int_0^{t''} dt' e^{i(\omega_{cb} + \Omega_{fn})t''} e^{i(\omega_{ba} + \Omega_{nj})t'} \times$$

$$< C, f|V(\vec{r}, t'')|n, B >< B, n|V(\vec{r}, t')|j, A > \qquad (2.5)$$

where $\omega_{nm} \equiv (E_n - E_m)/\hbar$ is the electronic transition frequency, and similarly for the trap states transition frequency Ω_{nm}. $A_j^{(0)}$ is the amplitude of the initial population in the level $|j, A >$. To simplify the notation we shall drop the superscripts indentifying the order of the perturbation and use superscripts to identify the final state of the transition. Evaluating the electron dipole matrix elements we obtain:

$$C_j^f(t) = \sum_{b,n} \frac{A_j \mu_{ab} \mu_{bc}}{(i\hbar)^2} \int_0^t dt'' \int_0^{t''} dt' e^{i(\omega_{cb} + \Omega_{fn} - \omega_L)t''} e^{i(\omega_{ba} + \Omega_{nj} - \omega_L)t'} \times$$

$$\frac{1}{4} < f|(E_+(\vec{r}, z) + E_-(\vec{r}, z))|n >< n|(E_+(\vec{r}, z) + E_-(\vec{r}, z))|j > \qquad (2.6)$$

Because of the large detuning of the intermediate state $|B>$, the only important

contributions to $C_j^f(t)$ ocur when $t' \approx t''$ [22]. Thus, we substitute $\Omega_{fn}t'' + \Omega_{nj}t' \approx$

$\Omega_{fj}t''$ and use the closure relation on the intermediate trap wavefunctions, $(\sum_n |n><$

$n| = 1)$, to eliminate these states. For the Doppler-free case, which involves the

absorption of two counterpropagating photons, we disregard the products of fields

from the same beam. We then obtain:

$$C_j^f(t) = \sum_b \frac{A_j \mu_{ab} \mu_{bc}}{(i\hbar)^2} \int_0^t dt'' \int_0^{t''} dt' e^{i(\omega_{cb} + \Omega_{fj} - \omega_L)t''} e^{i(\omega_{ba} - \omega_L)t'} \times$$

$$\frac{1}{4} < f|2E_+(\vec{r}, z)E_-(\vec{r}, z)|j > \tag{2.7}$$

Spelling out the three indexes for x, y, z we substitute $|j> \rightarrow |j, k, l_z>$ and

$<f| \rightarrow <h_z, g, f|$. Substituting Eq. 2.3 for the fields and performing the time integrations we obtain:

$$C_{jkl}^{fgh}(t) = \sum_b \frac{A_{jkl} \mu_{ab} \mu_{bc}}{(i\hbar)^2} \frac{1}{i(\omega_{ba} - \omega_L)} \frac{e^{i(\omega_{ca} + \Omega_{fj} + \Omega_{gk} + \Omega_{hl} - 2\omega_L)t} - 1}{i(\omega_{ca} + \Omega_{fj} + \Omega_{gk} + \Omega_{hl} - 2\omega_L)} \times$$

$$< h_z | \left[< f|e^{-2x^2/w^2(z)}|j > \frac{E_{0+}E_{0-}w_0^2}{2w^2(z)} < g|e^{-2y^2/w^2(z)}|k > \right] |l_z > \tag{2.8}$$

The line shape is governed by the transitions between vibrational states, with a

probability given by the matrix elements above, accompanied by the respective energy changing terms Ω_{fj} and Ω_{gk} . These matrix elements are separable in x, y because we have assumed a separable potential and aligned the laser along the trap axis. Note that if the beams were slightly misaligned we would need to modify these matrix elements by adding a factor $e^{i\Delta\vec{k}\cdot\vec{r}}$ as a first order correction. The x-direction matrix element is

$$I_j^f \equiv < f|e^{-2x^2/w^2(z)}|j > .$$ (2.9)

We turn now to the underlying physical processes contained in Eqs. 2.8 and 2.9.

2.4 Momentum transfer, selection rule and limiting cases

If $|j >$ and $|f >$ were free-particle states with momenta p_j and p_f, respectively, we could rewrite Eq. 2.9 as

$$I_j^f \propto \int dx e^{-i(p_j-p_f)x/\hbar} e^{-2x^2/w^2(z)}$$ (2.10)

It is evident that I_j^f is the spatial Fourier transform of the beam profile at momentum $p_j - p_f$. When we consider the complete set of j's and f's, we are decomposing

the beam profile into its momenta components. Each component contributes to absorption at a frequency shifted from the electronic transition frequency ω_{ca} by an amount Ω_{fj}. If the translational energy is not quantized the wavefunctions would be part of a continuum and the continuum of frequency shifts would produce a single broad line. Atoms spatialy confined, however, absorb in a discrete series of lines. Averaging over all atoms in a sample may, however, wash out the discrete features if the atoms have varying resonant frequencies or if the trap level spacing is not constant.

We can extract the selection rules for the transitions in Eq. 2.9 by simple parity conservation. The gaussian function in the matrix element I_j^f has even parity, implying that $|f>$ and $|j>$ should have the same parity for $I_j^f \neq 0$. This means that f and j must be separated by twice an integer, i.e., $f + j$ =even.

If the laser beam waist w_0 is much larger than the physical extent of either $|j>$ or $|f>$, i.e., $w_0 \gg \sqrt{(f,j)+1/2}/\alpha$, the gaussian function in the matrix element of Eq. 2.9 is approximately constant and equal to unity. In this case:

$$I_j^f = <f|j> = \delta_{j,f} \tag{2.11}$$

Because there is no change in the vibrational state, no sidebands arise from this transition. Consequently, in this limit, there would be no transit time broadening. The situation is closely related to Dicke narrowing, in which motional broadening is supressed if the atom is confined and cannot experience the spatial phase change of the electric field.

At the other extreme, if the beam waist is much smaller than the spatial extent of the wavefunctions, the gaussian factor behaves like a normalized delta-function. So, for an atom initially in state $|j>$, the number of possible transitions to different final states $|f>$ is enormous. Each of these transitions ocurs at a different frequency in quantized steps of 2ω. This situation results in a fine comb-like structure of lines within a broad envelope. The envelope shape will be calculated below. These limiting cases will ocur naturally as a result of the general solution to Eq. 2.9 that we develop in the next section.

2.5   General Behaviour

We develop an exact solution to Eq. 2.9 in Section 2.8. As is often the case, the exact solution hides the interesting physics. Furthermore, it is not computationaly useful in the case of large quantum numbers because it involves factorials. For these reasons we prefer to work with an approximate solution for Eq. 2.9 that is developed in Section 2.8.1.

The potential, being almost flat at the origin, causes the eigenfunctions to look like free-particle solutions. Consequently, the harmonic potential wavefunctions near the origin have a sinusoidal character. The physical picture of momentum transfer and spatial Fourier transform of the laser beam developed in the previous section is still appropriate within this approximation. Using the result of Section 2.8.1, the translational matrix element becomes

$$< f|e^{-2r^2/w^2(z)}|j > = \frac{\alpha w(z)e^{-\frac{\alpha^2 w^2(z)}{8}(\sqrt{2j+1}-\sqrt{2f+1})^2}}{[4\pi^2(2j+1)(2f+1)]^{1/4}}\delta_{(j+f=even)}. \qquad (2.12)$$

The y matrix element has the identical structure. Substituting these in Eq. 2.8, and leaving it implicit, from now on, that $j + f$ and $k + g$ are even, we obtain an expression for the transition amplitude in terms of the z-translational motion matrix element

$$C_{jkl}^{fgh}(t) = \frac{A_{jkl}E_{0+}E_{0-}}{2(i\hbar)^2}\left[\sum_b \frac{\mu_{ab}\mu_{bc}}{i(\omega_{ba}-\omega_L)}\right]\frac{e^{i(\omega_{ca}+\Omega_{fj}+\Omega_{gk}+\Omega_{hl}-2\omega_L)t}-1}{i(\omega_{ca}+\Omega_{fj}+\Omega_{gk}+\Omega_{hl}-2\omega_L)}\times$$

$$\frac{(\alpha w_0)^2 < h_z|e^{-(1+z^2/z_0^2)\psi}|l_z >}{2\pi[(2j+1)(2f+1)(2k+1)(2g+1)]^{1/4}} \qquad (2.13)$$

We have substituted the expression following Eq. 2.3 for $w(z)$, in the exponent. Also we have introduced

$$\psi \equiv \frac{\alpha^2 w_0^2}{8}\left[(\sqrt{2j+1}-\sqrt{2f+1})^2 + (\sqrt{2k+1}-\sqrt{2g+1})^2\right] \qquad (2.14)$$

If the divergence length z_0 is much larger than the trap length we can substitute $< h_z|e^{-(1+z^2/z_0^2)\psi}|l_z > \approx e^{-\psi}\delta_{h_z,l_z}$. Even when this condition is not satisfied, z_0 will usually be long compared to the spatial oscillation of the axial wavefunctions. Con-

sequently, transitions among different longitudinal states will be negligible. Another way of thinking about this is to note that because we are using the Doppler-free configuration there is negligible momentum transfer along the axis of the beam. Consequently, the longitudinal matrix elements are all of the form

$$I_{z:l \to l} = <l|e^{-(1+z^2/z_0^2)\psi}|l>$$ (2.15)

This numerical factor can be estimated by assuming that the envelope of $|l>$ is constant over its extent ($\pm\sqrt{l+1/2}/\alpha_z$). The result is

$$I_{z:l \to l} = e^{-\psi}\left[\frac{\sqrt{\pi}}{2}\frac{erf(\zeta_l)}{\zeta_l}\right]$$ (2.16)

where erf() is the error function and

$$\zeta_l \equiv \frac{\sqrt{\psi(l+1/2)}}{\alpha_z z_0}$$ (2.17)

The expression in brackets in Eq. 2.16 above has the expected limiting behavior:

$$\frac{\sqrt{\pi}}{2}\frac{erf(\zeta_l)}{\zeta_l} \to 1 \quad as \quad \zeta_l \to 0$$

39

$$\frac{\sqrt{\pi}}{2}\frac{\mathsf{erf}(\zeta_l)}{\zeta_l} \to 1/\zeta_l \ \ as \ \ \zeta_l \to \infty$$

An alternative way to solve Eq. 2.15 is to expand the factorial in powers of $(z/z_0)^2$ and write z^2 in terms of lowering and raising operators, as we illustrate in Section 2.6.1.

Substituting Eq. 2.16 in Eq. 2.13 we obtain:

$$C_{jkl}^{fgl}(t) = \frac{A_{jkl}E_{0+}E_{0-}}{2(i\hbar)^2}\left[\sum_b \frac{\mu_{ab}\mu_{bc}}{i(\omega_{ba}-\omega_L)}\right]\frac{(\alpha w_0)^2 e^{-\psi}}{2\pi[(2j+1)(2f+1)(2k+1)(2g+1)]^{1/4}}\times$$

$$\frac{\sqrt{\pi}}{2}\frac{\mathsf{erf}(\zeta_l)}{\zeta_l}\frac{e^{i(\omega_{ca}+\Omega_{fj}+\Omega_{gk}-2\omega_L)t}-1}{i(\omega_{ca}+\Omega_{fj}+\Omega_{gk}-2\omega_L)} \tag{2.18}$$

The total population of level $|C>$ evolves as

$$|C(t)|^2 = \sum_{jfkgl} |C_{jkl}^{fgl}(t)|^2 \tag{2.19}$$

For a time long compared to the inverse of the natural (or broadened) linewidth, the time dependence of Eq. 2.19 behaves as $2\pi t\delta(\omega_{ca}+\Omega_{fj}+\Omega_{gk}-2\omega_L)$. In this case we can define a transition rate $W_{ajkl}^{cfgl} = d|C_{jkl}^{fgl}(t)|^2/dt$. We introduce a phenomeno-logical linewidth by assuming some distribution of ω_{ca} with full-width-half-maximum Γ_c described by a normalized lineshape function $g_{ajk}^{cfg}(\omega_L)$, i.e. $\int g(\omega)d\omega = 1$, and

40

centered at $\omega_{ca} + \Omega_{fj} + \Omega_{gk} - 2\omega_L = 0$. Integrating the δ-function convolved with $g_{ajk}^{cfg}(\omega_L)$ we obtain:

$$W_{ajkl}^{cfgl} = |\sum_b \frac{\mu_{ab}\mu_{bc}}{i(\omega_{ba} - \omega_L)}|^2 |\frac{E_{0+}E_{0-}}{2(i\hbar)^2}|^2 |A_{jkl}|^2 (\frac{\alpha^2 w_0^2 e^{-\psi}}{2\pi[(2j+1)(2f+1)(2k+1)(2g+1)]^{1/4}})^2 \times$$

$$(\frac{\sqrt{\pi}}{2}\frac{\mathsf{erf}(\zeta_l)}{\zeta_l})^2 2\pi g_{ajk}^{cfg}(\omega_L) \tag{2.20}$$

Naturally the trap oscillation features can only show up in the spectrum if Γ_c is narrow enough to resolve them.

2.6 Results

The lineshape can be found from Eq. 2.20. In evaluating it we will assume that the beam divergence length is longer than the sample, so that the term containing $\mathsf{erf}(\zeta)$ can be taken as unity.

As a first example, we shall recover the results of Biraben et al.(see Eq. 43 in Biraben, et. al.[20]), who treat the center-of-mass motion classically. They find that an atom moving transversely through the laser beam with velocity v_r contributes to absorption at a detuning $\delta = 2\omega_L - \omega_{ca}$ according to

$$W(\omega_L) \propto \frac{E_1^2 E_2^2}{v_r^2} \int_{-\infty}^{+\infty} d\zeta \frac{\Gamma_c}{(\zeta - \delta)^2 + \Gamma_c^2/4} exp[-\frac{\zeta^2}{4v_r^2/w_0^2}] \tag{2.21}$$

41

We recover their result as follows. If in Eq. 2.20 the quantum numbers contained in ψ (Eq. 2.14) are large, we can substitute $(\sqrt{2j+1} - \sqrt{2f+1})^2 \approx \frac{n^2}{2j+1}$, where $n = f - j$. Expressing the translational energy in terms of velocity we substitute $(2j+1) \rightarrow mv^2/(\hbar\Omega) = \alpha^2 v_x^2/\Omega^2$. We then have to sum Eq. 2.20 for all the transitions starting from state j (keeping the y-dimension constant) and finishing at state $j + n$ with a normalized lineshape function $g_{aj}^{c(j+n)}$

$$W(\omega_L) \propto (\frac{E_{0+}E_{0-}}{v_x})^2 \sum_n g_{aj}^{c(j+n)} exp(-\frac{(n\Omega)^2}{4v_x^2/w_0^2}) \qquad (2.22)$$

Taking $g_{aj}^{c(j+n)}$ to be Lorentzian, we substitute $g_{aj}^{c(j+n)} = \Gamma_c/[(n\Omega - \delta)^2 - \Gamma_c^2/4]$ to obtain

$$W(\omega_L) \propto (\frac{E_{0+}E_{0-}}{v_x})^2 \sum_n \frac{\Gamma_c}{(n\Omega - \delta)^2 - \Gamma_c^2/4} exp(-\frac{(n\Omega)^2}{4v_x^2/w_0^2}) \qquad (2.23)$$

which is essentially the same result as Eq.2.21 when one considers $n\Omega$ a continuous variable and substitute the sum for an integral.

In order to understand the thermal averaged spectrum we start by ploting single atom spectra in the limit of $\Gamma_c \rightarrow 0$. The single atom spectra in Fig.2-2 consider transitions between trap states in a single dimension. Such a hypothetical spectrum could be realized if the laser could probe individual atoms and if the trap were very tight in one dimension (so that the atom is confined to the laser beam in that dimension).
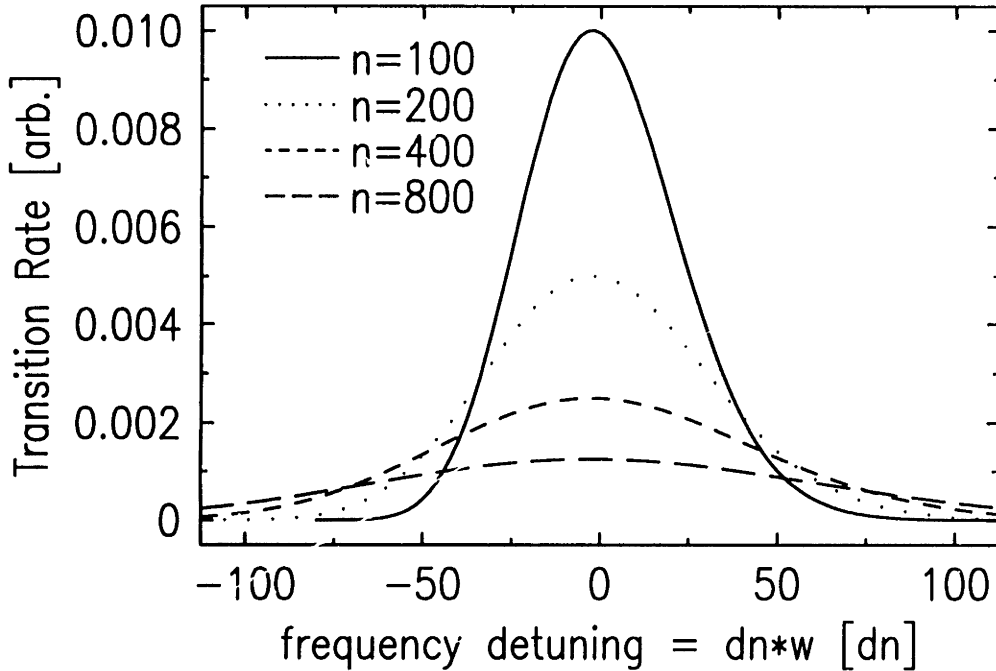
Figure 2-2: Single atom spectra for various starting quantum numbers as function of the change in quantum number. In this case $w_0 = 10\mu m$ and $\omega = 520 rad/s$. See text.

The plot shows transitions originating at $n = 100, 200, 400, 800$, with $\alpha w_0 \approx 0.91$. Notice the broadening with its decrease in peak amplitude as the quantum number increases. A larger quantum number is equivalent to an increase in velocity in the semiclassical picture.

The αw_0 product, which will appear in all the plots, is essentially the ratio of the laser beam waist to the trap ground state size, i.e., it is a figure of merit for the confinement of the ground state.

For a thermalized sample we have to sum over all possible sets of (j, k, l) weighted by the initial population distribution. This is accomplished by introducing the proper Boltzmann or Bose-Einstein statistical factor in $|A_{jkl}|^2$. In the semiclassical model this is accomplished by an analytic integral that predicts an exponential lineshape
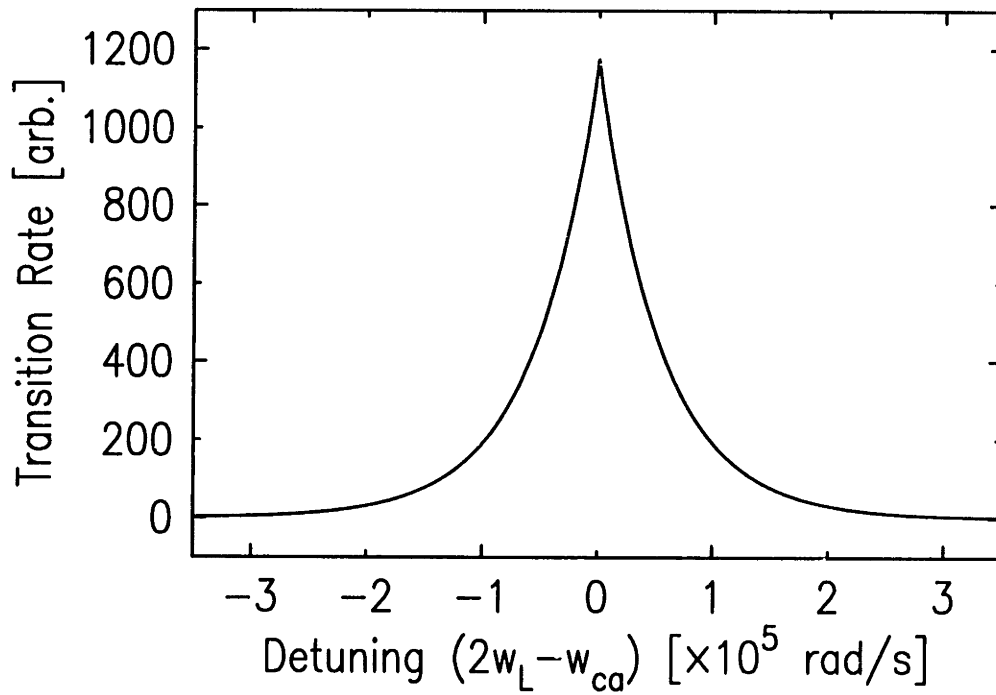
Figure 2-3: Thermalized spectrum with $T = 300\mu K$, $\Omega = 1560 rad/s$ and $w_0 = 40\mu m$ which gives $\alpha w_0 \approx 6.29$. Frequency resolution is not enough to resolve the peaks separated by 2Ω.
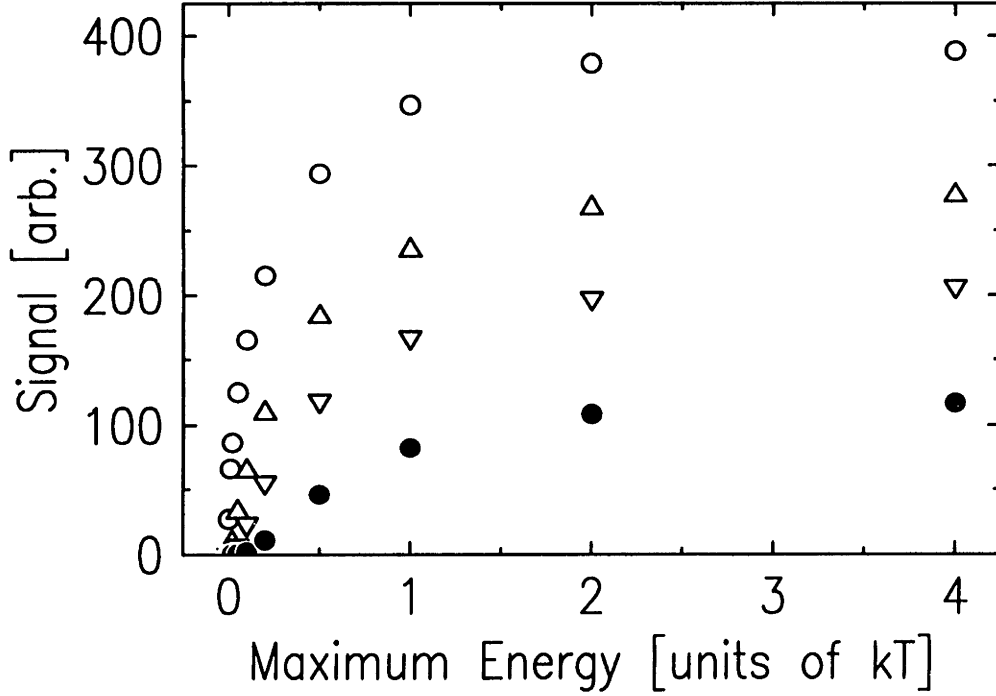
Figure 2-4: Variation of the transition rate for different truncation energies at specific frequency detunings $d\omega$ for $T = 300\mu K$, $\Omega = 1560 rad/s$ and $w_0 = 40\mu m$. $\circ$: $d\nu = 0$, $\triangle$: $d\nu = 4.96 kHz$, $\bigtriangledown$: $d\omega = 9.93 kHz$, $\bullet$: $d\omega = 19.8 kHz$.

$W(\delta\omega) \propto exp{-}|\delta\omega|/\Delta\omega_0$, where $\Delta\omega_0$ is a function of w_0 and temperature. Our calculated spectrum in Fig.2-3 shows the envelope of fine spaced lines for $\alpha w_0 \approx 6.29$ at a temperature of $300\mu K$. The thermal distribution was truncated at an energy of $8kT$. The spectrum fits well the exponential lineshape obtained from the semi-classical theory. For instance, the linewidth (FWHM) of the spectral envelope shown is $\gamma \approx 76 krad/s$ which is in good agreement with the predicted $\gamma_{tof} = (2\log 2)v_{ro}/w_0 \approx 77 krad/s$ with $v_{ro} = \sqrt{2kT/m}$.

The reason for such a sharply peaked spectrum comes from the fact that the very slow atoms contribute enormously at the resonance as can be easily seen from Fig.2-4. Here, the laser sits at a particular detuning and we vary the threshold energy, i.e.,
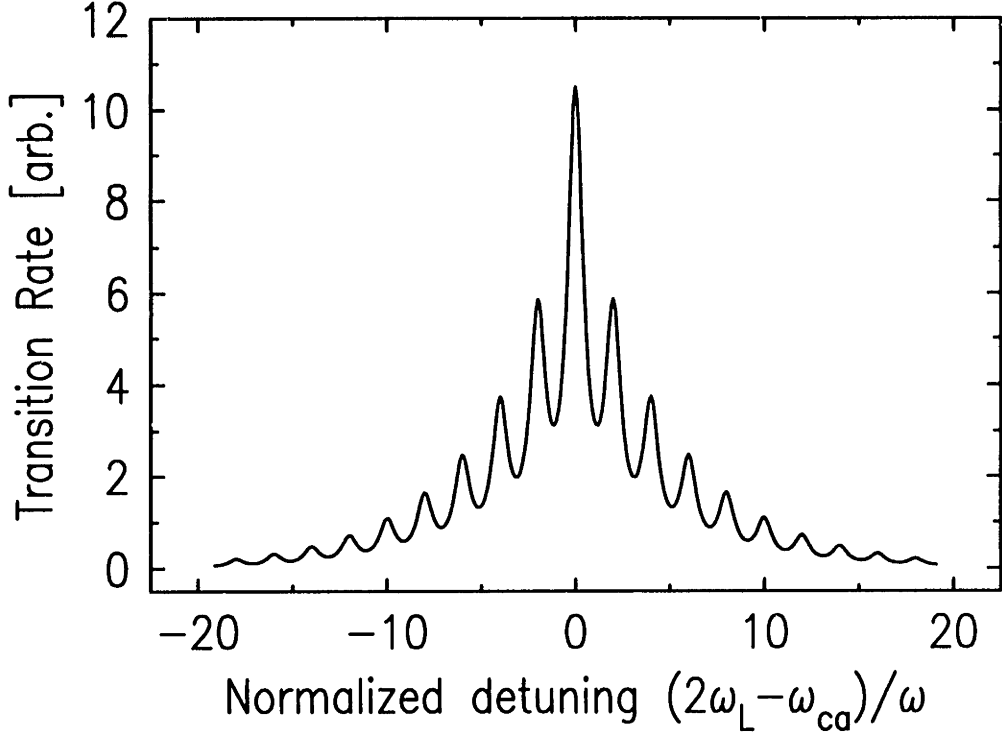
Figure 2-5: Thermalized spectrum with $T = 100\mu K$, $\Omega = \Gamma_c = 2\pi \times 1kHz$ and $w_0 = 40\mu m$ ($\alpha w_0 \approx 12.6$). Frequency resolution is good enough to resolve the peaks.

the energy at which the thermal distribution is truncated. In this case we find that the atoms with energy lower than $0.05 \times kT$ contribute close to 30% of the resonance peak.

The actual computation of these results was achieved through a two step process. First the 1-dimension spectrum was generated. The 2-dimensional spectrum was computed by taking the convolution of the 1-d spectrum with itself, i.e.,

$$W_{2d}(d\omega) = \sum_{d\omega_x} W_{1d}(d\omega_x)W_{1d}(d\omega - d\omega_x) \tag{2.24}$$

When the trap oscillation frequency is large compared to the system's resolution,

the spectrum clearly presents sidebands as in Fig.2-5. In this spectrum, the infinitely sharp transitions were convoluted with a lorentzian lineshape with FWHM Γ_c. The ratio Ω/Γ_c sets the contrast of the fringes while the envelope still resembles the exponential lineshape. It is clear at this stage that the resolution becomes determined by Γ_c, instead of the envelope's width.

If one consider this process as a line-narrowing technique it is important to notice that this is not a velocity selective process. Therefore, there are potentially large gains to the transition rate once the system enters such a regime. The transition rate at the line center increases dramatically with decreasing γ_c since the total area under the spectrum is preserved. As the beam waist is made larger, or the trap gets compressed into the beam, or as the temperature drops, the number of relevant sidebands decreases. If the trap were not harmonic, i.e., with nonuniform levels' energy separation, the peaked structure could completely wash out. Another effect that could easily change this result is a residual misalignment between the beams, since it would add some extra momentum component in the radial direction besides the one provided by the variation of the intensity.

If we generate a Bose-Einstein condensate, we can look for its signature both in the Doppler-free spectrum and in the recoil shifted Doppler-sensitive spectrum. In Chapter 4 we compute these spectra using the basic machinery developed here.

2.6.1 Accounting for inhomogeneity

In this section we modify the formalism presented above to consider the effect of inhomogeneity in the resonance frequency due to the trapping potential. In particular, we look at the case of magnetically trapped spin polarized hydrogen. The excited optical transition is $1S, F = 1, m_F = 1 \rightarrow 2S, F = 1, m_F = 1$, where F is the total spin quantum number. The energy of both levels scale linearly with magnetic field but due to a small relativistic correction to the electron g_e-factor between the $1S$ and the $2S$ states the resonance frequency changes slightly with magnetic field. The g_e-factor scales with the electronic quantum number n as [23]:

$$g_e(n) = g_e(1 - \frac{\alpha_{FS}^2}{3n^2})$$

(2.25)

where g_e is the free electron factor and $\alpha_{FS} \approx 1/137$ is the fine structure constant. To calculate the Zeeman shift of the 1S-2S transition, we start with the hyperfine Hamiltonian

$$H = ah\vec{I} \cdot \vec{S} + g_e \mu_B \vec{S} \cdot \vec{B} - g_p \mu_N \vec{I} \cdot \vec{B}$$

(2.26)

For low fields, $F = S + I$ and m are good quantum numbers. For $F = m = 1$

$$W_{11} = \frac{1}{4}ah + \frac{1}{2}(g_e\mu_B - g_p\mu_N)B \qquad (2.27)$$

The field dependent energy shift, $\delta W \equiv W_{11}(2S) - W_{11}(1S)$ is

$$\delta W = \frac{1}{2}\mu_B B[g_e(2S) - g_e(1S)] \qquad (2.28)$$

Using Eq.2.25 we obtain

$$\delta W = \frac{g_e}{2}\frac{\alpha_{FS}^2}{4}\mu_B B \qquad (2.29)$$

with a corresponding frequency shift for an atom sitting at field B of

$$\delta\nu = \frac{\delta W}{h} \approx 18.6(Hz/gauss)B. \qquad (2.30)$$

For a field of $0.3gauss$ (with a corresponding energy in temperature $T = 67.2(\mu K/G)\times$ $0.3G \approx 20\mu K$) the shift is $\delta\nu \approx 5.6Hz$. Although this is a small shift it is five times larger than the natural decay linewidth. Therefore it is imperative to understand the lineshape for a thermal distribution if one wants to achieve accuracy beyond this value. That is the task we now undertake.

The formalism of trap states that we introduced in this chapter provides an excellent way of computing this lineshape. There are two required modifications as I discuss below.

A typical magnetic trap in our experiment provides a harmonic potential in all directions with radial frequency about ten times larger than the axial frequency. The necessary bias field puts the minimum of the parabolas at a constant field B_{bias}. This field can be tuned with a knob and it can be measured by Hall probes or by measuring the trap oscillation frequency in the spectra.

The first modification to our spectrum then, is that it is shifted by an amount given the bias field through Eq.2.30. Since this is a constant shift, tunable and measurable, we will neglect it in the discussion and calculated spectrum that follows.

The second modification is to allow for the trap oscillation frequencies of the electronic excited state to be different from the corresponding frequencies in the ground state. Now, an atom moves from an eigenstate of the trap with frequency Ω to an eigenstate of the trap with frequency $\Omega + d\Omega$ where $d\Omega \approx 0.5(\Delta g_e/g_e)\Omega = 0.5(\alpha_{FS}^2 \Omega/4) \approx 6.6 \times 10^{-6}\Omega$. We then rewrite the difference in trap states frequencies as:

$$\Omega_{fj} \rightarrow (\Omega + d\Omega)(f + 1/2) - \Omega(j + 1/2), \qquad (2.31)$$

with an equivalent expression for Ω_{gk}. I_j^f in Eqs. 2.9, 2.12, 2.49 becomes:

$$I_j^f \equiv < f|e^{-2x^2/w^2(z)}|j >=$$

$$\frac{(\alpha'\alpha w^2(z))^{1/2}e^{-\frac{w^2(z)}{8}(\alpha\sqrt{2j+1}-\alpha'\sqrt{2f+1})^2}}{[4\pi^2(2j+1)(2f+1)]^{1/4}}\delta_{(j+f=even)} \qquad (2.32)$$

where $\alpha' = \sqrt{m(\Omega + d\Omega)/\hbar}$. Similar substitutions should be made for the z-motion, as we soon discuss.

We need to calculate the z matrix element in Eq. 2.13:

$$I_{z:l\to h} \equiv < h_c|e^{-(1+z^2/z_0^2)\psi}|l_a > \qquad (2.33)$$

where indexes a and c correspond to the electronic states. For a typical trap with $\Omega_z \approx 500 rad/s$, the extent of a wavefunction with energy of $20\mu K$ ($n \approx 4000$) is about $1mm$. This is very small compared to the laser beam parameter $z_0 \approx 20mm$ and in this case we can neglect the z^2/z_0^2 term in the matrix element above. The next simplification comes from the fact that the frequency spacing of the considered trap ($\approx 500 rad/s$) is larger than the expected magnetic frequency shift of a $20\mu K$ atom. We then expand $< h_c|$ in terms of $< h_a|, < h_a - 2|,$ and $< h_a + 2|$ to obtain:

$$< h_c | \approx < h_a | + \frac{d\Omega}{\Omega} \sum_{n \neq h} \frac{< h_a | (\alpha_z z)^2 | n_a >< n_a |}{n - h}$$

$$\approx < h_a | - \frac{d\Omega}{\Omega} \frac{\sqrt{h(h-1)}}{4} < h_a - 2 | + \frac{d\Omega}{\Omega} \frac{\sqrt{(h+2)(h+1)}}{4} < h_a + 2 | \qquad (2.34)$$

where the last expression was easily derived by using the raising and lowering operators $(\alpha_z z = (a^+ + a)/\sqrt{2})$. The normalization parameter for the wavefunction above is about $1/1.001$ for $h \approx 4000$, so we neglect normalization. We then obtain for Eq.2.33:

$$I_{z:l \to h} \approx e^{-\psi} \left[\delta_{l,h} - \frac{d\Omega}{\Omega} \frac{\sqrt{h(h-1)}}{4} \delta_{l,h-2} + \frac{d\Omega}{\Omega} \frac{\sqrt{(h+1)(h+2)}}{4} \delta_{l,h+2} \right] \qquad (2.35)$$

While the bias field shifts the spectrum, the change in radial trap frequency mostly distorts the spectrum and the individual peaks as seen in Fig. 2-6. Also shown in Fig. 2-6 is the effect of the trapping potential in the z-direction. The shift due to bias field is not included in the spectra of Fig. 2-6 to make the comparisons easier.

This spectrum displays some unexpected features. Notice how the spectrum shifted much more when the z direction is included compared to the little shift the radial direction contributes. The extra shift due to z direction is what we expected from Eq. 2.30, while the radial direction is contributing with much less than expected.

52
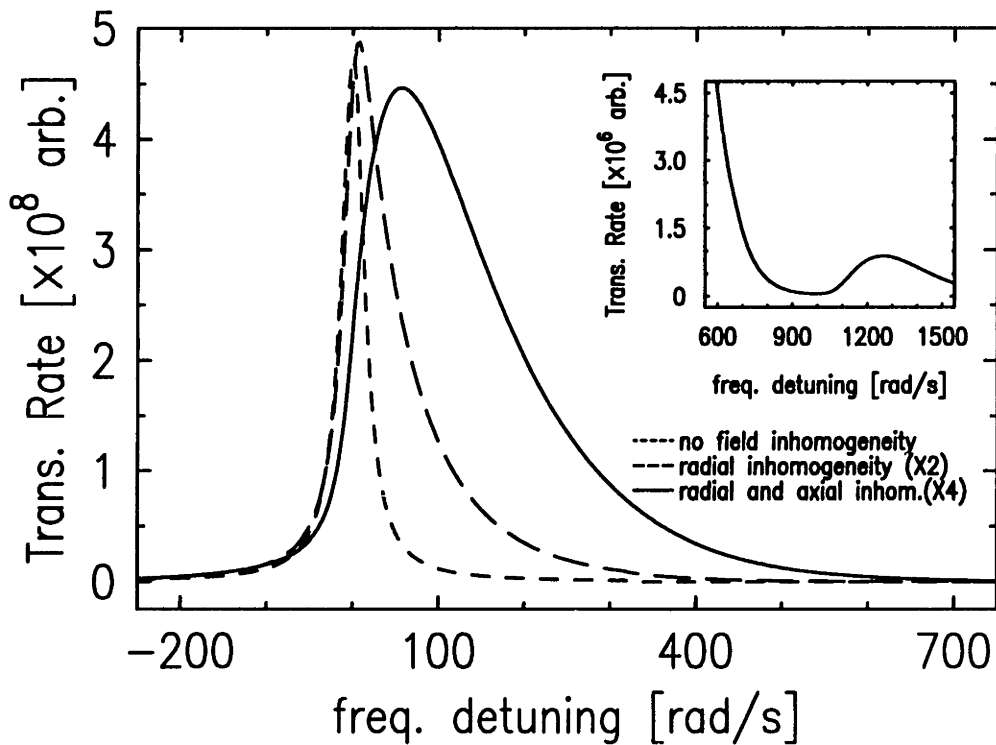
Figure 2-6: Central peak of spectra for magnetically trapped hydrogen at $T = 100\mu K$. $\Omega_x = \Omega_y = 2\pi \times 1kHz$, $\Omega_z = 2\pi \times 82.7Hz$ and $w_0 = 40\mu m$ with $\Gamma_c = 2\pi \times 5Hz$. The spectrum in short dashed line ignores field inhomogeneity while the one in long dashed line shows the radial contribution of the field inhomogeneity and the solid line one accounts for the axial variation of the field. The solid line spectrum is not frequency shifted by a bias field in order to make the lineshapes comparison easier. Notice the appearance of sidebands due to the axial trap frequency as seen in the insert. See text for discussion.

That is surprising because atoms with a given energy feel the same average field independently of the direction they travel, and therefore one expects the same shift in the spectrum. This is indeed the case for monoenergetic atoms but not for the thermal distribution that generates the spectrum. The small radial size of the laser beam greatly enhances the absorption by the slow atoms that contribute to the center of the spectrum while the fast, energetic, atoms are enhanced in the wings of the spectrum. Therefore, one is actively selecting velocity classes depending on the laser frequency, and in the line center, the "effective temperature" is much smaller than the sample temperature. This resembles the velocity selection method of Chebotaev and coworkers[24] to supress the second order Doppler shift in saturation spectroscopy. As in Chebotaev's method, we buy less assymetries and systematics at the expense of signal to noise ratio.

This imediately suggests a way of extending this velocity selection to the axial direction. Focus the laser beam, or open the trap in the axial direction so that in the extent of a beam divergence length the energy of the trap is still very small. In order to satisfy a similar requirement in the radial direction one could construct a trap whose strength of the radial direction follows the same hyperbola as the beam waist. In this case, in order to calculate the spectrum, one would have to include the z^2/z_0^2 term in equation 2.34. At any rate, the knowledge of these lineshapes should allow one to determine the 1S-2S center frequency with very little uncertainty.

2.7 Conclusion

Using the quantized states of a harmonic trap, we have developed expressions that predict the spectral lineshape for trapped atoms interacting with a gaussian laser beam via Doppler-free 2-photon absorption in the regime of low intensities. When the existing broadening, excluding transit-time broadening, is not bigger than the trap level energy separations, one expects to resolve peaks that are separated by twice the trap oscillation frequency. These are superimposed on a typical transit-time broadened line shape. In this case one can expect a very high-resolution that is not limited by time-of-flight broadening. As a consequence, one also obtains a much higher transition rate for absorption in this regime. This narrowing of the line is not a group selective method as in the case of velocity selective methods like saturated absorption. When the quantum features are not resolvable, we recover the semiclassical result[20].

The phenomenon of transit-time broadening is reinterpreted as transverse momenta redistribution from the laser to the atom. In this quantized picture, the atom can only accept momenta that would take it from one eigenstate into another eigenstate. Within this formalism we can easily account for the change in resonance frequency with trapping field for the case of magnetically trapped spin-polarized hydrogen and compute the expected spectrum. We compute lineshapes and show how one can actually work with energy classes that are well below the sample temperature and obtain a much smaller shift and broadening than what has been predicted[25].

The formalism presented here can be easily extended to different trap shapes as

well as different laser beam profiles.

2.8 Complement I: Solution of Eq. 2.9

In this section we present an exact and an approximate solution to Eq. 2.9 that we transcribe below:

$$I_j^f \equiv\; < f|e^{-2x^2/w^2(z)}|j >$$ (2.36)

The wavefunctions for the harmonic oscillator $|f>, |j>$ can be written in terms of Hermite polinomials $H_n()$ as:

$$\Psi_j(\alpha x) = N_j \times e^{-\alpha^2 x^2/2} H_j(\alpha x)$$ (2.37)

where $N_j \equiv 1/(2^j j! \pi^{1/2})^{1/2}$ is the normalization factor. By defining $\xi \equiv \alpha x$ and $\gamma^2 \equiv 2/(\alpha w(z))^2$ we can rewrite Eq. 2.36 as:

$$I_j^f = N_j N_f \int d\xi e^{-(1+\gamma^2)\xi^2} H_j(\xi) H_f(\xi)$$ (2.38)

We can now make use of the generating function for the Hermite polynomials[26]:

$$g(\xi, t) = e^{-t^2 + 2t\xi} = \sum_{n=0}^{\infty} H_n(\xi) \frac{t^n}{n!} \tag{2.39}$$

Consider then, the following relation:

$$\int d\xi\, e^{-(1+\gamma^2)\xi^2} g(\xi, s) g(\xi, t) = \sqrt{\frac{\pi}{1+\gamma^2}} e^{-t^2 \frac{\gamma^2}{1+\gamma^2}} e^{-s^2 \frac{\gamma^2}{1+\gamma^2}} e^{st \frac{2}{1+\gamma^2}} \tag{2.40}$$

But this is also equal to:

$$\sum_{n,m} \frac{t^n s^m}{n! m!} \int d\xi\, e^{-(1+\gamma^2)\xi^2} H_n(\xi) H_m(\xi) \equiv \sum_{n,m} \frac{t^n s^m}{n! m!} C_{n,m} \tag{2.41}$$

If we now expand the exponentials of s and t and equate the terms with the same power in s and t for the equations above we obtain:

$$C_{n,n+2k} = \frac{n!(n+2k)!\sqrt{\pi}}{\sqrt{1+\gamma^2}} \Big[\frac{(-1)\gamma^2}{1+\gamma^2}\Big]^{n+k} \sum_{j=n,n-2,\ldots} \frac{(-2/\gamma^2)^j}{(\frac{n-j}{2})!(\frac{n+2k-j}{2})! j!} \tag{2.42}$$

Inserting the normalizing factors we obtain the desired result:

$$< n|e^{-2x^2/w^2}|n + 2k > = \frac{C_{n,n+2k}}{(2^{2(n+k)} n!(n+2k)!\pi)^{1/2}} \tag{2.43}$$

57

where k and n are positive integers.

2.8.1 Approximate Solution to Eq. 2.9

The exact solution above becomes quite difficult to handle for large n due to the factorials, besides failing to make apparent the physics involved. It is thus usefull to work out an approximated solution as follows.

In a two-photon experiment where one has limited amount of power, one usually focuses the laser beam tightly to obtain an increase in the local intensity. The beam waist then, ends up being much smaller than the typical sample radius. For the majority of the atoms in the sample, the change in potential energy as it goes across a beam waist is much smaller than its total energy. In this case we can regard the potential constant and the wavefunction near the origin, where the laser goes through, becomes a free-particle like wavefunction.

This approximation is particularly good for large quantum numbers where the wavefunction extends far beyond a beam diameter. A typical experimental situation at the Spin-polarized hydrogen group at MIT, provides a $100\mu K$ sample held in a magnetic trap where the ground state wavefunction radius extends over $10\mu m$ and the wavefunction for an atom at the thermal energy, $n \approx 20,000$, extends over $1.6mm$ while the beam waist is $40\mu m$. By using this approximation we will certainly be imprecise about the first few energy levels. But for these low n's we can easily check the results against the exact results. For the situation above we find that the approximated solution, i.e. Eq. 2.12 is off by 10% for $j = 10, f = 10$ and by 1.2% for

$j = 20, f = 22$ from the exact values given by Eq. 2.43.

We approximate the harmonic potential wavefunctions around $r = 0$ by considering the atom to behave as a free particle (zero potential) with the given harmonic oscillator energy and some amplitude to be determined. The functional form for the ket $|l>$ in the x-direction then becomes:

$$|l> \rightarrow \frac{\alpha^{1/2} X_l}{2} (e^{i\alpha\sqrt{2l+1}x} + (-1)^l e^{-i\alpha\sqrt{2l+1}x}) \tag{2.44}$$

where X_l is the peak amplitude of the wavefunction around the origin, soon to be determined.

Substituting this expression in Eq. 2.36 we obtain:

$$I_j^f = \frac{\alpha^{1/2} X_j}{2} \frac{\alpha^{1/2} X_f}{2} \times$$

$$\int dx \left[e^{i\alpha\sqrt{2j+1}x} + (-1)^l e^{-i\alpha\sqrt{2j+1}x} \right] e^{-2x^2/w^2(z)} \left[e^{-i\alpha\sqrt{2f+1}x} + (-1)^l e^{i\alpha\sqrt{2f+1}x} \right] \tag{2.45}$$

The equation above reveals the same physics of momentum transfer as Eq. 2.10 when we used the free-particle wavefunction. Now we are calculating the momentum components of the laser beam profile at wavevectors $(\pm\sqrt{2l+1} \pm \sqrt{2m+1}) \times \alpha$. The result is simply:

$$I_j^f = \frac{X_j X_f \alpha w(z)}{2[2/\pi]^{1/2}} \delta_{(j+f=even)} \times \tag{2.46}$$

$$\left[e^{-\frac{(\alpha w(z))^2}{8}(\sqrt{2j+1}-\sqrt{2f+1})^2} + (-1)^f e^{-\frac{(\alpha w(z))^2}{8}(\sqrt{2j+1}+\sqrt{2f+1})^2} \right]$$

For large quantum numbers, which is usually the case around the thermal energy, we can neglect the terms dependent on the sum of the square roots.

In order to determine the coefficients X_j, X_f we resort to the power series of the Hermite polynomials in which case we can easily write for the even wavefunctions $\Psi_{2n}(x)$ [26]:

$$\Psi_{2n}(0) = (-1)^n \frac{(2n)!}{2^n n!} / ((2n)! \pi^{1/2})^{1/2} \tag{2.47}$$

To extend this result to odd wavefunctions we approximate it by employing Stirling's approximation for the factorials and we obtain:

$$X_j \approx \pm (\frac{2}{j\pi^2})^{1/4} \tag{2.48}$$

Every time n changes by 2 the Hermite polynomials will change phase at the origin by 180 degrees, and this sets the sign of $I_j^f \propto (-1)^{(j+f)/2}$. Since this expression will

eventually be squared we omit the sign. In order to extend the result all the way to $n = 0$ we add $1/2$ to the quantum numbers in the denominators. The final solution then is:

$$I_j^f = \frac{\alpha w(z) e^{-\frac{\alpha^2 w^2(z)}{8}(\sqrt{2j+1}-\sqrt{2f+1})^2}}{[4\pi^2(2j+1)(2f+1)]^{1/4}} \delta_{(j+f=even)} \tag{2.49}$$

The same way that we regarded $\hbar\alpha\sqrt{2j+1}$ as a momentum component of state $|j>$ we can also, inspecting the equation above, regard $\sqrt{8}\hbar/w_0$ as a measure of the momentum content of the laser intensity profile. Using p as simbol for momentum we can rewrite the exponential above as: $\exp[-(p_j - p_f)^2/p_{beam}^2]$. This expression has a clear physical interpretation: a transition $j \to f$ is only induced if the beam intensity profile carries enough momentum to account for the change of momentum in the transition.

2.9 Complement II: Transition rate versus temperature

In this section we apply the results obtained above to estimate the total transition rate at resonance as function of temperature and other parameters and we look for a maximization of the signal in our trap. We first assume a very narrow $\Gamma_c << \Omega$ where one could easily resolve the peaked structure.

By computing few spectra as those shown in Fig.2-3, we can easily extract out the

61

dependence of the resonant signal with temperature and trap oscillation frequency Ω. The z-direction does not enter this discussion as long as the divergency length is comparable to the maximum size of the trap, and we take that to be the case.

We find that the transition rate at resonance, without conserving the total number of atoms (i.e., without renormalizing the Boltzmann distribution) and at constant Ω, varies with temperature as:

$$W(d\nu = 0, T) \propto (T^{1/2})_\Omega \qquad (2.50)$$

The variation with Ω, not conserving the total number and at constant T follows:

$$W(d\nu = 0, w) \propto (\Omega)_T \qquad (2.51)$$

Finally the variation with w_0 at constant power ($w_0^2 |E|^2 =$ constant) approximately follows:

$$W(d\nu = 0, w_0) \sim (\frac{1}{w_0})_P \qquad (2.52)$$

Now let's normalize the distribution for the total number of atoms. We substitute

$$(A_{jk})^2 = Fe^{-\hbar\Omega(j+f+1)/kT} \qquad (2.53)$$

subjected to the normalizing condition $\sum_{jk}(A_{jk})^2 = N$. Summing over the geometric series of Boltzmann factors for the two dimensions (x, y) , we obtain for the normalizing factor F:

$$F = \frac{N(1 - e^{-\beta\hbar\Omega})^2}{e^{-\beta\hbar\Omega}} \approx N(\frac{\hbar\Omega}{kT})^2 \qquad (2.54)$$

Substituting this result together with the previous dependences found we arrive at:

$$W(d\nu = 0, \Omega, T) \propto \frac{NP^2\Omega^3}{w_0 T^{3/2}} \qquad (2.55)$$

But in our trap, to lower the temperature by approximately two orders of magnitude costs us one order of magnitude in evaporated atoms, i.e., $N \propto T^{0.57}$[11]. If we choose a trap configuration where the sample radius is constant and large, the so called "open-trap", then one can also show that $\Omega \propto T$, for a constant bias field.

If Γ_c is such that one can't resolve the peaked structure, then we have to include a reduction factor on the transition rate of $1/\Omega$ and we obtain:

$$W(d\nu = 0, \Omega, T) \propto \frac{NP^2\Omega^2}{w_0 T^{3/2}} \qquad (2.56)$$

Substituting all the T dependences we finally obtain as an approximate T dependence in this case: $W(0, T) \sim T$.

2.9.1 Complement III: Total on-resonance transition rate

For the total on-resonance transition rate we sum Eq. 2.20 for all transitions, which was done for the spectrum in Fig.2-3, and use the result from Bassani et. al.[27] who calculated the sum over all intermediate ($|B>$) states for hydrogen. Their result ($D[J_0] = -11.78$) means, in terms of our result:

$$|\sum_b \frac{\mu_{ab}\mu_{bc}}{i(\omega_{ba} - \omega_L)}|^2 = [\frac{-11.78}{2} \times \frac{2a_0^2 e^2}{3R_\infty/\hbar}]^2 \qquad (2.57)$$

where a_0 is the Bohr's radius, e is the electron charge and R_∞ is the Rydberg constant in energy units. The field can be related to the intensity by $I = c\epsilon_0 |E|^2/2$ which in the case of a gaussian beam with power P yields $w_0^2|E|^2 = 4P/(\pi c\epsilon_0)$. We again ignore the z-dependence by assuming a trap length much shorter than the divergence length . We then obtain for the case where $\Gamma_c > \Omega$, say $\Gamma_c = 2\Omega$:

$$W_{d\nu=0} \approx [\frac{-11.78}{2} \times \frac{2a_0^2 e^2}{3R_\infty/\hbar}]^2 (\frac{4P/w_0^2}{2\pi c\epsilon_0 \hbar^2})^2 \times$$

$$\times N(\frac{\hbar\Omega}{kT})^2 \times (2447 \times \frac{4}{2\Omega})(\frac{\Omega}{1040 rad/s})(\frac{T}{300\mu K})^{1/2}(\frac{w_0}{40\mu m})^3 \qquad (2.58)$$

Substituting the numbers we obtain:

$$W_{d\nu=0} \approx 1.1 \times 10^9 \times$$

$$(\frac{N}{10^{13} at})(\frac{P}{1mW})^2(\frac{\Omega}{1040 rad/s})^2(\frac{300\mu K}{T})^{3/2}(\frac{40\mu m}{w_0}) s^{-1} \qquad (2.59)$$

When $\Gamma_c < \Omega$ and the peaks are resolvable we obtain:

$$W_{\delta w=0} \approx 0.22 \times 10^{13} \times$$

$$(\frac{N}{10^{13} at})(\frac{P}{1mW})^2(\frac{\Omega}{1560 rad/s})^2(\frac{300\mu K}{T})^{3/2}(\frac{40\mu m}{w_0})(\frac{4rad/s}{\Gamma_c}) s^{-1} \qquad (2.60)$$

2.9.2 Connection with the semiclassical result

The semiclassical result for the transition rate in Sandberg's thesis is given in terms of the density. His result (Eq. 3.52 in ref.[28]), in the time-of-flight broadening regime is:

$$R_{TOTAL} = \frac{4n_0 k |D_{ab}|^2 w_0}{\pi v_0} P_{laser}^2 arctan(\frac{l_s}{kw_0^2})$$

(2.61)

First let's make the approximation that the length of the sample is much smaller than the beam divergence length , i.e, $l_s/(kw_0^2) << 1$. Then his result becomes:

$$R_{TOTAL} = \frac{4n_0 l_s |D_{ab}|^2}{\pi v_0 w_0} P_{laser}^2$$

(2.62)

We can easily calculate the central density of our harmonic potential by:

$$N = n_0 \int dz (2\pi r dr) e^{-\beta m \Omega^2 r^2/2}$$

(2.63)

The result is:

$$N = 2\pi n_0 l_s \frac{kT}{m\Omega^2}$$

(2.64)

Substituting in Eq.2.59 we obtain:

$$W = 10^{11} l_s \left(\frac{n_0}{10^{13} at/cm^3}\right)\left(\frac{P}{1mW}\right)^2\left(\frac{40\mu m}{w_0}\right)\left(\frac{300\mu K}{T}\right)^{1/2} s^{-1} \qquad (2.65)$$

which shows the same dependences on power, temperature and beam waist as his result. To compare the number we substitute the values he uses ($T = 100\mu K, w_0 = 38\mu m, n_0 = 10^{13}, P = 10mW, l_s = 40mm$) to obtain:

$$W = 1.2 \times 10^{11} s^{-1} \qquad (2.66)$$

which is in good agreement with his numerical value of $R_{total} = 1.7 \times 10^{11} s^{-1}$ for our choice of Ω and Γ_c.

Chapter 3

Spectroscopy of the Condensate

This chapter discusses spectroscopy of the Bose-Einstein condesate fraction and considers saturation effects on the spectroscopy of hydrogen.

3.1 Two-photon spectroscopy of a trapped Bose-condensate

The goal of this chapter is to address in a very simple manner, using crude approximations, the dynamics of light interacting with a Bose-condensed sample of hydrogen. With the advent of BEC in alkalis, there has been a renewed interest in the dynamics of light interaction with the condensate. B.Sviatunov and G. Shlyapnikov[29] and D.Politzer[30] have considered a non-confined condensate, in a well defined momentum state, and found that polaritons would give rise to total reflection from the condensate. More recently, J. Javanainen[31, 32] and L. You, et. al. [33, 34] considered the case of a confined Bose condensate, in a single photon transition, and found that the resonance would be much broader, consequently weaker, than the resonance from the normal phase. O. Morice, et. al.,[35] have computed the refractive index of a dilute Bose gas across the transition line. The result of all these calculations for a confined condensate is that the spectroscopic signature for the condensate may be hard to find. In view of those results and since we rely on an optical signature for a condensate of hydrogen, we heve performed some simple calculations to check whether it is possible to obtain such a signature in our system.

We are going to neglect all the atoms not in the condensed phase that do not interact with the condensate via absorption or emission of photons. We take the many-body ground state wavefunction to coincide with the trap ground state wavefunction, that is, we assume a density low enough so that interactions between the atoms are negligible compared to the ground state energy. This is the implicit as-

sumption made when using second quantization where the states are described by an occupation number. To simplify the notation we will drop any vectorial form unless it needs special attention.

For two-photon spectroscopy we need to deal with at least 3 levels in the internal atomic structure. We denote the wavefunctions by $|G(k)>, |I_j(k)>$, and $|E_j(k)>$, where G, I, E stand for ground, intermediate and excited electronic states. $G(k)$ is the ground trap state. The subscript $(_j)$ identifies the trap state, and the index k identifies the particle. We anticipate that the intermediate state plays no role in the atomic statistics of the problem since it never builds up population.

A state function $|\Psi(g, e_j)>$ of the atomic system having g atoms in the ground state and e_j atoms in the electronic excited state and trap state j, symmetrized in accordance with the Bose nature of the particles, can be written

$$|\Psi(g, e_j)> = \mathcal{S} \prod_{i=1}^{\alpha} |G(i)> \otimes \prod_{k=1}^{\beta} |E_j(k)> \qquad (3.1)$$

where the operator $\mathcal{S}$ symmetrizes and normalizes the ket onto which it operates and $\beta + \alpha = N_c$, where N_c is the total number of relevant atoms in the sample.

The electric dipole interaction operator is

$$\mathbb{D}(\vec{r}) = \{-\mu_{op}\varepsilon(\vec{r}) + H.c.\} \qquad (3.2)$$

70

where μ_{op} is the electric dipole moment operator and $\varepsilon(\vec{r})$ is the oscillating electric field at position $\vec{r}$.

To calculate the transition rate for exciting one atom out of the condensate into state E_j , we have to evaluate the following expression from second order perturbation theory:

$$W_{g,e_j}^{g-1,e_j+1} \propto |< \Psi_{(g-1,e_j+1)}|I\!\!D|\Psi_{(g-1,i=1,e_j)} >< \Psi_{(g-1,i=1,e_j)}|I\!\!D|\Psi_{(g,e_j)} > |^2 \quad (3.3)$$

The equation above is very similar to Eq. 2.6 with the difference that these wavefunctions contain many terms. Counting these terms is performed as follows: There are $n_t(g,e_j) = N_c!/(g!e_j!)$ terms in a symmetrized wavefunction with occupations g and e_j, with $g + e_j = N_c$. The normalization factor for this wavefunction is $n_t(g,e_j)^{-1/2}$. The intermediate wavefunction has $n_t(g-1,1,e_j) = N!/[(g-1)!1!e_j!]$ terms and the electric dipole operator produces $n_t(g-1,1,e_j)$ identical terms between these two wavefunctions. Therefore, the first matrix element in Eq. 3.3 contributes $g^{1/2}$ terms and the second matrix element contributes $(e_j + 1)^{1/2}$ terms. This dependence on the populations of the levels is exactly the same as if we had used second quantization.

Following the procedures in Chapter 2 for Eq. 2.6, we obtain

$$W_{g,e_j}^{g-1,e_j+1} \propto = g(e_j + 1)|\mu_{gi}\mu_{ie} < E_j(r)|\varepsilon_1(r)\varepsilon_2(r)|G(r) > |^2 \quad (3.4)$$

The main result of Eq.3.4 is the dependence of the transition rate on the final state population. The total transition rate is always proportional to the initial state population regardless of the statistics used. But the enhancement of a scaterring process due to the population of the final state is a feature of the Bose-Einstein statistics.

This has profound implications for the dynamics of the light-matter interaction. One expects, for instance, an increase of the vacuum-induced spontaneous emission rate for atoms that can decay into the condensate since this particular process will be enhanced by the population of the condensate, $(g + 1)$. Coherent processes giving rise to AC Stark shifts, four wave mixing processes, Rayleigh scattering and many other processes may change substantially under the presence of such an enhancement factor. It is important to notice that we are neglecting these coherent effects in this calculation.

A broadening of the line due to an enhanced spontaneous decay rate will have a corresponding influence on the excitation rates and could conceivably prevent us from seeing the condensate optically. To investigate this, we will estimate the two-photon spontaneous emission rate into the condensate.

3.2   Two-photon spontaneous emission

In this section we consider the effect of the quantum degeneracy of the ground state on a single excited atom interacting with the electromagnetic vacuum. Instead of calculating the absolute value for the two-photon decay rate, we are only interested

in the change it suffers from the normal case.

The natural decay rate of the $2S$ state of hydrogen, via emission of two photons, is $\gamma_N = 2.2283 s^{-1}$[36]. Consider an atom initially in state $|E_j>$. How does the transition rate to $|G>$ with occupation number g compare with γ_N where the final center-of-mass state is not especified ?

In order for the atom to decay into the condensate the momentum recoil it gets from the spontaneous emission process must take it from the momentum distribution of the excited state E_j to the momentum distribution of the ground state. It must also have spatial overlap with the condensate wavefunction. All this information is contained in the matrix element of Eq.3.4.

To set the stage for the problem, note that when the 2S state decays by two-photon radiation, the frequency of the photons obeys $\nu_1 + \nu_2 = E_{2S \to 1S}/h$. The spectral distribution funtion is broad — spanning the range 0 to $E_{2S \to 1S}/h$. The distribution funcion is close to parabolic, reaching a maximum at $\nu_1 = \nu_2 = E_{2S \to 1S}/(2h)$. The distribution of momentum recoil of the atom is also broad. Thus, the probability of radiating into the ground state of the trap would normally be neglegible. Because of the Bose enhancement factor, this is not necessarily true. Nevertheless, we will find that the spontaneous decay rate is not greatly enhanced. In this respect, two-photon decay into a Bose condensate differs fundamentally from one photon decay.

The vacuum photons are quantized in plane wave modes. We shall take the spatial dependence of the field of photon 1 to be $\varepsilon_1(\vec{r}) \sim e^{i\vec{k}_1 \cdot \vec{r}}$, with a similar expression for photon 2. The product of the two fields varies in space as $\varepsilon_1(\vec{r})\varepsilon_2(\vec{r}) \sim e^{i(\vec{k}_1 + \vec{k}_2) \cdot \vec{r}}$. Substituting this expression in Eq.3.4, it is clear that if this process is to have a non-

negligible transition rate, the photons' recoil $\hbar \Delta \vec{k} \equiv \hbar(\vec{k_1} + \vec{k_2})$ has to bridge the gap from the excited state momentum to the ground state momentum.

The expression for γ_N can be obtained by integrating the spectral distribution function $A(\nu)$, i.e., $\gamma_N = \int_0^{E_0/h} A(\nu) d\nu$. We use Eq. 27 of J. Tung, et. al.[37], rewritten as

$$\gamma_N \propto \int (4\pi \nu_1^2 d\nu_1) \int (4\pi \nu_2^2 d\nu_2) \nu_1 \nu_2 f(\nu_1, \nu_2) \delta(\nu_1 + \nu_2 - E_0/h) \qquad (3.5)$$

where $E_0 = E_{2S-1S}$, and $f(\nu_1, \nu_2)$ accounts for the summation over all intermediate state matrix elements with the corresponding resonant denominators. From Tung's computed spectral distribution function we aproximate

$$f(\nu_1, \nu_2) \approx (\nu_1 \nu_2)^{-2.5} \qquad (3.6)$$

to provide a reasonable visual fit to his Fig. 1. We are now in a position to estimate the condensate enhanced spontaneous emission rate γ_c. Substituting $\nu = p(c/h)$, rewriting the integration element in Eq. 3.5 in Cartesian coordinates and using Eq. 3.4 we obtain for the ratio

$$\frac{\gamma_c}{\gamma_N} \approx \frac{g \int d^3 p_1 \int d^3 p_2 | < E_j(\vec{r}) | exp[i\Delta \vec{k} \cdot \vec{r}] | G(\vec{r}) > |^2 f(p_1 p_2) p_1 p_2 \delta(p_1 + p_2 - E_0/c)}{\int d^3 p_1 \int d^3 p_2 f(p_1 p_2) p_1 p_2 \delta(p_1 + p_2 - E_0/c)} \qquad (3.7)$$

where we have neglected the recoil energy in the δ-function.

We can estimate the matrix element in the equation above for a harmonic trap by using the Hermite polynomials and their generating function in a similar fashion to Complement I of Chapter 2. Substituting $< E_j|$ by $< n_x, n_y, n_z|$ and $|G >$ by $|0, 0, 0 >$ for a cylindrically symmetric harmonic potential with frequencies $\Omega_x = \Omega_y = \Omega$ and Ω_z, and inverse-length parameters α and α_z ($\alpha = \sqrt{m\Omega/\hbar}$, see Chapter 2), the following is obtained

$$| < E_j(\vec{r})|exp[i\Delta\vec{k} \cdot \vec{r}]|G(\vec{r}) > |^2 =$$

$$\frac{(\Delta k_x/\alpha)^{2n_x}(\Delta k_y/\alpha)^{2n_y}(\Delta k_z/\alpha_z)^{2n_z}exp[-(\frac{\Delta k_x^2+\Delta k_y^2}{2\alpha^2} + \frac{\Delta k_z^2}{2\alpha_z^2})]}{2^{n_x+n_y+n_z}n_x!n_y!n_z!}. \tag{3.8}$$

The maximum of this expression happens for $(\Delta k_j/\alpha_j)^2 = 2n_j$ for $j = x, y, z$. One can easily check that this condition for maximum corresponds to recoil energy conservation.

To evaluate Eq. 3.7 we change the integration variables in the numerator to $\Delta p_j \equiv p_{1_j} + p_{2_j}$ and $\delta p_j \equiv p_{1_j} - p_{2_j}$. For small quantum numbers [1] n_j, the δ-function can be transformed so that $p_1 + p_2 = E_0/c \rightarrow p_1^2 + p_2^2 \equiv \Delta p^2 + \delta p^2 = E_0^2/(2c^2)$. We then rewrite Eq.3.7 as

---

[1]This will be the typical case for atoms excited via two counterpropagating photons (DF). For the Doppler-sensitive case, n_x, n_y will be small while $2n_z$ may be comparable to $(E_0/(\hbar\alpha_z c))^2$.

$$\frac{\gamma_c}{\gamma_N} \approx \frac{\frac{4\pi g}{8[E_0/(2c)]^3} \int d^3(\Delta p)[E_0^2/(2c^2) - \Delta^2 p]| < E_j(\vec{r})|exp[i\Delta\vec{k}\cdot\vec{r}]|G(\vec{r}) > |^2}{(4\pi)^2 \int dp_1 p_1^{0.5}(E_0/c - p_1)^{0.5}} \qquad (3.9)$$

Neglecting $\Delta^2 p$ due to the approximations already employed above and integrating

the numerator by the saddle-point integration method[26] we obtain for γ_c/γ_N:

$$\frac{\gamma_c}{\gamma_N} \approx \frac{(\hbar\alpha)^2\hbar\alpha_z}{[E_0/c]^3}\frac{g}{\sqrt{(2\pi)^3 n_x n_y n_z}} \qquad (3.10)$$

where we used Stirling's approximation to get rid of the factorials. One can also

rewrite Eq. 3.10 in terms of the peak density in the condensate, that can be shown

to be $\rho_c = g\alpha^2\alpha_z/\pi^{3/2}$, and the maximum photon wavelength $\lambda = 121nm$

$$\frac{\gamma_c}{\gamma_N} \approx \rho_c\lambda^3\frac{1}{(2\pi)^3\sqrt{8n_x n_y n_z}}. \qquad (3.11)$$

One should easily recognize $\rho_c\lambda^3$ as the number of condensate atoms per cubic

wavelength. Also notice the resemblance with superfluorescence, with the difference

that these are ground state atoms! The dependence of Eq. 3.11 on (n_x, n_y, n_z) is

discussed later but it clearly implies that γ_c/γ_N is largest for $n_x = n_y = n_z = 0$. In

this case, Stirling's approximation is not valid and we can easily calculate an exact

expression obtaining $\gamma_c(0, 0, 0)/\gamma_N \approx \rho_c\lambda^3\sqrt{2}/(2\pi)^2$. To investigate the magnitude of

γ_c/γ_N, we consider an upper limit for hydrogen we take $\rho_c = 10^{15}at/cm^3$ and obtain

$$\gamma_c(0,0,0) \approx 8\%\gamma_N \qquad\qquad (3.12)$$

The fact the γ_c is neglegible should allow us to perform high resolution spectroscopy in this system. This is very different from the single optical photon case where the predictions are for a very broad linewidth[31].

The dependence of Eq.3.11 on the trap quantum numbers deserves discussion since it deals with fundamental issues about the interpretation of stationary wavefunctions compared to a time-evolvi♭g position and momentum picture. The $(n_x n_y n_z)^{-1/2}$ dependence comes from the amplitude of the wavefunction $|n_x, n_y, n_z>$ at the center of the trap, where it overlaps the ground state function (see Complement I in Chapter 2). In a time domain picture, where the particle is localized, this factor would be absent when the particle overlaps with the ground state. Obviously, in an average over time the $(n_x n_y n_z)^{-1/2}$ factor would be reapear. So, it is a matter of taste, which picture one wants to use. In general, for interaction times shorter than the classical motion period, it is more appropriate to use the time domain picture while for long interaction times, the stationary wavefunctions simplify the calculations.

3.3 The ultimate laser cooling machine: Condensate Laser Cooling

We now proceed to describe an application that assumes a γ_c larger or comparable to γ_N in a hypothetical physical system.

The ideas of making an "atom-laser", i.e., a laser-like atomic beam, in which the atoms mantain coherence with each other and whose luminosity could be enormous by atomic beams standards, has led many people to wander in phase space in search of the way to generate it[38, 39]. We describe the principle of a cooling scheme that can efficiently transfer cold atoms into the condensate via laser excitation followed by spontaneous emission. We believe that this scheme could permit the creation of a real atom-laser. The scheme will probably not work for hydrogen given the numbers above and the difficulty of improving them due to the large dipolar decay rate of the condensate [40]. However it might work in other system. After presenting the idea I will elaborate on some of the requirements for a candidate physical system.

In laser cooling one is always subject to the statistical randomness of spontaneous emission that generates random recoil energy. In the method here proposed, spontaneous emicsion preferentially brings the atoms into the condensate, which is the lowest energy state accessible.

Let's assume a sample, with a condensate fraction, that satifies the following requirements: (1) the decay rate into the condensate, γ_c is larger or comparable to the natural decay rate γ_N; (2) the atoms transverse the trap in times shorter or comparable to the natural lifetime $(1/\gamma_N)$; and (3) the condensate population decay

rate is smaller than the laser excitation rate times $[\gamma_c/(\gamma_c+\gamma_N)]$. The method consists of exciting "normal" atoms in a place that does not overlap with the condensate. In such a place the radiative decay rate due to the vacuum is the natural spontaneous emission rate. If the natural decay rate of the atom is low, it will wander in the excited state around the trap until it enters the condensate region. At this point the atom will experience an enhanced decay rate into the condensate. The probability that the excited atom will radiate into the condensate is

$$P^{0,0,0}_{n_x,n_y,n_z} = \frac{\gamma_c}{\gamma_c + \gamma_N} \tag{3.13}$$

If the above probability is significantly higher than 1/2 the laser excitation will quickly populate the condensate, provided that the condensate is not deplenished too quickly. Of course one has to account for the small heating of atoms that do not decay into the condensate.

If one can find a system that satifies the requirements above, one can envision a steady-state atom-laser with an output flux

$$R_{ao} = R_l \times \frac{\gamma_c}{\gamma_c + \gamma_N} - R_{loss}(\gamma_c) \tag{3.14}$$

where R_{ao} is the atom output rate, R_l is the laser excitation rate of atoms not in the condensate, R_{loss} is the condensate loss rate (dipolar decay rate, for instance),

and γ_c is the decay rate into the condensate for an equilibrium condensate population.

The requirements to make this idea work are quite stringent. First of all, the presence of a condensate is necessary. Second, the excited state should be a metastable atomic state so that the atoms can still be in the excited state when they overlap the condensate. And third, while a two-photon transition would allow for cooling a broad distribution of initial energy states it may prove impossible to yield a large enough γ_c/γ_N.

3.4 Doppler-free excitation of condensate atoms

One might expect that the Bose condensate has a dramatically different response to laser excitation from the normal phase. A complete description of its behaviour requires a comprehensive density matrix treatment. That is beyond the scope of this section. Instead, we shall address the simple but crucial question of whether the Bose degeneracy can be expected to dramatically affect the population transfer. We shall do this by considering the rate equations for population transfer due to the laser excitation alone. These equations are valid only for short times, such that the ground state population is not affected and the excited states populations are small. In this case, light shifts and coherent scaterring effects should play a minor role. Despite these assumptions, this rate equation treatment should be adequate to reveal whether or not the population transfer is significantly affected by the Bose nature of the system.

We consider transitions to and from the ground state induced by laser excitation.

We neglect spontaneous emission (condensate enhanced or natural), ignore collisional population transfer and neglect photoionization (which we discuss in Complement I of this Chapter). The population transfer rate equations are

$$\dot{e}_j = (e_j + 1)gR_{0j} - (g + 1)e_jR_{0j} = (g - e_j)R_{0j}$$

$$\dot{g} = \sum_j [(g + 1)e_jR_{0j} - (e_j + 1)gR_{0j}] = \sum_j -(g - e_j)R_{0j}. \qquad (3.15)$$

where R_{0j} is the "normal phase" laser excitation rate between trap levels 0 and j. For small population transfer, the excited state population follows $e_j(t) = g[1 - \exp(-R_{0j}t)]$. For short times the excited state will get populated by the rate

$$\dot{e}_j = gR_{0j}, \qquad (3.16)$$

which is essencially the same rate as for non-condensate atoms! It is also remarkable that the saturation behaviour would be dominated by the rate R_{0j} and not by some enhanced rate.

Because Bose degeneracy does not enhance the population transfer, we can calculate a spectrum due to the condensate using the machinery developed in Chapter 2. In the following computation we neglect any effect from density shift, as predicted by Jamieson and colleagues[15], and we also assume a laser intensity sufficiently low
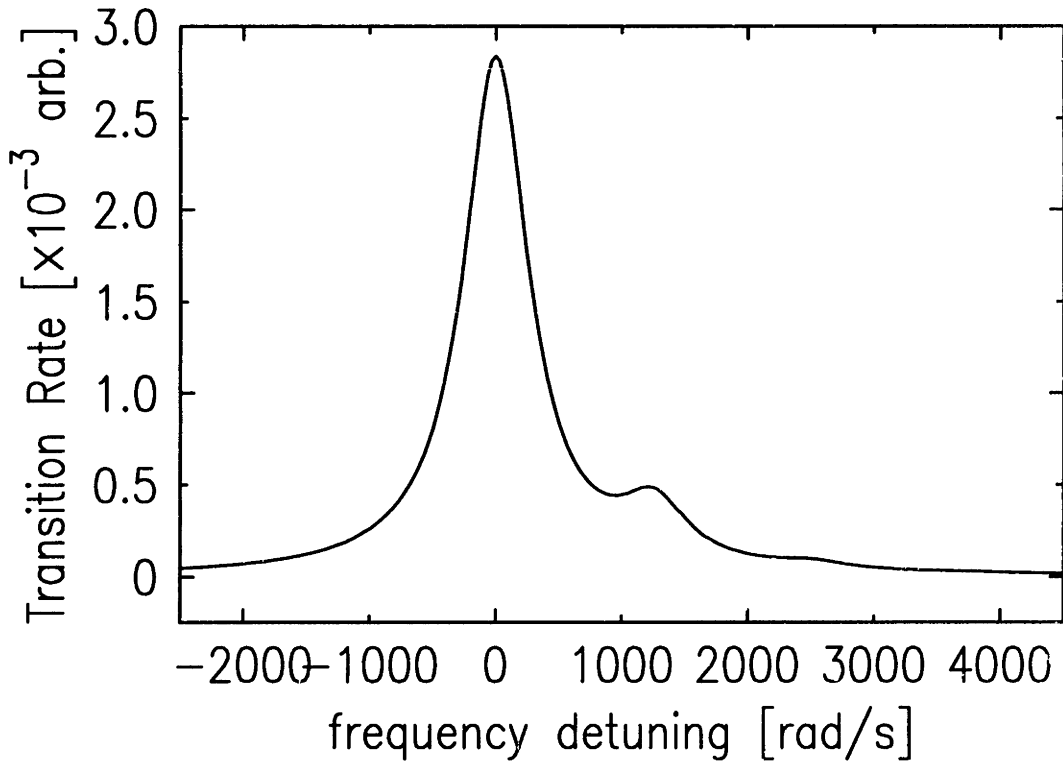
Figure 3-1: Doppler Free spectrum of the condensate alone for a laser waist $w_0 = 20\mu m$ and $\alpha w_0 = 2.0$ corresponding to a radial oscillation frequency $\Omega_x = \Omega_y = \Omega = 2\pi \times 100 Hz$ and a condensate radius $r(1/e) = 10\mu m$. Laser linewidth (@121nm) = Ω.

to avoid saturation.

The spectrum is shown in Fig.3-1 for the conditions stated in the figure caption. The spectrum is clearly asymmetric because the condensate is the minimum trap state and can only be excited to trap states that are higher in energy. The spectrum for a system which is partially condensate is found by adding the spectrum due to the atoms in the normal phase.

3.5   Doppler-sensitive excitation

The Doppler sensitive excitation of the Bose condensate of hydrogen brings no surprises. To analyze it we evaluate the transition matrix elements as in Section 3.2, and calculate the spectrum. Since the trap ground state has a gaussian velocity distribution we expect the spectrum to be a gaussian with a width set by the trap confinement.

The two-photon excitation for the (+) field depends on the field product (see Eq. 3 in Chapter 2)

$$\varepsilon_+\varepsilon_+ = \frac{E_{0+}^2}{1+z^2/z_0^2}exp\{2ikz + 2i\eta(z) - \frac{2r^2}{w^2(z)} + \frac{ikr^2z}{z^2+z_0^2}\} \tag{3.17}$$

For the (-) field we take $z \to -z$ and $E_{0+} \to E_{0-}$. Since the typical extent of $|0_z>$ is much shorter than z_0 We can neglect terms of the order of z/z_0 and obtain

$$\varepsilon_+\varepsilon_+ = E_{0+}^2 exp\{2ikz - \frac{2r^2}{w_0^2}\} \tag{3.18}$$

The matrix element in Eq. 3.4 becomes

$$|<n_z, 2n_y, 2n_x|\varepsilon_+\varepsilon_+|0,0,0>|^2 = \{\frac{(2n_x)!(2n_y)!}{2^{2n_x+2n_y}(n_x!)^2(n_y!)^2}\}\times$$

$$\times [\frac{\alpha^2 w_0^2/2}{(1 + \alpha^2 w_0^2/2)^{n_x+n_y+1}} \cdot E_{0+}^2]^2 | < n_z|e^{2ikz}|0 > |^2 \qquad (3.19)$$

W̰ have calculated the z matrix element above in Eq.3.8. The result is

$$| < n_z|e^{2ikz}|0 > |^2 = \frac{(2k/\alpha_z)^{2n_z} e^{-\frac{4k^2}{2\alpha_z^2}}}{2^{n_z} n_z!} \qquad (3.20)$$

which has a maximum when $(2k/\alpha_z)^2 = 2n_z$. The element above is basically the

momentum component of the ground state at $p = 2\hbar k - \sqrt{2m\hbar w_z n_z}$. By evaluating

the factorials with Stirling's approximation and substituting $n_z = 2k^2/\alpha_z^2 \div n$ we

obtain

$$| < n_z, 2n_y, 2n_x|\varepsilon_+\varepsilon_+|0,0,0 > |^2 = \frac{(\alpha_z/k)e^{-\frac{\alpha_z^2 n^2}{4k^2}}}{\pi^{3/2}\sqrt{n_x n_y}} \left[\frac{\alpha^2 w_0^2/2}{(1 + \alpha^2 w_0^2/2)^{n_x+n_y+1}} E_{0+}^2 \right]^2 \quad (3.21)$$

The excitation from the trap ground state to the trap state $|n_x, n_y, n_z >$ is centered

at the frequency $2\omega_L = \omega_{co} \vdash (n_x + n_y)\Omega + n_z\Omega_z$. Similarly to Chapter 2, we introduce

a normalized lineshape function $g_{a000}^{cn_x n_y n_z}(\omega_L)$ centered at the frequency above. The

spectrum then is proportional to the product of this lineshape to the matrix element

above

$$W_{a000}^{cn_x n_y n_z}(\omega_L) \propto \frac{(\alpha_z/k)e^{-\frac{\alpha_z^2 n^2}{4k^2}}}{\pi^{3/2}\sqrt{n_x n_y}} \left[\frac{\alpha^2 w_0^2/2}{(1 + \alpha^2 w_0^2/2)^{n_x+n_y+1}} E_{0+}^2 \right]^2 g_{a000}^{cn_x n_y n_z}(\omega_L). \quad (3.22)$$

Note that while the peak count depends linearly on the trap parameter α_z, the integrated signal (Σ_n) is constant, independent of the α_z parameter. The spectrum due to the z-motion shows the expected Gaussian envelope profile with a FWHM $\Delta\omega(@121nm) = 4k\sqrt{\hbar w_z \log 2/m}$. This linewidth can also be written as $\Delta\omega = (2/\sqrt{\log 2})(2k)(\hbar\alpha_z/m)$, where the usual $\Delta w = \Delta k v$ is more apparent. Also notice that a simple $\Delta(p_z/\hbar)\Delta z \approx 1$ uncertainty relation predicts the right linewidth up to the $(2/\sqrt{\log 2})$ constant ($\Delta z = 1/\alpha_z$ implies $\Delta v_z \equiv \Delta p_z/m = \hbar\alpha_z/m$).

The center of the Doppler-sensitive spectrum is offset from the Doppler-free line by $\Delta\omega(121nm) = (1/\hbar) \times (2\hbar k)^2/(2m) = 8.422 \times 10^7 rad/s \rightarrow \Delta\nu(486nm) = 3.351 MHz$. This frequency offset is due to two photons recoil energy. While the Doppler spectrum due to the atoms in the normal phase is also centered at this frequency, the width can be as large as MHz. Consequently at this frequency the only significant contribution for fluorescence comes from the condensate fraction. This should provide us with a clear and definite signature of the transition!

In our experiment, the photon's recoil energy will generally be above the trap threshold. In other words our trap is not harmonic for those energies. In this case the final state is part of a continuum and no discrete features should be discernible under the Gaussian profile. Transitions to (n_x, n_y) different from zero are also very improbable with the perfect alignment of the laser beam since the beam waist will in general be much larger than the ground state extent in these directions. In this case, the sidebands shown in Fig. 3-1 will be absent and the spectrum will be purely Gaussian for a monochromatic laser. The sidebands can be made to appear by offsetting the trap such that the condensate lies along the side of the laser beam, say, a

beam waist from the laser axis. Verifying that the sidebands only ocurr to the blue of the peak is a confirmation of the theory constructed in Chapter 2.

3.6   Condensate-enhanced one photon decay

In our typical fluorescence experiment, the hydrogen atom is excited from the 1S to the 2S level. An applied electric field, mixes the 2S and 2P levels causing a fast one-photon decay of the 2S. It is important to know if this decay can be enhanced due to the condensate. If that is the case, the fluorescence photons may be emitted in a very different angular distribution than in the usual fluorescence case. One could also conceive of performing a non-destructive detection of condensate atoms by recycling those excited atoms back into the condensate. Detecting these condensate-enhanced fluorescence photons is difficult because they should be emitted along the laser beam path and one needs a special setup for that.

We then consider the enhancement for the 1-photon decay rate into the condensate. Similarly to two-photon case we are only interested on the ratio of the condensate enhanced decay rate to the natural decay rate. Following the same argument as in Section 3.2:

$$\frac{\Gamma_{2p}^c}{\Gamma_{2p}^N} = \frac{\int p\,dp_x dp_y dp_z | < nz, ny, nx|e^{i\vec{p}\cdot\vec{r}/\hbar}|0,0,0 > |^2 \delta(p + E_r/c - E_0/c)}{4\pi[E_0/c]^3} \qquad (3.23)$$

where $E_r \ll E_0$ is the recoil energy. We are especially interested in the case where

most of the recoil is in the z-direction. Therefore we can eliminate the delta function by setting $p_z \approx p \approx (E_0 - E_r)/c$. Assuming that the initial value of n_z represents an energy close to the 2-photon recoil energy away from the ground state, and using the same techniques as in Section 3.2 we obtain

$$\frac{\Gamma_{2p}^c}{\Gamma_{2p}^N} \approx -\frac{[\hbar \alpha c/E_0]^2 g}{4\pi\sqrt{(2\pi)^2 n_x n_y n_z}} \tag{3.24}$$

where the approximations employed require n_x, n_y different from zero. The discussion about the overlap of the wavefunctions in Section 3.2 is valid and for very short times after the excitation, the excitation particle overlaps with the condensate. In this case the ratio in Eq. 3.24 is of the order of $\Gamma_{2p}^c/\Gamma_{2p}^N \approx (\rho_c \lambda^3)(k/\alpha_z) \gg 1$, for the same parameters as in section 3.2.

Because Γ_{2p}^c can be larger than the $2P - 2S$ separation, it is essential to address the question of how the $2S$ decay is affected by stray electric fields. This is calculated in complement 3.I. For a given electric field, the 2S decay rate can increase or decrease depending on the magnitude of Γ_{2p}^c. The maximum increase in the 2S decay rate due to the condensate is a factor of ten higher than without the condensate. This should not affect an experiment that has little stray electric field.

3.7 Conclusion

I believe that the analysis in this chapter makes a strong case for the possibility of optical detection of the condensate in our trap, notwithstanding the relatively crude level of the calculation. The possibility of observing high-resolution features in the condensate opens the door to a variety of interesting experiments such as squeezing the ground state, studying interactions, propagation of excitations, and may be studying the dynamics of the transition when the fluctuations in the occupation numbers are supposed to be as large as the numbers themselves. And, of course, a condensate should become a master element in the construction of an atom-laser and for related experiments in atom-optics.

3.8 Complement I : 2S decay with E-field

We follow the usual procedure as in Bethe's book[23]. Let's write the unperturbed hamiltonian of the 2S and 2P levels with energy offset by the 2S energy and include the decay as an imaginary energy. The perturbation hamiltonian only has the off-diagonal elements $-\mu E$. Therefore the full hamiltonian, in the basis $[|2S> |2P>]'$, reads:

$$H = \begin{bmatrix} 0 & -\mu E \\ -\mu E & -\hbar\omega_L - i\hbar\gamma/2 \end{bmatrix} \tag{3.25}$$

where ω_L is the Lamb shift. Calculating the eigenvalues of the hamiltonian we

find for the energy of the modified 2S state:

$$E_{2S'} = E_{2S} + \hbar\omega_L \left(\frac{(\mu E)^2}{\hbar(\omega_L^2 + \gamma^2/4)} \right) - i\hbar\gamma/2 \left(\frac{(\mu E)^2}{\hbar^2(\omega_L^2 + \gamma^2/4)} \right) \qquad (3.26)$$

In case γ, the 2P decay rate, is enhanced by the condensate decay we can write $\gamma = \gamma_N + \gamma_c$ and compute the decay rate of the 2S state in the presence of field, given by twice the imaginary part of the equation above divided by $\hbar$, i.e.,

$$\gamma_{2S'} = (\gamma_N + \gamma_c) \left(\frac{(\mu E)^2}{\hbar[\omega_L^2 + (\gamma_N + \gamma_c)^2/4]} \right) . \qquad (3.27)$$

Depending on the value of γ_c the 2S can decay faster or slower than in the normal phase, in the presence of an E-field. The maximum ocurrs for $\gamma_c = 2\omega_L - \gamma_N \approx 2\omega_L$. In this case the maximum 2S decay compared to the normal 2S decay is $\gamma_{2Sc}/\gamma_{2SN} = \omega_L/\gamma_N \approx 10$.

3.9 Complement II : Saturation effects and Photoionization

In this chapter we briefly consider the effects of photoionization and saturation to the transition rates previously calculated. While the transition rate is still roughly the same, with a small decrease due to an increased linewidth, one cannnot assume that the population of the excited level will remain as it would in the absence of these effects. In effect, photoionization dramatically reduces our sensitivity, especially with respect to the condensate where the replenishing of the ground state population may happen slowly.

I will approach this question with a rate equation formalism. I use the rates calculated by others and transcribed in Jon Sandberg's thesis[28]. For this discussion we will constrain ourselves to 3 levels: 1S, 2S and photoionized continuum. We completely ignore non-resonant 3 photon ionization and I will not include the AC Stark shift in this discussion as it has been already considered by Beausoleil[41].

The excitation rate for an atom always in the beam is given by

$$\gamma_e = 85.7 I^2 / \Delta\omega \, (cm^4/W^2 s) \tag{3.28}$$

with a typical value for a 2mW laser ($I_{peak} \approx 40 W/cm^2$) and $\Delta\omega \approx 2\pi \times 4kHz$ of $\gamma_e \approx 5 s^{-1}$.

The cross-section for photoionization of the 2S state by a 243nm photon is $\sigma_{pi} =$

$9.26 \times 10^{-18} cm^2$. This translates into a photoionization rate of

$$\gamma_{pi} = 11.4(I_1 + I_2)cm^2/Ws. \tag{3.29}$$

with a typical value of $\gamma_{pi} \approx 0.9 \times 10^3$. With such a high value it is clear that the photoionization rate is going to dominate the system time constant for saturation. Our rate equations for the considered 3-levels system (with subscripts 1,2, and pi — photoionized continuum) then becomes:

$$\dot{n}_2 = \gamma_e n_1 - [\gamma_e + \Gamma_c + \gamma_{pi}]n_2$$

$$\dot{n}_1 = -\gamma_e n_1 + [\gamma_e + \Gamma_c]n_2 \tag{3.30}$$

$$\dot{n}_{pi} = \gamma_{pi} n_2$$

where we assumed that the photoions and electrons have no decay mechanism and γ_e is the unsaturated 2-photon absorption (and estimulated emission) rate and Γ_c is the decay rate from state 2 to state 1.

In the limits of small population transfer n_1 can be considered a constant and we easily obtain:

$$n_2(t) = \frac{\gamma_e n_1}{\gamma_t}(1 - e^{-\gamma_t t}) \qquad (3.31)$$

where $\gamma_t = \gamma_e + \Gamma_c + \gamma_{pi}$. And n_{pi} follows

$$n_{pi}(t) = \frac{\gamma_{pi}\gamma_e n_1}{\gamma_t}[t - \frac{1 - e^{-\gamma_t t}}{\gamma_t}] \qquad (3.32)$$

Notice that for $\gamma_t t << 1$, Eq.3.31 shows the expected rate $n_2(t)/n_1 \approx \gamma_e t$. In Fig.3-2 $n_2(t)/n_1(0)$ is plotted using Eqs.3.31 and $n_2(t)/n_1(0) \approx \gamma_e t$, for $\gamma_e = 5s^{-1}, \Gamma_N = 8s^{-1}$, and $\gamma_{pi} = 0.9 \times 10^3$.

These curves are important for choosing the laser power and the time it is left to interact with the atoms. When the ground state deplenishes, we want to make the best use of those atoms and and avoid interaction times longer than $1/\gamma_{pi}$. This is particularly important for the condensate as the number of atoms may be quite small and the question about its replenishing rate is not yet answered.

For a normal scan, these rates also affect the lineshape. To fully account for that one has to look at 2 sets of degenerate states in the electronic ground and excited states with different rates between the ground and excited states. Once this problem is solved, one has to perform the thermal average to obtain the spectrum. Of course, saturation affects primarily the cusped peak since most of the atoms that contribute at the central frequency are the slow atoms that remain mostly within the laser beam.

92
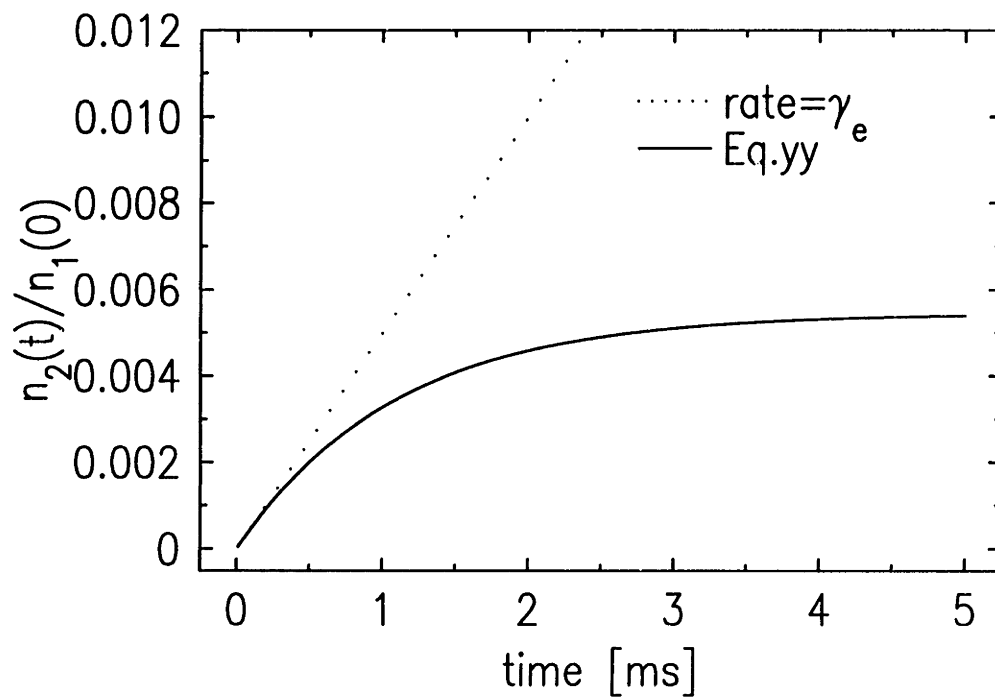
Figure 3-2: Population of the excited state for the $\gamma_e = 5s^{-1}$ and $\gamma_t = 913s^{-1}$. The dashed line does not account for decay out of the excited state while the solid line does..

If one knows the laser beam shape and power and the trap parameters a measure of the photoionization rate would provide the temperature of the sample.

Another issue of interest is the effect of the photoions and photoelectrons to the lineshapes. If these photocharges remain in cyclotron orbits for a long time, they could acumulate and affect the 2S quenching. So far, we have seen no evidence of such a process in the 2S decay curves. If the magnetic field is very strong, one could imagine these photocharges undergoing photoassociation, i.e., there may exist a magnetic field induced stability against photodissociation. This is just a speculation at this point since I have done no calculations in this direction.

Chapter 4

Laser Spectroscopy of Trapped Hydrogen - Experiment

In this chapter I briefly describe the experimental setup, techniques and procedures. I first review trapping, cooling and bolometric detection at a more extended level than the description in Chapter 1. Then I describe the laser system and the operational aspects of the experiment. While the apparatus has undergone many improvements since the description contained in the theses of Doyle[11] and Sandberg[28], the core of the apparatus remains the same as described in those theses. I will concentrate on the changes made to the system system since then but I will also give an overview of the whole system. Experimental results will be discussed only in the next chapter.

4.1 Overview - trapping, cooling and bolometric detection

The object of this experiment is to investigate a sample of cold, trapped spin-polarized hydrogen using two-photon spectroscopy. We want to characterize the thermodinamic state of the sample, study how the trap interacts with the sample and perform spectroscopic measurements of many kinds.

In order to broaden the range of processes one can investigate, high flexibility is required from the apparatus. In our case we want to produce an atomic sample at various temperatures and densities, and be to control its size, position, shape, etc. This kind of control is exerted by the trapping magnets together with trap loading and evaporative cooling procedures, as briefly described below.

As described in Chapter 1 the magnets, in a Ioffe-Pritchard configuration, provide the trapping potential for d-state atoms with a potential minimum at the center of the cell(see Figs.1.1,2). The cell is coated with superfluid ^4He, and molecular hydrogen is frozen in the discharge region. The trap is loaded by pulses of RF that produce atomic hydrogen vapour in all four hyperfine states. During that period the cell wall is heated to 250 mK. The superfluid helium on the cell walls shields the otherwise strongly attractive and dissipative potential between the surface and the atoms, allowing the atoms to bounce off the wall with a high probability. The atoms dissipate their energy with collisions to other H atoms, to He vapour and to the superfluid He until they are caught in the trap.

A diagram of the apparatus is shown in Fig. 4-1. After the first moment of loading

the trap, the discharge temperature falls and the cell heater is turned off. The cell becomes a sink for any atom that hits on it and the helium vapor pressure effectively vanishes. The atoms that have low enough energy stay trapped. The trapped atoms undergo collisions. Two kinds of binary collisions are important for our experiment. The first is a spin-exchange collision with one of the atoms in the "impure" c-state (see Fig. 1-1). The relative phase of the spin up and down components of the c-state is changed with a collision to another atom due to the difference in energy of the singlet and triplet potentials[42]. This results in the loss of such atoms as they eventually change their state to non-trapped state (high field seeking). This kind of collision is responsible for our trap achieving 100% polarization soon after loading, i.e., all c-atoms decay and only d-atoms remain in the trap.

Elastic collisions are very important for the achievement of thermal equilibrium. These are S-wave collisions between d and d-atoms with an energy independent cross-section. As already mentioned in Chapter 1 this collision has a positive scaterring length, meaning that the system is stable against recombination.

In addition, the atoms interact via their magnetic moments so as to relax the spin state, causing them to decay into allowed hyperfine states[42]. This dipolar decay process not only limits the lifetime of our trapped sample but also has serious implications to the sample equilibrium temperature.

Evaporative cooling of hydrogen in our trap has been extensively studied and modelled by John Doyle[11]. Here we briefly describe the process. Our trap shape is such that most of the atoms in a thermalized sample have energies about 1/7 of the trap threshold energy (also, density is highest at the bottom of the trap where
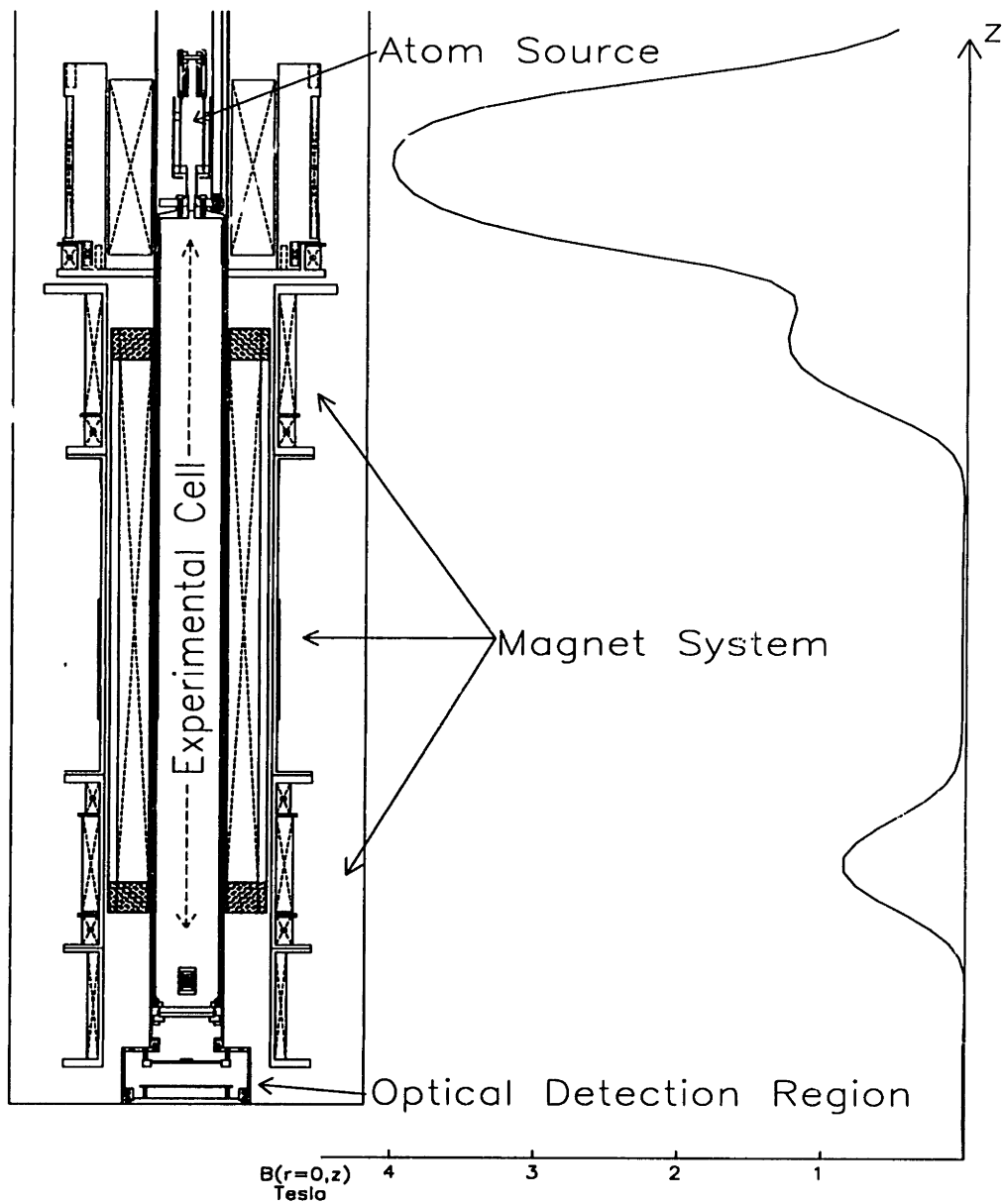
Figure 4-1: Diagram of the laser system.

the energy is lowest). The thermalization of the sample leads to promotion of atoms to energies above the trap threshold. When these "hot" atoms leave the trap region they carry an energy that is much higher than the average energy per atom in the trap. As a consequence the sample is cooled. This is the principle of cooling by evaporation that also works very efficiently in your cup of coffee. Unfortunately our sample also has a heating mechanism. Dipolar decay ocurrs preferentially in high density regions. Therefore, atoms lost by this mechanism carry, in average, less energy than the average atom in the trap thereby heating the sample. The trap shape and the rate at which these processes ocurr determine a final equilibrium temperature for the sample. Once this equilibrium has been "reached" the sample keeps losing atoms by dipolar decay and evaporation without changing its temperature.

In order to cool the sample to a desired point we continuously lower the trap threshold energy forcing more and more "hot" atoms to escape while the sample is thermalizing with the trap. This technique of forced evaporative cooling, proposed by Hess[13], has been successfully used not only by us but by all the labs that have achieved BEC so far. It provides very efficient cooling. We typically lose one order of magnitude in atomic number to drop two orders of magnitude in temperature if the time scales are set properly. After this cooling process the sample is ready for detection or study.

The detection technique we hau ueen using is based on measuring the atomic hydrogen recombination energy with a very sensitive bolometer, a resistor that varies its resistance with temperature. We measure the energy distribution of the sample by carefully allowing the atoms to escape the trap into a zero magnetic field region

where they eventually recombine. The recombination of the hydrogen atoms into a molecule releases a large amount of energy (the molecular potential is 4.6 eV deep supporting 14 vibrational states and many rotational levels), and a fraction of this energy is deposited onto the bolometer. By recording the power deposited onto this bolometer as we lower the trap threshold we obtain the energy distribution of the sample. Since the trapping potential is calculable, these distributions can be fit to a Maxwell-Boltzmann distribution and a temperature assigned to the sample[11]. Accuracies in the temperature are typically better than 10% at temperatures from $120 - 3000 \mu K$. Measurements of colder temperatures encounter escape time problems as well as signal to noise ratio problems. I. Albert Yu[43] has carefully studied dump shapes and has made some progress in accounting for escape time.

By measuring the dipolar decay rate of the sample while the atoms are held in a constant trap we can calculate the sample density. This is accomplished through a series of identical trap loads by holding the trap steady, after evaporation, for different times. The 2-body dipolar decay constant has the value $G_{1d} = 10^{-15}(cm^3/s)$[42]. Since the sample is destroyed after each measurement, it is essential that the trap is reproducible. Reproducibility is often better than 1% in the temperature range of $120 - 3000 \mu K$ and densities in the range $10^{12} - 10^{14} cm^{-3}$.

Although it is very sensitive, simple, and extremely powerful, this bolometric detection would not allow us to detect Bose-Einstein condensation, for the information about the condensation would probably be destroyed by the time the bolometer detects the recombination heat. There are also serious limitations in the response time constant and sensitivity when one approaches very low temperatures and low number

of atoms. These limitations in the bolometric detection technique and the fascinating prospects of high-resolution spectroscopy of hydrogen brings motivated the laser system that we now describe.

4.2 Overview of the Laser System

The ideal laser for high resolution spectroscopy would be powerful, highly monochromatic, propagate in a gaussian mode and be spatially stable. While our laser system is not ideal it should be adequate for initial studies of our sample. Most of the description that follows is thoughrougly explained in the thesis of Jon Sandberg[28].

The diagram in Fig. 4-2 shows the main components of our system for generating 243nm radiation. A Coherent[44] Innova 200 Krypton Ion laser pumps a Coherent 699-21 ring dye laser with approximately 4.6W in multiline violet. The laser is tuned to the blue at 486nm with the circulating dye Coumarin 102[45]. The dye laser has been modified by including an Electro-Optical modulator (EOM) intracavity to allow for fast phase modulation. This laser frequency is locked to a mode of the reference cavity (a Fabry-Perot) that is evacuated by an ion pump to 10^{-7} torr and temperature stabilized to better than $1mK$. We use standard FM sidebands techniques for acquiring the error signal[46]. This system is performing well. The laser remains locked for many hours and can have a linewidth of less than $1kHz$ for $< 1s$ measuring times. The cavity drift rate changes slowly over time. For over a month we have observed a linear drift rate of about $5kHz/hr$.

For absolute frequency calibration we use the i_2 absorption line of molecular tel-
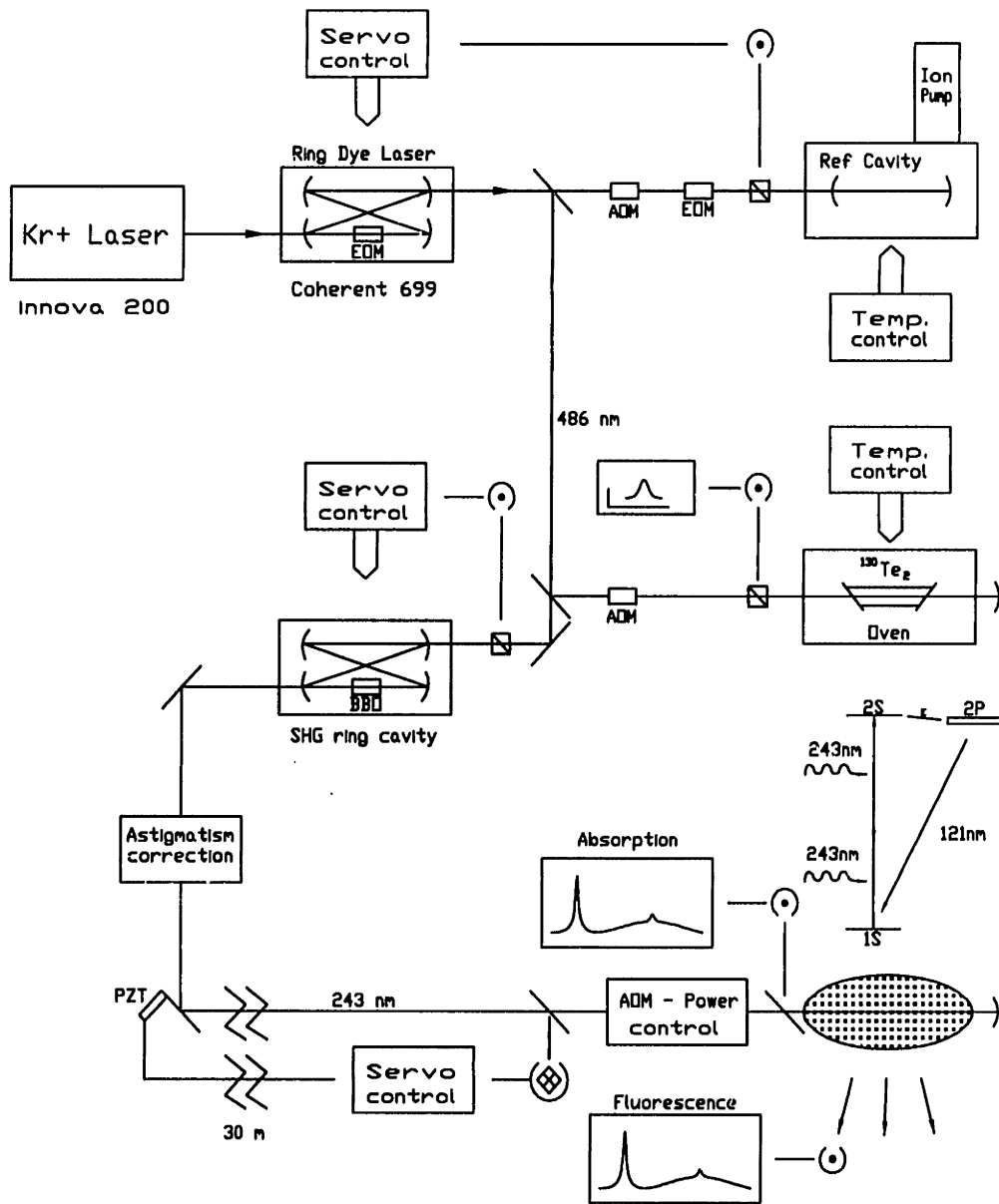
Figure 4-2: Diagram of the laser system.

lurium. This line has been calibrated[47, 48] and is located $57MHz$ above 1/4 of the hydrogen frequency $(E_{2S} - E_{1S})/\hbar$. By shifting the lasers frequencies with Acoustic-Optic modulators (AOM) we are able to observe the hydrogen line while monitoring the peak of this Te_2 line. The Te_2 spectroscopy is discussed in more details in Section 4.6.

In order to generate a reasonable amount of UV power at 243nm we double the blue laser frequency in an enhancement cavity. This cavity is locked to the laser frequency using Hansch's polarization method[49]. The 243nm beam comes out of the cavity in a highly astigmatic mode and a special set of lenses corrects this aberration but still leaving non-gaussian spatial modes that have to be filtered out.

The distance from the optics laboratory, where the laser is located, to the dilution refrigerator, where the atomic sample is produced, is about 26m. The beam travels through a tube and it moves around by more than a beam diameter (few mm) on top of the refrigerator. To make the experiment possible we have developed an active beam steering system that positions the beam to about a one-hundredth of a beam diameter. This system works really well and will be described later.

Close to the trap we spatially filter the 243nm beam, and using an AOM we can chopp the beam on and off. The AOM also allows us to control the laser power sent to the trap. The power controller is essential for measuring the double pass absorption through the system and can be used for performing atomic absorption measurement. The 243nm beam goes into the refrigerator, where the atomic sample is contained, and is retro-reflected back out. A good overlap of the incoming and retro beams is required to produce the standing wave for Doppler-free two-photon excitation. Part of

the retro beam is used to measure the absorption and part to monitor the alignment.

In order to detect the Lyman$_\alpha$ fluorescence we have a Multichannel[50] detector below the retro-mirror. The detection fractional solid angle is about 10^{-4} which, multiplied by window's transmission, Lyman$_\alpha$ filter's transmission and the detector quantum efficiency, results in about 5×10^{-6} for the overall detection efficiency. The operation of this detector is described later.

4.3   Experimental Procedure

The actual experiment consists of loading the trap and evaporating to the desired $n - T$ phase space point, scanning the laser frequency through the resonance and counting the fluorescence. Since the detector is still quite sensitive to scaterred laser power we actually turn off the laser while applying the quench field and looking for the fluorescence. We take advantage of the fast decay of the 2S state in the presence of high E-fields to "open" the detector for a very short amount of time in order to minimize dark counts. This way we end up with a typical average of 0.02 dark counts per second of laser integration time.

Besides the frequency spectrum we also pursued three other laser measurements: the 2S decay time, the radial translation scan of the trap with respect to the laser beam and a measure of the photoionization rate. The goal with the 2S decay time experiment was to determine the order of magnitude of stray fields in our cell. This measurement is trivial but time consuming. After the laser is shut off, we introduce a variable delay before quenching the 2S atoms. By storing the counts due to diferent

delays in four separate counters we gather four data points to which an exponential decay is fit and the lifetime is extracted.

The radial translation scan experiment consists of offseting the trap axis with respect to the laser beam axis and recording the fluorescence for the different offsets. The offset is accomplished by changing the currents in the individual coils of the quadrupolar magnets. The interpretation of this measurement gets complicated by a variety of issues: angular misalignment between the axis of the trap and the laser, radiation trapping, pressure shift and broadening, and deformation of the trap at large offsets.

Photoionization is predicted to dominate the saturation behaviour for low power levels. A simple rate equation treatment as done in Part II suggests an easy way to measure its rate. In this measurement we simply vary the laser pulse width recording the fluorescence counts for each pulse width in a different counter.

The results of these experiments are described in Chapter 5. We now turn to a description of different systems in the apparatus.

4.4 Overview of Improvements

This section describes the improvements that made it possible to obtain the optical signal and perform the experiments described in this thesis. There were three major problems that prevented us from seeing the signal previously. The first problem was related to absorption of laser power on the windows, creating He vapour pressure. The evaporated He atoms quickly depleneshed our sample. This problem is not solved but it has been minimized. We have learned to treat the windows in the presence of the laser so as to avoid very large absorption. The construction of a cleaner gas handling system avoided the complete fogging of the windows we had observed in some previous cases during loading of the cell with He and H_2. The development of ^4He superfluid film pump reduced the losses by a factor of 5. These solutions are discussed in more detail in Section 4.5.

Second, the detector was being heavily saturated by the laser. In order to solve this problem we employed a Lyman$_\alpha$ band-pass filter and raised the temperature of operation of the detector. In debugging the operation of this detector we also improved its detection efficiency fourfold by biasing the photocathode positively with respect to the surrounding can. More discussion on the MCP is presented in Section 4.6.

Third, the laser was jumping frequency in excursions of the order of 100kHz which made the reproduction of small signals almost impossible. The source of this instability was in the temperature control of the reference cavity. Ground loops were a problem and the proportional servo system could not keep up with the changing environment. An integrating servo loop was implemented and brought the temperature

stability to better than $10^{-3}K$.

Besides fixing these major problems there were a series of improvements that turned out to be very important as well. Among these are: (1) - the narrowing of the search frequency range by better control over the Te_2 spectroscopy and through the measurement of a hydrogen atomic beam; (2) - a redesign of the beam delivery optics allowing direct and flexible control of the timing of the laser beam; (3) - the construction of a high performance beam delivering servo control and (4) - the implementation of a power controller that allowed precise measurement of the absorption through the fridge optics and that would allow the measurement of absorption through our sample at three times the shot-noise limit of 5 parts in 10^8 (for the conditions: 10s time constant, 1-10kHz modulation frequency, 3mW laser, $50\mu W$ on photodiode).

Most of these improvements were made before finding the signal. Since then, we have improved the stability of the laser system by identifying frequency variations on the 25kHz level due to table vibration. In order to identify the source of this frequency variation we employed FM spectroscopy of a strong 9MHz wide line in Te_2, obtaining a resolution better than 3kHz. During the process of studying the laser frequency jitter we have improved the lock of the laser to the reference cavity and we've measured a Doppler-induced frequency jitter of about $5 - 6kHz(@121nm)$. This seems to be our dominant source of broadening at present.

Some of the improvements above are described in more detail in the sections that follow.

4.5 Atom Loss by He Vapour

The optical windows in our cell can absorb a large fraction of the 243nm laser power. This is a serious problem in our experiment since a few percent absorption resulted in ^4He vapour that quickly destroyed the atomic sample, leaving no time for a systematic frequency search. A lot of effort was invested to find better optical coatings or good handling of the windows so that they would not show a higher than 5% absorption. This effort included experimenting with many different coatings in different vacuum environments, performing photoacoustics experiments and calorimetric measurements down to 1.2kelvin.

The basic conclusions of these experiments are three fold: 1 - this absorption is a surface effect due to deposition of contaminants on the windows under non-UHV conditions; 2 - laser assisted deposition of absorbers on the windows, supposedly hydrocarbons[52], can generate large absorptions ($> 10\%$) in minutes for laser intensities of few $mW/(mm^2)$ under non-UHV conditions; 3 - the presence of O_2 near the windows not only supresses the effect above but it can actually reverse the absorption through some sort of photoreaction that "burns" the surface contaminants.

Acting on this data, we changed the way we handled the optical system. The laser beam was never allowed in the cell at room temperature without the presence of O_2 (typically a few torr of 30% O_2, 70% He or N_2). The photocleaning method described above was employed for some duration of time prior to cooling down the apparatus. A new and cleaner gas handling system was built to avoid the complete fogging of the windows we had observed a few times when we loaded the cell with

H_2 and *He* at low temperature. Certain procedures were designed to speed up the loading and avoid degassing of the vacuum lines during that few minutes interval. Since then, we have never observed a round-trip loss increase of more than 5% due to gas loading into the cell. Actually, as soon as the gas is introduced, the laser can be partially scattered and absorbed and within a minute the return beam power is fully restored. This effect is not fully understood. One speculation is that it is due to accumulation of warm He on the bottom window until it all becomes superfluid.

Even with all the procedures above, our sample lifetime was still limited to a few tens of seconds for 2mW laser power. An old idea for pulling the superfluid film out of the cell after the load of the trap was made operational. The operation of this film pump consists of evaporating the film coming from the cell in a certain perimeter and making it recondense on a different surface. The little chamber where the superfluid accumulates is separated from the cell by the evaporator heater. Almost all the *He* evaporated in this heater recondenses in the chamber side and not in the cell side. This charming and useful device whose detailed operation will be described elsewhere[53] pulls the film (3% of saturated film) off our cell in about a minute and deposits about $600\mu W$ in the dilution fridge. The operation of this film pump was first characterized using a film burn-off measurement[43] with the bolometer and one can clearly see the film thinning as a function of time.

We performed atom loss measurements at different laser powers, different duty cycles and different cell temperatures. We found the mechanism responsible for these losses to be photonic in nature, i.e, a given number of photons absorbed on the windows generated the same percentual loss independently of laser duty cycle, power and

temperature for a limited range of variation of these parameters. Therefore the sample lifetime can be measured in energy scale or in number of photons. The operation of the film pump did not eliminate the problem but it did increase the sample lifetime by a factor of five. In a typical run the sample lifetime (1/e) was measured to be 240mJ of integrated laser power going into the fridge, which translates to about 24mJ absorbed at the windows. We believe that a He film residue is responsible for the remaining loss. Probably the monolayers close to the surface are not superfluid and slowly drift down towards the bottom window. This would provide a replenishing for a thin film coverage at the window, which happens to be the lowest point in the cell. Changing the geometry may yield much better results.

Another idea for greatly reducing this problem is to put the retro mirror inside the cell. If the mirror has a high reflection coefficient and is designed to have a node of the E-field at the surface, then there would be negligible power coupled to a thin absorber on the surface. A necessary condition for the absorber to be thin and at the E-field node is that the mirror coating be non-porous. Ignoring the absorber, the intensity at the surface is a factor of $(1 - R)^2/4$ times the average intensity of the standing wave. Since reflectivities(R) higher than 0.998 can be easily achieved this may result in a huge reduction of the light intensity at the absorber. The index of refraction of the absorber may play a role in redefing the position of the node or changing the reflectivity. Since these absorbers are not well characterized it is best to experiment with such a setup and measure the quantities of interest. This idea should also find application on the construction of high finesse cavities for laser frequencies in the blue, violet and UV. The joint operation of the film pump together with this

surface-node mirror may completely solve this atom loss problem.

Recently this atomic loss was remeasured to limit the sample lifetime to 13s for 5.8mW of laser power (75mJ as compared to the previous value of 240mJ). This may be due to the extra loads of *He* we added to the cell or because of alignment problems. At any rate this is a problem that requires an improved solution. One could then conceive of using the laser to tailor the atomic distribution or to promote laser induced evaporation.

4.6 MCP - L_α detection

As a L_α detector we use a stack of two microchannel plates from Galileo Elctro-Optics[50] in the so called Chevron configuration. I am not going to describe in details the operation of these plates as they are well documented in the literature by the manufacturers. Most of our findings about the low temperature behaviour of these plates are documented in Bitko's undergraduate thesis[54]. These plates operate under high voltage ($1000V$ per plate) and they are basically an array of about one million electron multipliers. To enhance the quantum efficiency at 121.5nm the top cathode is coated with a thin layer of CsI. With this coating the predicted quantum efficiency is 20

The stack of two of these plates in series provides a gain of about 10^6 under a condition known as space charge saturation, which allows for a nice discrimination between dark and real counts. The typical recharge time for the excited channels can be estimated from a simple RC time constant argument. The problem of operating such plates at low temperatures is that their resistance can be many $G\Omega$ below about 40K. With plates capacitances around 250pF the dead times can be of the order of a second this limits the linear regime (say 5% deviation from linear) count rate to few tens of k.counts/s.

In our case, the plates have a 40mm diameter and about half the plate is exposed to scattered light from the laser beam while the other half is mostly hidden from the scattered light by the retro-mirror assembly. This distorts the pulse height distribution since part of the plate could be saturated, generating small amplitude pulses,

while another non-saturated part would generate large amplitude pulses. Since we have a single anode to collect the electron showers, these diferent behaviours get mixed in the output. By watching the pulses in a scope one could easily assume that the plate was not saturated while, in fact, it was.

The cure for the saturation problem could be approached in three ways and so far we have employed two of those. First, by heating the plates up, the dead time is decreased and the detector can handle a higher count rate before it saturates. One problem that comes about from higher plates temperature is black-body radiation. This heats up the bolometer creating some diagnostic problems. A good black-body shield helped the situation.

The second solution is to increase the response contrast between L_α and the laser radiation. This was implemented by using a L_α band-pass filter from Acton[55]. The problem here is making a device with a good contrast and at the same time minimizing the L_α loss. We ended up with 10% transmission at L_α and 0.4% transmission at 243nm. The combination of a higher operating temperature(90K) and this filter eliminated the saturation problem at a cost of decreasing the signal by 10.

A third solution that has been preliminarily tried is to switch the MCP gain off when the laser is in the cell and switch it on for detection. A successful early trial switched the gain in few microseconds. That fast switching caused a temporary saturation of the preamp for few microseconds. This early trial indicated that such an idea will work easily if one allows for longer switching times. After performing the 2S decay time measurement we know that we can delay the detection by hundreds of microseconds after the laser is off without losing signal. By implementing gain

switching one should be able to remove the Lyman$_\alpha$ filter and recover a factor of 6 in signal. In addition one could operate the MCP at much lower temperatures which would allow for the usage of the bolometer.

The MCP voltage biasing circuit was designed with this switching idea in mind. A matched resistive and capacitive voltage division that accounts for the MCP capacitances, ensures a fast rise and fall time for the switched voltage. A small decrease in the voltage across the plates (800V) is sufficient to reduce the gain by orders of magnitude.

The biasing circuit is shown in Fig. 4-3.

The MCP quantum efficiency to L_α was measured using a Kr lamp from Opthos[56]. The Kr cell was excited by RF and the quoted spectrum was tested by moving a L_α filter in and out of the path between the lamp and the detector. We used the CsI coated MCP and a Hamamatsu[57] R972 solar blind photomultiplier as detectors. Both were used in photon counting mode by attenuating the source with a combination of a pinhole and another Ly_α filter. Using the quoted efficiency of the photomultiplier we arrived at a quantum efficiency of 6% for the MCP.

By biasing the surroundings of the MCP photocathode (top face) negativelly with respect to it, we were able to boost the quantum efficiency by over a factor of 4. The gain increased with the biasing voltage, eventually saturating at -120V. The idea for how this biasing works is as follows. About 1/2 of the MCP front surface is solid and not channelled. Many photoelectrons generated in this region are ejected from

114
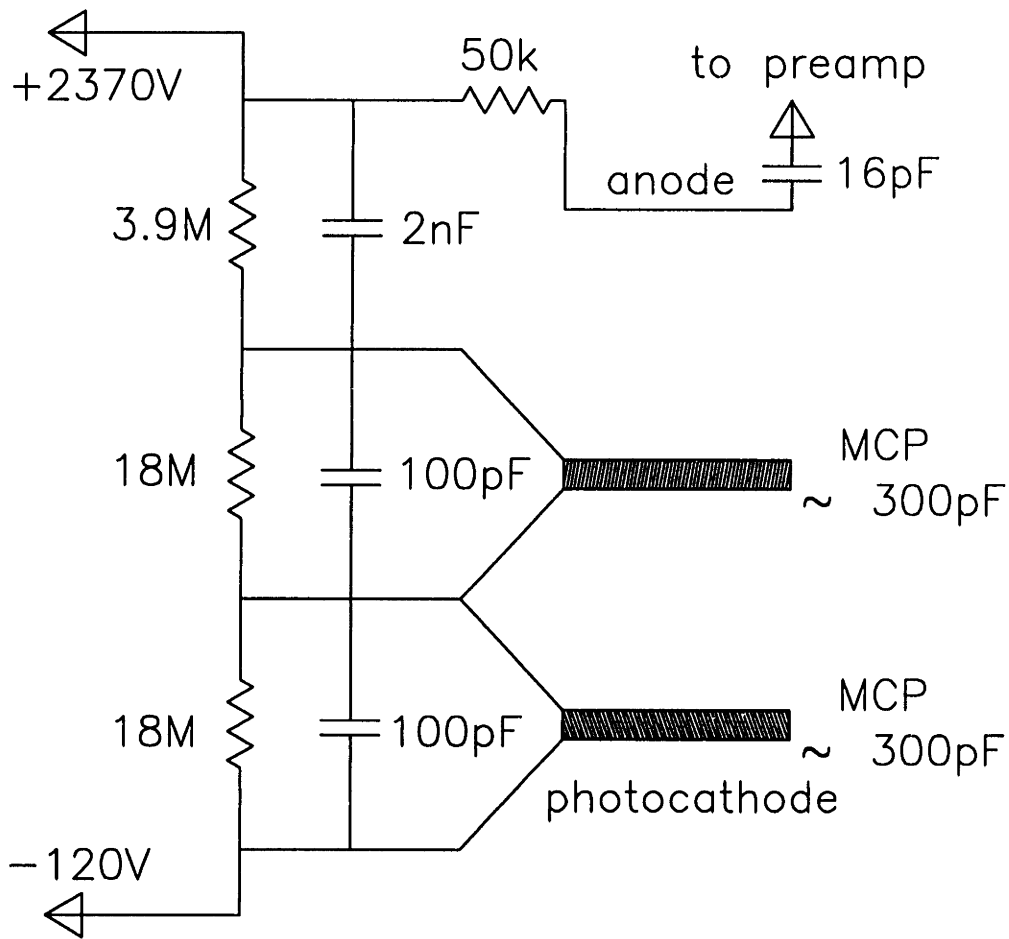
Figure 4-3: MCP biasing circuit. Designed to provide 1000V across each plate and to be switchable fast by maching the resistor network to the capacitance network..

the plates and never reach the channels. By aplying this biasing scheme, most of these photoelectrons would be detected. This accounts for a factor of 2 increase in the detection efficiency. The other factor of 2 may come from the effective solid angle of the CsI coating. The photons could first hit deep in the channel where there is no more coating (the coating extends down approximately 2 channel diameters) and have a much lower probability of causing a detectable pulse.

These plates must operate in a better than $10^{-5}T$ vacuum. In some instances, leaks produced ion feedback. Small He leaks are especially troublesome as they can cause arcing due to the low dielectric strength of He. Since we had a leak in the dilution refrigerator we decided to separate the MCP vacuum from that of the refrigerator. The MCP now has its own can and is pumped by an Ion pump.

With a good handling this is a great detector. It combines good detection efficiency (25%), low dark count rates ($< 10s^{-1}$), large detection area (40 mm dia.), fast response (ns), and reasonable dynamic range (depending on temperature). The independent vacuum space makes it possible to use this detector in an atmosphere with He what is not possible with PMT's because of He penetration of the glass enclosure.

4.7 Te$_2$ Spectroscopy

In this section I just want to give references to Te_2 spectroscopy relevant as a spectrometer for hydrogen spectroscopy and share some of our experimental studies.

We use a molecular $^{130}Te_2$ cell from Opthos[56] in an oven at 485^oC to perform saturation spectroscopy with the 486nm laser and identify the position of the hydrogen line. The i_2 transition was extensively studied by McIntyre[47] and others[48] for its use as a frequency marker for hydrogen spectroscopy. McIntyre predicts the line to be $57.1 \pm 0.6kHz$ above 1/4 of the hydrogen frequency (1S-2S : F=1) for the conditions: $T = 513^oC \Rightarrow P = 0.89(11)T \Rightarrow$ FWHM linewidth $\Delta\nu_{i_2} = 10.3(1)MHz$, with a total absorption through the cell of 23%(discounting the windows absorption) at the top of the Doppler line # 1284 in the $^{130}Te_2$ atlas[51].

After observing the hydrogen signal we have carefully analyzed the Te_2 scans, monitoring laser power, and linewidth. By χ^2 fitting the i_2 line (normalized to laser power squared) taking into account the strong and wide neighbohring line and comparing the center frequency to the hydrogen frequency, we have been able to predict the hydrogen frequency from the i_2 frequency and linewidth to better than 100kHz. A series of scans, using 2 different cells, was carefully analysed and compiled by Thomas Killian[58] for the following conditions: pump beam power/waist $\approx 16mW/0.5mm$; probe beam power/waist $\approx 2mW/0.3mm$; pump beam chopped at 8kHz by 84MHz AOM; lock-in detection at 300ms/12dB/oct; scan 20MHz, 200pts, 1s/point; cell temperature 485 ± 1^oC (non calibrated thermocouple). Under these conditions he predicts the hydrogen frequency (in MHz) to be

$$\frac{\nu_H}{4} = \nu_{i_2} - 59.01 + 0.17\gamma_{i_2} \pm 0.05 \qquad (4.1)$$

where $\Delta\nu_{i_2}$, the FWHM of the i_2 $^{130}Te_2$ line, typically varried from $10.3 - 11 MHz$. Even though the oven is temperature controlled, our cell temperature may varry somewhat. Different alignments may also be a cause of broadening.

4.7.1 Splitting a Te_2 line to few parts in 10^4

After we found the hydrogen signal we noticed the laser jumping frequency by 25kHz. Since the hydrogen experiment is time consuming and the results are not seen in real time we decided to invest some effort in resolving a Te_2 line to better than 5kHz. We picked a line that is about 32GHz to the blue of the i_2 line, under the lower frequency peak of a doublet Doppler structure. This line is 9MHz wide and about 30 times stronger than the i_2 line. There are no other visible lines under this Doppler profile. The Doppler width is approximately $0.9GHz$ with a peak absorption of 37%. By power controlling the laser beam and employing saturated FM spectroscopy[46] at 35MHz we were able to resolve this line to better than 3kHz in less than a second. Actually, after fixing the laser jitter problem we were left with a clean 60Hz signal showing a frequency modulation depth of 10-30kHz. We soon found out that this 60Hz signal was due to Zeeman modulation from the heater wires of the cell oven.

In conclusion we have used saturated spectroscopy in the i_2 line of Te_2 to be able to predict the hydrogen frequency with an uncertainty of 100kHz. We have performed

saturated FM spectroscopy in a much stronger $9MHz$ wide Te_2 line and were able to resolve laser frequency excursions to better than 3 parts in 10^4 of that linewidth on real time.

4.8 Laser Beam Steering systems

The description of the laser beam steering system that follows was written in a very detailed form a long time ago. Instead of editting and rewritting a more compact version I opted for keeping this version. The reader not interested on the details of this system can skip this section.

The physical separation between the laser source and the trapped atoms produces large drifts in beam alignments. The stringent requirements on beam overlap for Doppler-free 2-photon spectroscopy forced us to actively control the beam position as I describe below.

We have two actuators to steer the beam. One is located in the Optics Laboratory and it controls the position of the incoming beam at the top of refrigerator. The other one is at 4 kelvin, just below the cell, and it controls the retro beam alignment. The requirements for these two systems are different as the sources and amplitudes of noise are very different.

4.8.1 Incoming beam

The major sources of noise on the incoming beam pointing stability are believed to be air currents, slow building motion, and vibrations — possibly caused by large pumps and mechanical devices as we have in our basement and in the refrigerator control room. The typical power noise spectrum shows fluctuations with large amplitudes at 60Hz,120Hz and even extending to around 300Hz. Therefore we set as an initial goal to have a stable servo system that would have a unity gain point at 1kHz. For

this discussion and for the discussion of the power controller in the next section I will assume the reader to have some knowledge of control systems theory.

4.8.2   Position Sensitive Detectors

We use a PIN silicon photodiode with a resistive cathode from UDT[59] to monitor the beam position. The UDT -PIN 10D photodiode generates a photocurrent proportional to the incident light power and this current gets distributed to 4 terminals depending on the impedances towards those terminals as seen by the photoelectrons. If one connects the 4 terminals to the same "virtual" voltages, the current gets divided into each terminal according to the geometrical distance from the position where the photocurrent is originated and the terminals. With some electronics, these currents generate the proper error signal, i.e., the beam position. These photodiodes have a large active area with a correspondingly large capacitance, which requires some care with the electronics to avoid gain peaking and oscillations.

In order to achieve a high spatial resolution the optical system was designed to include a magnification of the beam as it reaches the PSD. This way any movement of the beam is also magnified and easily detected. In our case we had the beam covering a diameter of half a centimeter which gives us resolutions much better than a hundredth of a beam diameter.

4.8.3　Incoming beam pointing transducer : PZT

We chose piezoelectrics for the transducers for driving the beam pointing mirror because of their speed, low cost and smooth operation. The beam pointing assembly consists of 2 short bimorphs, a sandwich of two thin oppositely polled sheets of PZT that bends with applied voltage, and a custom made small dielectric mirror[60] with 3 support points separated by 3mm.

The two important parameters of this system are the dynamical range and the frequency response. The dynamical range, ie. angular excursion, is determined from the upper voltage limit, the PZT's coefficients and the geometries of the PZT and the mirror-PZT system. The frequency response is usually flat until the first resonance which is tyically determined by the spring-mass system. For a simple servo design one typically avoids resonances by constraining the system bandwidth to the flat response region. In order to push the resonance to as high a frequency as possible, it is necessary to use small masses and high spring constants and this why we used the smallest possible mirror that acomodated our beam.

The dynamic range in angle is given by

$$\Delta\theta = 2 \times \Delta z / \Delta L \qquad (4.2)$$

where the factor of 2 comes from the optical reflexion, $\Delta L = 3mm$ is the distance between the suport points, and (using expressions in catalog from EDO[61])

$$\Delta z = 3 \times d_{bim}V(\frac{L}{tck})^2 = 3 \times 300 \times 10^{-12}m/V \times 100V \times (\frac{0.2}{0.02})^2 = 9\mu m \quad (4.3)$$

for the typical bimorph coefficient d_{bim}, with 100 V across the device, $L = 0.2in.$ length and $tck = 0.02in.$ thickness. The angle then becomes $\Delta\theta = 6mrad$ which is more than enough to satisfy our requirements. The only reason for not going to an even shorter PZT is the difficulty of construction of very small structures.

Using the expression for a bimorph PZT 5H from EDO[61] we obtain for the resonance frequency of the PZT by itself:

$$N_1 = 1420Hz - m = \frac{3frL^2}{tck} \Rightarrow fr = 9.5kHz \quad (4.4)$$

for length $L = 0.2in.$ and thickness $tck = 0.02in..$ By weighting the mirror and the PZT one can estimate the decrease in resonance frequency. In our case we ended up with a resonance frequency at 7kHz.

The PZT's are soldered onto a PC board. The suport triangles are expoxied at the end of the PZT's and to the back of the mirror. The soldering should be done with low temperature Indium based solder to avoid overheating the PZT's as the Curie's temperatures for these polarized plates are around 200 ^oC. Also, the gluing should be done carefully as it could decrease the system's excursion. With the first resonance at $7kHz$ and a $6mrad$ of dynamic range this system is quite adequate for

our needs.

4.8.4 Incoming Beam Servo Electronics

The servo electronics consists of 3 blocks. The first is a normalizing circuit to make the error signal independent of laser power, which is achieved by a divider chip. This circuit works well for the typical working laser powers. If the power drops too low, it becomes very noise due to the small denominator.

The second block is the frequency dependent transfer function that takes into account the frequency response of the PZT and assumes a flat response of the PSPD, since it has a much higher bandwidth. This tranfer function has a 3-pole roll-off at low frequencies, turning into a 1-pole (single stage integrator) near the unity gain point and then increasing again to a 3-pole roll-off at higher frequencies. The frequencies where the number of poles is changed were originally designed to be 2 decades apart so as to give a good phase margin to the loop. Afterwards the values were changed slightly by monitoring stability and towards higher gains.

The third block consists of a moderate voltage amplifier that can provide $\pm 60V$ across the PZT's. A set of switches to flip the phase and exchange the 2 directions comes handy. As the dynamic range is large, when the system unlocks the beam tends to be placed a few centimeters away from the detector. This is a serious problem since there is no usefull error signal then. The simplest solution to the problem was to place a DIAC (or SBS) that almost shorts the voltage on the PZT until the system relocks. With this system the laser stays locked for many hours of hands free operation.

Unlocking and relocking events are rare and are usually caused by an unlocking of the UV generating cavity.

4.8.5 Retro-beam

The requirements for the retro-beam are very different (remember that the PZTs support the mirror in a vacuum can at 4K). First, a large excursion is desirable. Second, we have noticed in the past that the return beam drifts slowly (seconds time constant) with negligible high frequency variations. And third, the beam is chopped.

To meet these requirements we use long bimorph PZT's holding a high quality mirror, which is in a somewhat large substrate. With this system we get a resonance frequency around 450Hz and an excursion of Xdegrees/100V. A home built high voltage amplifier can drive the PZT's with an output of up to $\pm 650V$ and a bandwidth of 700Hz.

The error signal is detected with the same kind of detector used for the incoming beam and the servo electronics is simplified to a single pole. Since the return beam is chopped we employ a sample-and-holder that triggers on the beam power for developing the error signal.

Unfortunately, due to arcing of the PZT's at 250V, the system ended up with a very limited dynamical range. As such it is only able to control the alignment for a short time requiring manual adjustment of the beam alignment to bring the system back to its usefull range. Because of this, we no longer use this system, and we rely on infrequent manual alignments during the scan. By adjusting one of the lenses on top

of the refrigerator we can achieve the overlap of the incoming and retro beams. The alignment is first assessed visually in the optics lab and then the retro beam PSPD signal can be used to keep a good alignment during the scan.

4.8.6 Conclusion

The incoming beam is actively positioned at the top of the refrigerator to about one hundredth of its diameter. The retro-beam steering did not show enough dynamic range to be useful, so the overlap of the two beams is adjusted manually with a micrometer mounted lens on top of the refrigerator. During the night, when the alignment is much quieter, a typical scan requires adjusting the overlap of the beams once every 5 minutes. The typical misalignment allowed is about a quarter of the beam diameter. By installing actuators on the optical mount that is now used for manual alignment this system could easily be electronically controlled.

4.9 Power Controller & Absorption

The development of a high performance power controller was needed for three different purposes. The first one has to do with the study of lineshapes.

The 2-photon transition rate scales with the square of the laser power at 243nm. Since the 243nm is generated by doubling 486nm, it also depends quadratically on the 486nm laser power. Therefore, in order to be able to study lineshapes without this huge power induced noise, we have to either measure the average laser power for each fluorescence cycle and do post-processing of the data or actively control the laser power before it reaches the atoms.

The second motivation was that with all the problems we had with window absorption, we needed an accurate way of measuring changes in laser power transmission through the optical windows in our system.

The third purpose for which we built this power controller was for measuring hydrogen absorption of 243nm in the trap. Uncertainties related to the fluorescence detection prompted a search for other detection techniques. These uncertainties had to do with stray electric fields causing fluorescence to ocurr before one could effectively activate the detector counter, possible anomalies in the transmission of L_α by cold MgF_2 windows and L_α radiation trapping. So a measurement that did not rely on the detection of L_α and that could be implemented without adding components to the refrigerator was highly desirable.

An absorption measurement of the sample would be possible if one can detect few parts in 10^6 with a second time constant. A 1mW beam carries 10^{15} photons a

second. If such a beam is absorbed by a photodiode, the shot-noise limit would be 3 parts in 10^8. By estimating the noise from photodiodes and electronics it is clear that this is a hard experiment to perform but it might be possible if one uses many available tricks such as power controlling the input beam, doing differential detection and performing lock-in integration on a zero background. One possible modulation scheme is Stark shifting the transition frequency.

The major unknown in the absorption measurement has to do with the refrigerator and optics vibrations and actual electronic noise. We are trying to see changes of 1 part in 10^6 in the power of a beam that has to pass through many small apertures in the refrigerator and make it back into the detector. That final noise we end up with was determined experimentally and it is discussed later on in this section.

4.9.1 Power Controller

The existance of an AOM in the optical path allows for a very nice control of the laser power. By servoing the RF amplitude into the AOM, one controls the difraction efficiency of the modulator. The bandwidth one can achieve with this system is quite large, typically above 100kHz, and it depends on the bandwidth of the light detector, the AOM bandwidth, (which is usually determined by the transit time of the sound wave) and the bandwdith of the RF acuator used to control the RF power.

Since an efficient power controller should not draw much power from the beam, we use a mere 3% reflection off a window to monitor the power. The major problem with measuring small powers in the UV with photodiodes is the fact that they usually have

a much higher efficiency in the visible than in the UV. Thus, stray light is a serious problem as the controller corrects for the total integrated response. Ideally one wants to use a spectral filter in the photodiode, something we have not implemented. Some care has to be exercised on the choice of the gain in the first amplification stage since this is usually related to the response bandwidth. Also as one uses a fast photodiode in a photoconductive mode with a resonable gain, the noise equivalent power of the circuit is intrinsically larger than otherwise. So some design compromises have to be made.

In the optical design I made sure that the transit time of the sound wave through the beam in the AOM be kept small by having a small beam waist at the AOM. The AOM manufacturer provides the speed of sound in the media and the rise time. Unfortunately they do not always provide the time delay for a square pulse, for example. And these delays can become the limiting factor in the implementation of such a power controller.

As an RF switch I employed two cascaded mixers (Minicircuits ZFAM-2000[62]. By applying voltage to the IF port one controls the coupling from Local Oscillator port into the RF port. The circuits are shown in Fig. 4-5 and Fig. 4-4. The exact elements for the transfer function were determined experimentally by modifying the original calculated values. Once the loop is closed the output of the measuring photodiode displays a DC stability of about than 1 part in 10^4 as determined by the PMI voltage reference REF-08[63] and local variations of temperature. The 0dB point ocurrs at around 100kHz.
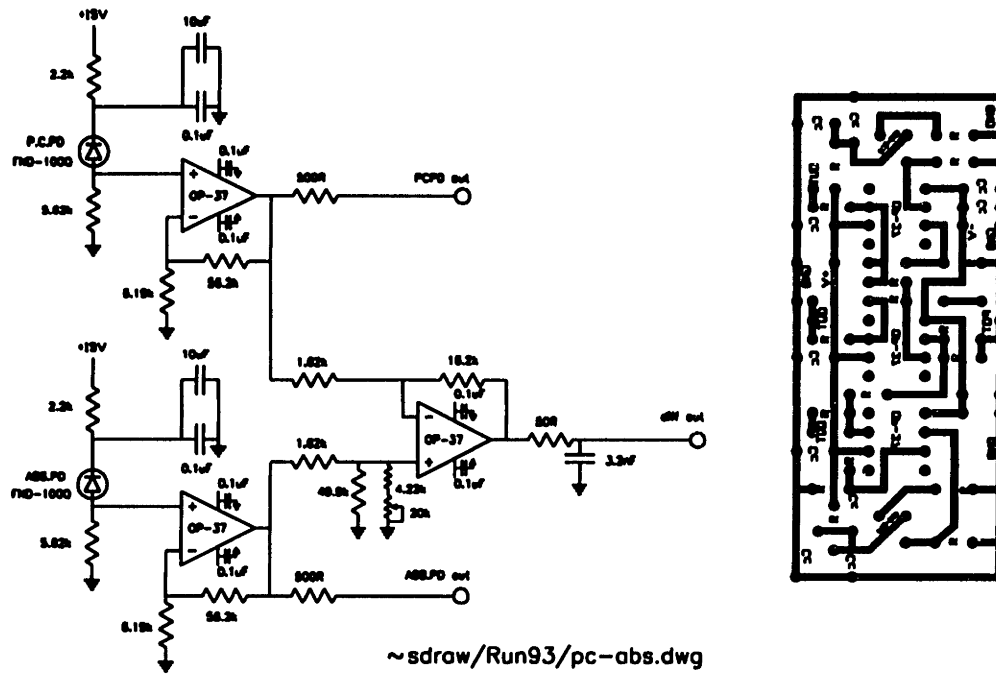
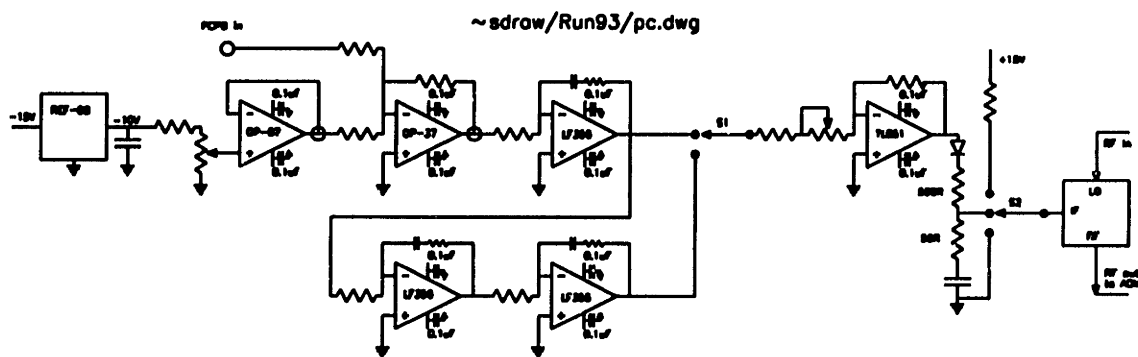Figure 4-4: Differential absorption measurement electronics.

Figure 4-5: Power controller circuit.

130

4.9.2 Absorption

In order to perform an absorption measurement, we power control the incoming beam, and subtract the return beam power from a scaled incoming beam power such that the difference is normally close to zero. The output of this subtraction circuit is then fed into a lock-in that also generates the modulation control signal. As a modulation scheme we can use the Stark shift of the line. We have tried this scheme with no atoms in the cell, in a previous run, and found a background noise of 3 parts in 10^7. This is just a factor of 3 above the photonic shot-noise for the experimental conditions.

Under good experimental conditions we should be able to detect the atomic absorption with a signal to background noise of 100. This experiment was not tried in this experimental run because the beam is hitting the sides of the cell and only 70% of the beam mode is returning to the photodiode. This situation produces much larger background noise due to vibrations.

This absorption measurement complements the fluorescence measurement in many ways. While the fluorescence could be subject to radiation trapping, the absorption is not. Most of the noise in the fluorescence is the signal's shot-noise and very little background noise, while in the absorption signal it is mostly background noise. In our case we have no particular motivation right now to perform an absorption experiment. The absorption measurement remains as a backup detection technique that could be used in case the primary technique stops working due to failure of the MCP.

Chapter 5

Data and Analysis

In this chapter we present, discuss, and analyze the experimental data. The procedures for the various experiments were described in Section 4.3.

5.1   First Observations of the 1S-2S Transition

Fig. 5-1 shows some of the first observations of the 1S-2S fluorescence signal. We describe here some of the features of the signal and a little of the history of the improvements that were essential for performing the experiments described in this chapter. The predictions for signal to noise ratio were about 10-30, but the observed signal to noise ratio is typically smaller by a factor 5-10. The low predicted signal to noise ratio in these scans is due to a series of suboptimal experimental conditions:

(1) low laser power - *the dye laser power had been slowly degrading for a year, decreasing from 500mW to 300mW. Because the 1S-2S signal varies as the fourth power of the dye laser power, this was a serious problem. We later discovered that*
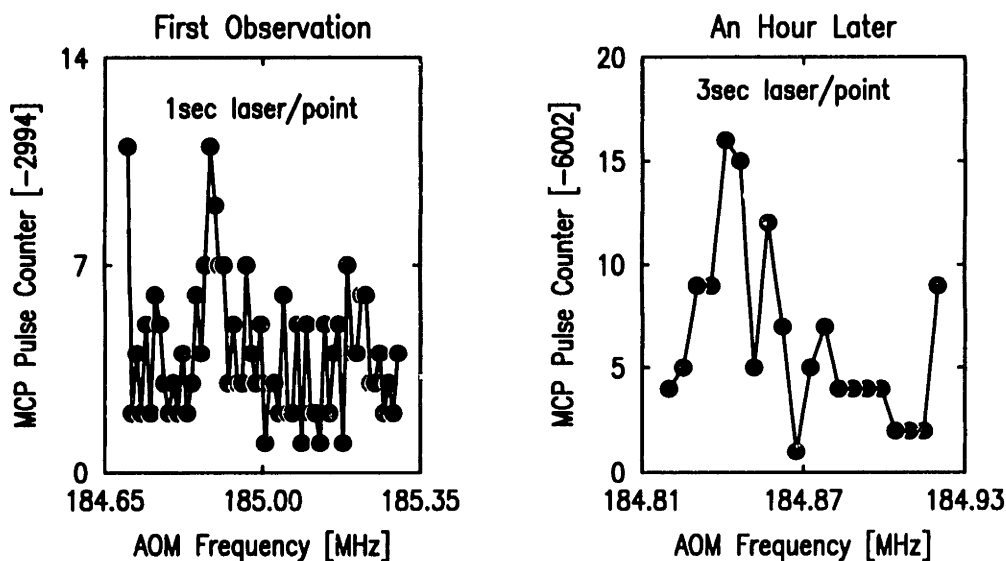
First Observation

An Hour Later

1sec laser/point

3sec laser/point

MCP Pulse Counter [-2994]

MCP Pulse Counter [-6002]

14

7

0

184.65   185.00   185.35

AOM Frequency [MHz]

20

15

10

5

0

184.81   184.87   184.93

AOM Frequency [MHz]

Figure 5-1: Initial Scans..

the problem was due to slow clogging of the dye jet nozzle;

(2) low density $(10^{11}cm^{-3})$ - *because of concerns about the overlap of the laser beam with the atomic sample, we opened the trap in the radial direction, which lowered the density;*

(3) poor duty cycle (relatively short laser time and long detector exposure time) - *we originally had limited knowledge of the stray E-fields and the effectiveness of the quench plates on the 2S decay time. So, we conservativelly set our scan parameters to relatively short laser pulses and long quench/count times (150µs of laser on time and 30µs of count time)*;

(4) less than perfect alignment between laser beam and trap axis - *we later discovered this from the radial translation scans of the trap;*

(5) bugs in the software and counter electronics - *they were fixed later.*

It turned out that optimizing our initial signal was not an easy task. We first tried

many simple and small changes in trapping and scanning parameters, but none gave significant improvement. Sometimes the signal would disappear, and uncontrolled changes on a signal this small made it impossible to establish the reality of any improvement. We needed a large improvement which could be detected beyond the signal variation.

Eventually we found that drift in the reference cavity was a major source of the problem. A large number of scans served to map the reference cavity drift. The refence cavity showed an almost linear drift ten times larger than it should have been, based on extrapolations and interpolations of Te_2 scans over the course of many days. The failure to get a repeated series of scans on the next day, coupled with a complete misbehaviour of the laser frequency as evidenced on the Te_2 frequency, pointed to serious problems with the reference cavity. The laser appeared to be jumping frequency in 100-200 kHz steps. The problem with the cavity was found to be a partially malfunctioning temperature controller, which was replaced.

Before continuing with the discussion of the data, we briefly disgress to recount a little story that illustrates how bad events sometimes have good consequences. For a few years our dilution refrigerator had been leaking He into the vacuum space. The leak was too small to localize and fix, but since it was so small, we could operate the fridge by inserting a cup of activated charcoal in the vacuum space. Charcoal adsorbs He provided that the it is cold enough, which made starting the refrigerator a challenging enterprise. The refrigerator operated for many runs, but only in a time consuming and unreliable way.

Just prior to this run, this leak opened up more, making a cool down impossible.

Fortunately, the leak had become so large that it was localizable, and thus fixable. Fixable it was, but not guaranteed to be fixed in any reasonable length of time. The leak was in a "step" heat exchanger and was quickly fixed using the same soft solder used during manufacturing. We now have a turn-key, reliable, dilution refrigerator, thanks to that leak having become much bigger.

A similar story happened with our laser. This time, a clog replaces the leak. We were frustrated by how little power we were getting from the laser. After numerous realignments and dye changes the situation worsened to the point that the laser power was insuficient for the experiment. One more dye change revealed the source of the problem. The length of the jet suddently became so short that it was clear that the nozzle had clogged. Once again, a drastic failure allowed us to fix a major problem.

After these fixes we started getting improvements in our signal to noise ratio.

5.2 Radial Translation Scans of the Trap

We could measure the density distribution as a function of position by keeping the laser in the center of the cell and displacing the atoms with offset currents in the individual coils of the quadrupole magnets. From the known field profile we could extract density as a function of energy, which gives the Boltzmann factor and thus temperature. Using this procedure, we could also determine the best alignment for the laser beam-atoms system. In these experiments the laser frequency was kept constant or was scanned across a very limited frequency range.

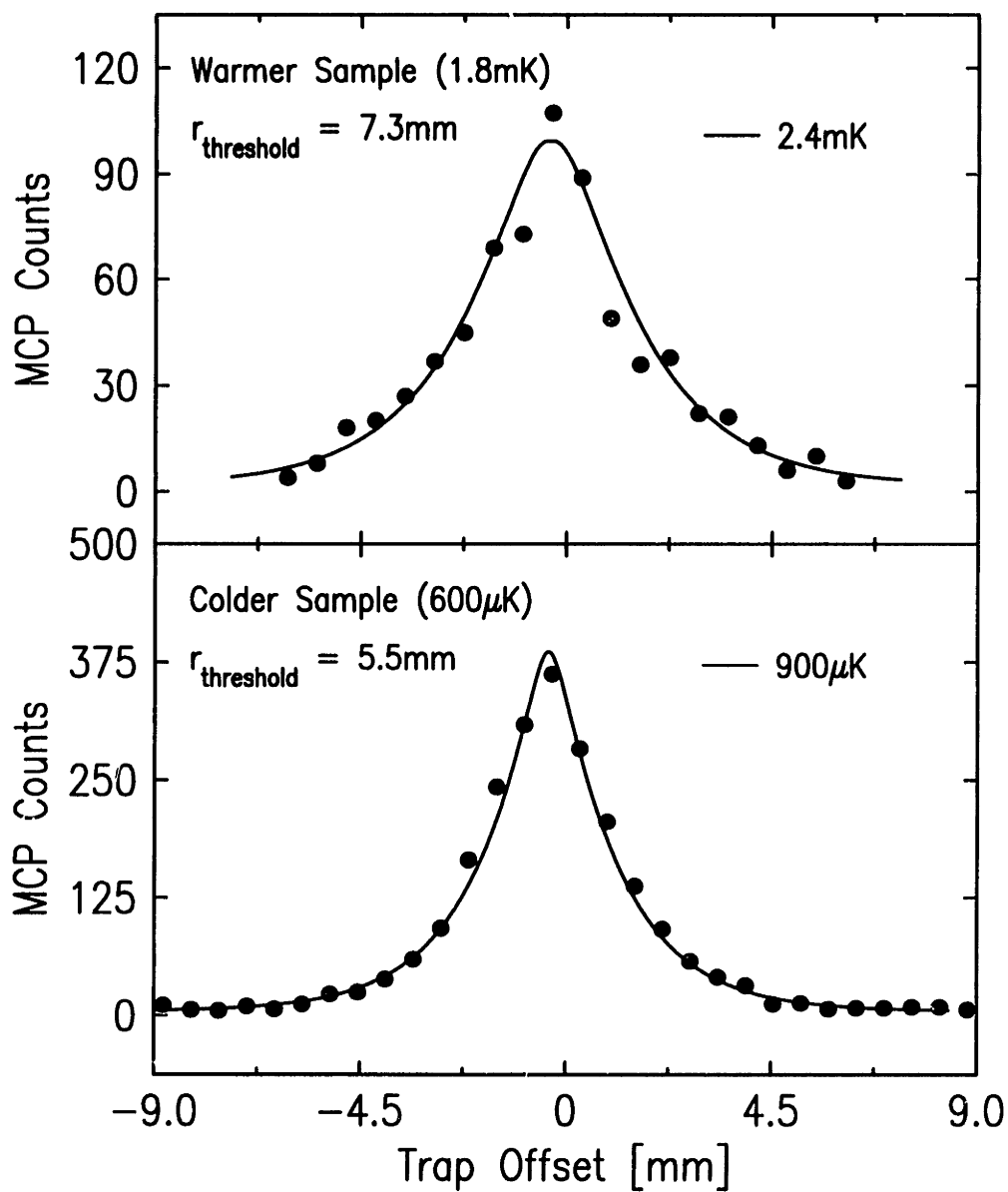Fig. 5-2 shows two such scans. One was taken at low density and high temper-

Figure 5-2: Translation scans of the trap. "$r_{threshold}$" is the translation distance at which the field is at the trap threshold value. .

ature, the other was taken at higher density and a much colder temperature. The solid lines represent a fit for the sample temperature. We believe from independent measurement using the bolometeric technique traces that the scan in Fig. 5-2.a shows a reasonable agreement between the bolometer temperature measurement and laser data. The scan in Fig. 5-2.b, however, is off in the temperature measurement by 50% too high. Other measurements were done at colder temperatures and higher densities where the discrepancy was even higher.

At this stage it is important to remind ourselves of how many things could complicate this kind of measurement. First, there may be an angular misalignment between the axis of the trap and that of the laser beam. We estimate the maximum angle to be $\theta_{max} \approx 4mrad$. In these cases the trap length was longer than the beam divergence length of 4cm, which means that the signal would be essentially flat for a trap displacement of $160\mu m$.

The other complications have to do with L_α radiation trapping and a possible density shift of the transition frequency. In order to pursue this technique we must improve our laser stability. Once the laser is made more stable, one can measure the density-induced frequency shift and one can also measure the effect of radiation trapping. However, by then the appeal for this measurement as a temperature diagnostic will have faded since the spectral linewidth provides a more direct measurement. As a spatial probe, though, it should be very useful for the study of BEC, superfluidity, interactions, etc.

These translational scans provided us data on the offset of the laser beam from the trap axis, and by using this information we achieved some gain in signal to noise

ratio for the other experiments.

5.3 Semiclassical Time-of-Flight Spectrum

In the ideal scenario — a monochromatic laser, perfect alignment, sample in thermal equilibrium in a region much shorter than the laser beam divergence length — the predicted time-of-flight spectrum has an exponential lineshape (see Chapter 2) with a FWHM linewidth (@243nm) of

$$\frac{\gamma_{tof}}{2\pi} = \frac{ln2}{2\pi} \frac{\sqrt{2kT/m}}{w_0} = 0.39 \times 10^6 \sqrt{T} (Hz/\sqrt{K}), \qquad (5.1)$$

for $w_0 = 36\mu m$. Fig. 5-3 show scans taken for different temperatures and at slightly varying conditions such as alignment, laser power, and, probably, laser jitter. The solid lines are fits to exponentials with the displayed linewidth.

As we will see, turning the spectral linewidth into a temperature with high accuracy is a complicated matter. With some improvements, though, we should be able to measure temperatures to better than 15% accuracy. We now consider a range of effects that can affect this measurement such as the effective beam waist, beam misalignment, radiation trapping and laser frequency jitter.

Even though we had carefully measured the beam waist in the trap region, in this particular run 30% of the beam was occluded due to alignment problems. This is easily fixable, but it poses a question of the effective beam waist in this particular
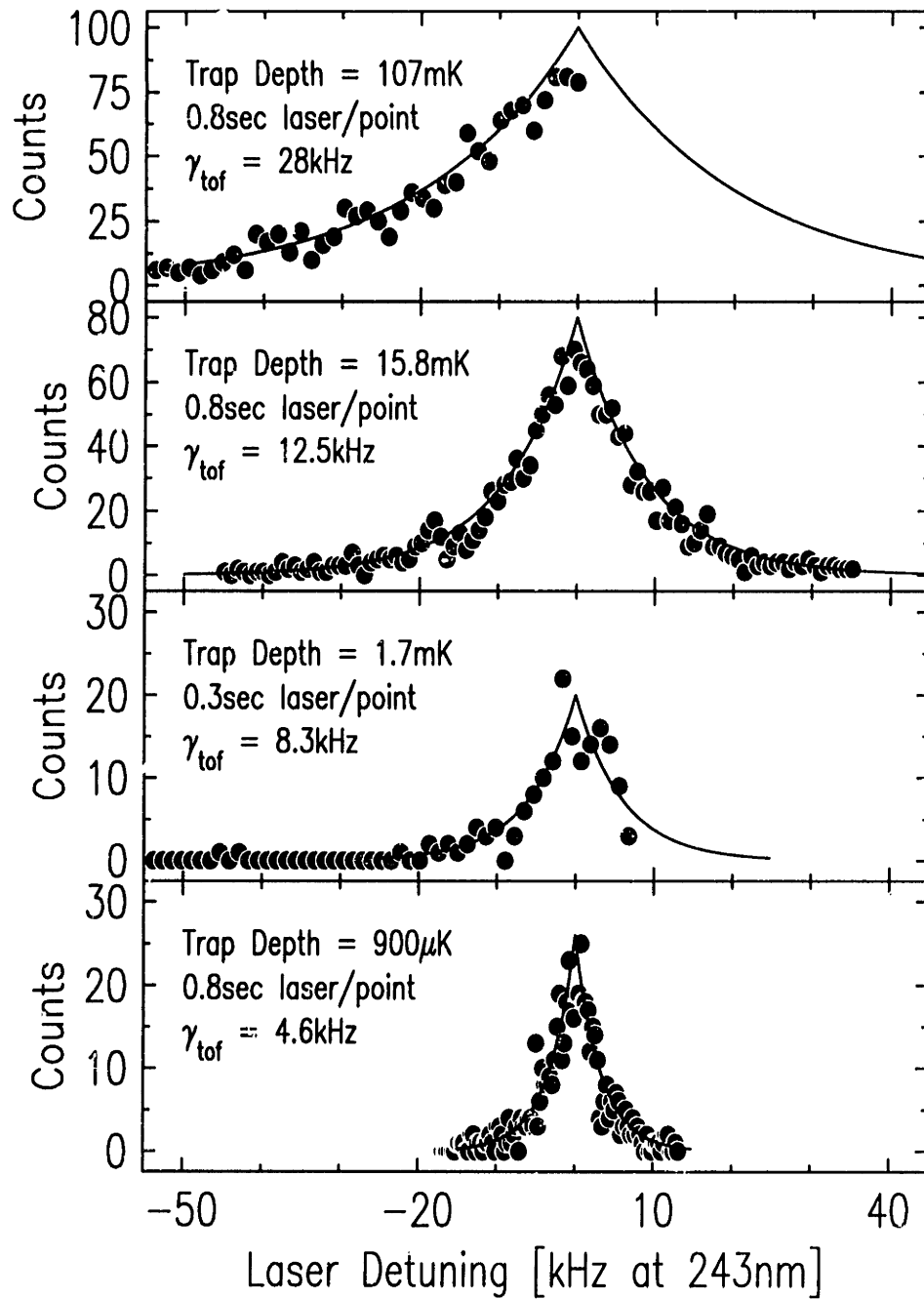
Figure 5-3: Spectra for trap depth varying from $900 \mu K$ to 107 mK with the fitted time-of-flight lineshape and FWHM linewidth.

run.

When the sample is longer than the beam divergence length, the exact computation of the linewidth is quite complicated and depends on the specific variation of the density along the beam axis. C. Bordé[19] has obtained expressions for the lineshape in the case of constant density in terms of exponential integral functions[64]. We have treated the case of a harmonic potential along the beam axis and find solutions in terms of the error function (see Section 2.5).

In order to provide a quick fit for the temperature, we have developed the approximation below. In Complement II and III of Chapter 2 we found that, for a colemated laser beam of waist w_0, the peak transition rate is proportional to $1/w_0$. The beam waist varies along the z-axis according to $w(z) = w_0(1 + z^2/z_0^2)^{1/2}$. If the divergence length is much longer than the beam waist, the waist seen by an atom during the interaction time is approximately the local, almost constant beam waist. One can then integrate the exponential spectra at different z-positions and with different waists to obtain the lineshape

$$W(\Omega) \propto \int \frac{n(z)e^{[-(1+z^2/z_0^2)^{1/2}\Omega/\Delta\Omega]}}{(1 + z^2/z_0^2)^{1/2}}dz \tag{5.2}$$

where $n(z)$ is the density, Ω is the detuning and $\Delta\Omega = \sqrt{2kT/m}/(2w_0)$ is the $1/e$ linewidth at 243nm. The equation above can be easily integrated numerically. For a trap about 16 times longer than the beam divergence length (a typical case for most of our data), one can easily obtain an effective beam waist that is twice the

minimum waist. Therefore, in order to measure temperature accurately, one has to acount properly for the effective beam waist. Incorporating radiation trapping is a trivial matter if the reabsorption cross section for the emitted L_α radiation is well known (see Jon Sandberg's thesis[28]).

The best strategy for dealing with all the complications due to the varying beam waist is to avoid them by making the beam waist bigger, and consequently increasing the divergence length, which varies as the square of the waist. With the axial compressed trap, as we normaly use, an increase in the beam waist by a factor of two would avoid any problem on the interpretation of the spectral linewidth.

If the return beam is not perfectly aligned to the incoming beam, one can expect two effects: a residual first order Doppler effect and a decrease of the transition rate. Somewhat unexpectedly, a misalignment does not change the effective beam waist at a given point. The residual Doppler effect linewidth can be easily estimated in our case to be about 8% of the time-of-flight linewidth for a large misalignment of 40% of a beam waist ($\theta = 0.4w_0/300mm = 5 \times 10^{-5}$). For this misalignment the reduction in signal is 16%.

If the laser frequency jitters uniformly — square distribution — across a small frequency range ($< \gamma_{tof}$), it is easy to see that the time-of-flight spectrum will be flattened on the peak. If one neglectes the flattened region in the peak and fits the wings of the spectrum to an exponential, one obtains the original linewidth of the time-of-flight spectrum. Use of the spectral wings for fitting a line can be helpfull to avoid accounting for saturation and depletion of the population of low energy atoms.

5.4 Spectroscopy of Quantized Atomic Motion in the Trap

In Chapter 2 we quantized the motion of the atoms in the trap and predicted the appearance of sidebands modulating the time-of-flight lineshape. When the sideband contrast is good, the resolution is no longer limited by time-of-flight. The scans in Figs. 5-4 and 5-5 show sidebands. Notice our best estimate for the trap oscillation frequency from our knowledge of the fields and the frequency splitting measured in the scans. Also notice, that out in the wings of the lines the splitting starts decreasing. The fast atoms are the ones contributing the most to the wings of the line and those are the ones sampling the trap unharmonicity. Saturation is clearly present in all these scans.

To analyze our spectral data, however, we encounter a few problems that we did not include in our analysis. One is the effect of anharmonicity in the trap shape. The trap is harmonic only at the bottom. If the temperature is not low enough, a large fraction of the atoms will not be in the harmonic trap but in a linear quadrupolar trap. In a linear trap the separation between trap states becomes smaller as the energy increases.

The second effect is saturation, including photoionization, and the resonant depletion of atoms. At high compression and cold temperature, the transition rate for most atoms is more than $1s^{-1}$. Therefore the resonant laser ejection of atoms cannot be neglected for scan times of the order of a second. While one can learn about the repopulation process through the study of resonant laser ejection, for high resolution
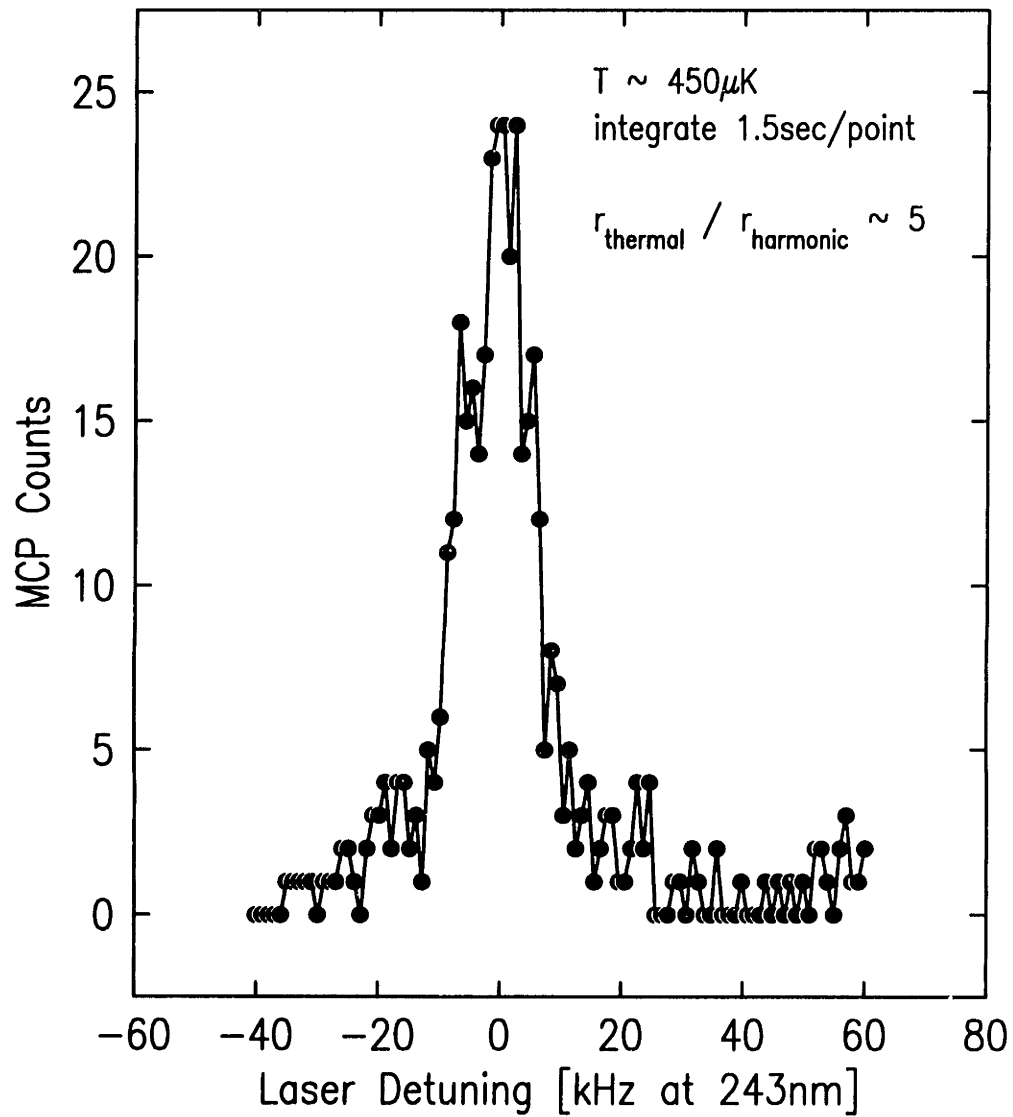
Typical Scan of Cold Sample

Figure 5-4: Spectrum showing sidebands.

spectroscopy we would like to avoid it instead of learning to account for it. We have repeatedly decreased our laser power in trying to keep laser ejection and photoionization to a minimum. Nevertheless, it will become evident from our spectra that saturation is important.

A major advance in the spectroscopy of hydrogen is possible, but first it is essential to reduce the laser frequency jitter and to improve the detection efficiency. This will allow the laser power to be reduced which simplifies almost every aspect of the experiment. For this reason we feel that it is just not worth the effort under our present conditions to try to account for the lineshape in detail.

The contrast of the sidebands is determined by the ratio of the trap oscillation frequency to the effective laser linewidth. The fit in Fig. 5-5 used 2kHz for the laser linewidth. This value is in good agreement with the previously measured Doppler induced frequency jitter.

By resolving the sidebands one can preferentially address different classes of atoms by positioning the laser frequency in different sidebands. At the outermost sidebands, the laser interacts only with atoms that have the highest transverse energy, while at the center peak, it interacts more strongly with the low energy atoms. This should allow for velocity selective experiments including laser induced evaporation[65][66].

These sidebands, which in our formalism, originate in transitions between different trap states, would also appear in a semiclassical formulation where the atom is allowed to go back and fourth through the laser beam. In this case, one generally ignores the transfer of kinetic energy between the laser and the atoms. It is interesting, though, that if we can realize BEC in our trap, we should be able to see sidebands, due to the
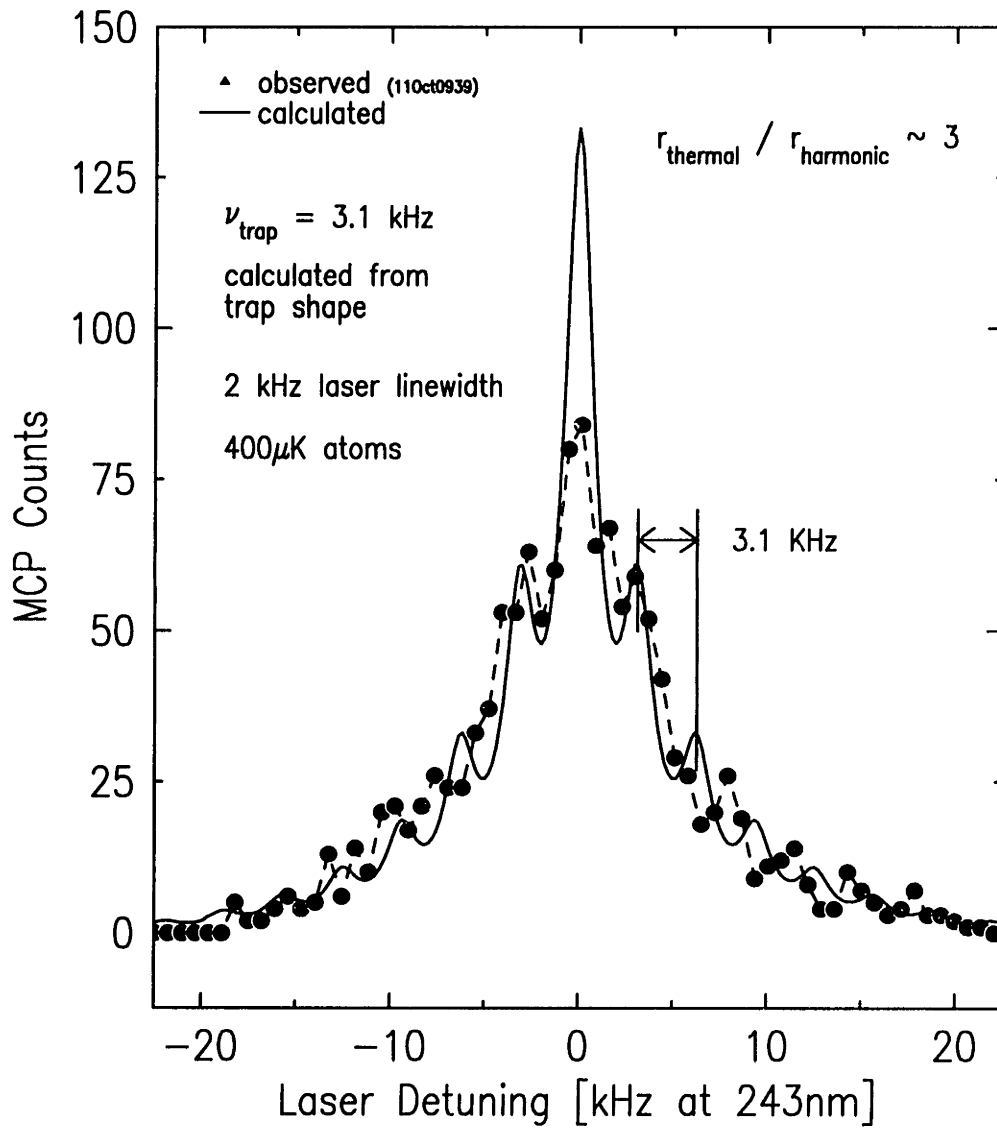
Figure 5-5: Spectrum showing sidebands. The calculated trap oscillation frequency is for the bottom of the trap. Approximately half the atoms are sampling the harmonic potential. The mismatch of the peaks away from line center is attributed to anharmonicity of the trap.

condensate, only on the high frequency side of the line center since an atom excited out of the condensate can only go to higher trap energy. This cannot be duplicated by a semiclassical treatment that ignores momentum transfer.

5.5 Lifetime of the Hydrogen 2S Metastable State

The direct observation of the 2S lifetime is a nice example of what a trap allows one to do. Such a measurement would be almost impossible in a hydrogen atomic beam because of the long lifetime and high speed of hydrogen. Even with a beam cooled to 4K, it would be required to propagate the beam for 50m!

The decay rate of the 2S state varies with the square of the local electric field (see Complement 3.I). Therefore a measurement of the 2S lifetime can be used to measure or set a limit on stray or applied fields. By avoiding such fields one can experimentally verify the 2S decay calculation.

Following the procedure described in Section 4.3, we have measured the 2S lifetime in many diferent trap shapes and temperatures. Fig. 5-6 shows two such measurements. We have measured reproducible decay time constants between 40ms and 116ms. These are to be compared to the predicted natural decay time of 122ms.

The reason for different decay rates in different traps is not yet completely clear. That are a few effects that interfere in this measurement. The first is stray fields. These fields should be larger close to the walls than in the center of the cell. Therefore, a sample confined tightly in the trap axis benefits from a very low stray electric field. A second has to do with the angular distribution for emission of the L_α fluorescence,
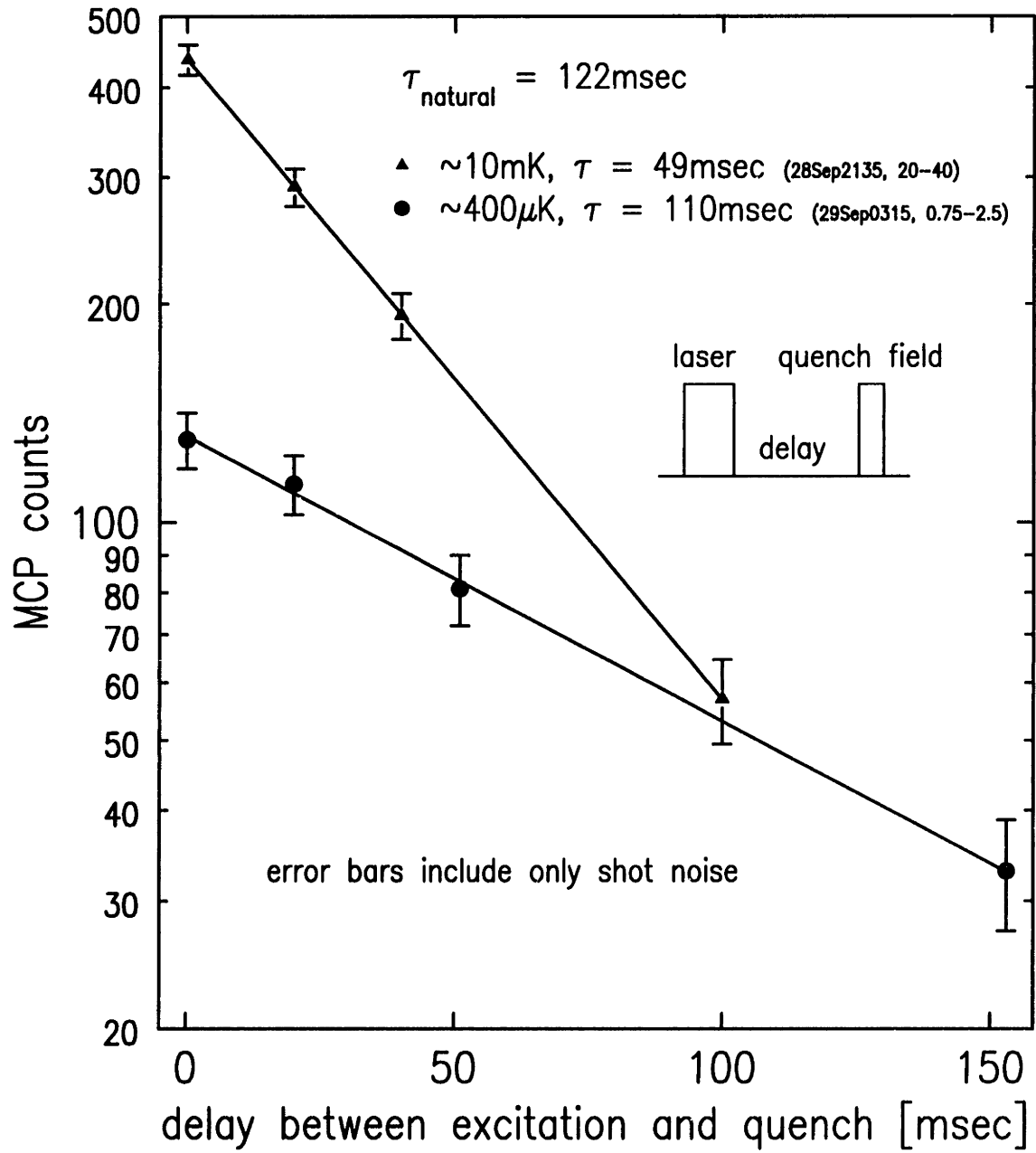
Figure 5-6: 2S lifetime measurement. The two sets of data points are for different traps with different compressions.

that depends on the direction of the local magnetic field[28] and that also depends on the particle energy. These two effects can be reduced by using a very cold and compressed sample in a large bias magnetic field.

Other effects can also play a role in this measurement including effects due to photoions and photoelectrons, and also inelastic collisions. The number of generated photoions can be much larger than the actual number of excited atoms if one is not careful with the excitation timing and power (see Complement 3.II). These photoions and photoelectrons could persist in the trap for a long time undergoing cyclotron motion and inducing 2S decay. To my knowledge, there are no rigorous estimate for 2S-1S inelastic cross section at these enegy ranges. To minimize these effects, if they are relevant, one would like to work with low densities and carefully control the excitation.

Once the laser frequency jitter is minimized, a precise measurement of the 2S lifetime should be possible. One would selectively excite slow or fast atoms in a sample. In the same trap load, one could study atoms that reach close to walls and atoms that remain mainly in the center of the cell. One could also study and control photoionization and look for its influence on the 2S decay rate. The increase of detection efficiency described in Chapter 6 would greatly benefit this experiment, by shortening its duration or by allowing lower levels of excitation. We believe that this measurement could be pursued to a few percent accuracy level, and probably better.

5.6 Photoionization and Saturation of the Fluorescence Spectrum

For this discussion, we consider as saturation any mechanism that would make the excited state population deviate from a linear growth in time, i.e., any loss mechanism. From these saturation processes, we expected the rate of photoionization to dominate over those of spontaneous emission, inelastic collisions, laser excitation and stimulated emission (see discussion in Complement 3.II).

We attempted to measure the photoionization rate by exciting the sample on resonance for various times before quenching the atoms. A plateau in the signal would indicate that the loss rate equals the excitation rate. Assuming that the loss rate is predominantly due to photoionization, the photoionization rate could be determined. The photoionization rate of the 2S state should scale linearly with laser power.

We performed the measurement for three different laser powers. We show data for one of these measurements in the insert of Fig. 5-7 together with the fitted saturation rate. Fig. 5-7 also shows the fitted saturation rates versus laser power. Clearly these points do not lay in a straight line indicating that some other loss mechanism is present. The most probable candidates is depletion of 1S atoms either by resonant loss or by He vapour.

If photoionization is assumed to be the dominant mechanism at the lowest laser power, the photoionization rate for the thermal sample can be directly read from the figure. The thermal photoionization rate averages the photoionization rate for atoms that spend all the varying fractions of time in the laser beam. The photoionization
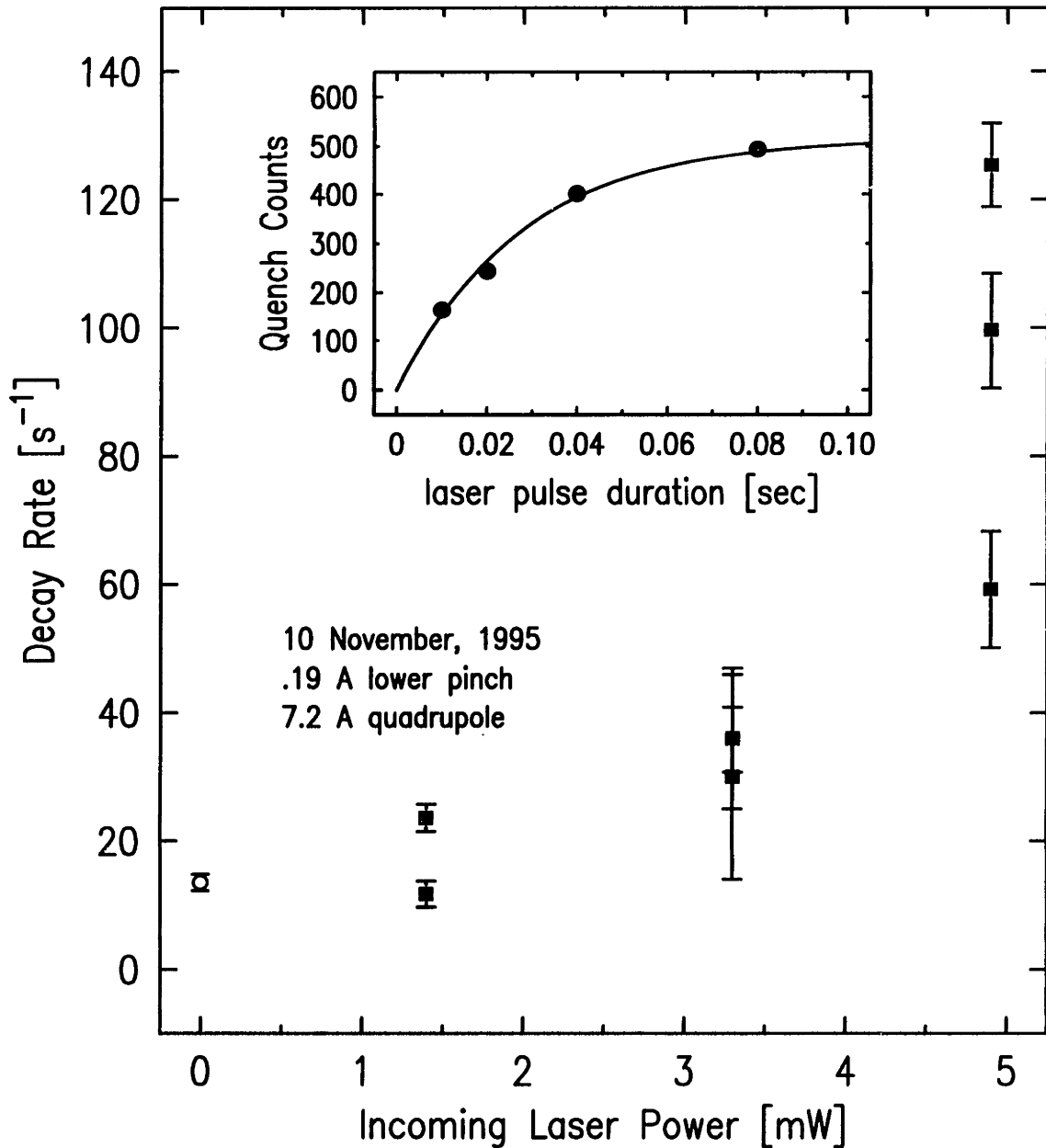
Figure 5-7: Saturation study of the 2S state. The insert shows the fit to one decay rate. The main figure shows the sets of decay rates for different laser powers. The point at zero laser power represents a measure of the 2S decay for the same trap taken in the same day.

rate of the 2S state could be easily obtained from this thermal photoionization rate data (Fig. 5-7 by incorporating photoionization into the theory presented in Chapter 2 provided that the excitation times are longer than the trap oscillation period and the laser frequency detuning is known.

A quick estimate on the expected photoionization rate for the data in Fig. 5-7 goes as follows. Using Eq. 2.48 one can easily estimate the average laser intensity seen by an atom in the n-th state of the trap: $< I(n) > /I_0 \approx [\sqrt{2}/(2\pi)]\alpha w_0/\sqrt{n} \approx 0.23 w_0/r_n$, where r_n is the radial span of the trap state n. Taking the typical atom to have an energy equivalent to 2kT for the trap in Fig. 5-7 we obtain $r_n \approx 150\mu m$, which results in a photoionization rate of $54s^{-1}$ for 3.3mW of incoming laser power. We then recall the discussion in Section 5.3 and use an effective beam waist that is a factor of 2 larger. This decreases the intensity by 4 and increase the waist by two resulting in a decrease by two of the photoionization rate, i.e., $\gamma_{pi}(3.3mW) \approx 27s^{-1}$. This very rough estimate is in perfect agreement with the data point at 3.3mW in Fig. 5-7.

Again, instead of trying to fully characterize this problem, we postpone it until the laser frequency jitter problem is solved. Then one should be able to study the loss rates for different velocity classes of atoms. Such an experiment is potentially powerful. Using this technique, one may be able to study the kinetics of repopulation of low energy states, for instance. One may also be able to analyse the feasibility for two-photon laser induced evaporation.

5.7 Comments on Count Rate and Signal to Noise Ratio - Towards an Optical Frequency Standard

The signal to noise ratio in our initial scans was dominated by the detector dark count and by problems with the counters. After improving the counting electronics and using a higher counting duty cycle (long excitation time for a short detection time) the detector dark count rate was brought down to neglegible levels, about few hundredths of a count per second of excitation time.

As discussed in Section 4.8.2, our fluorescence signal noise is dominated by counting shot noise, laser power and alignment fluctuations, and frequency jitter. For a one second integration time we have typically observed between 40 to 1000 counts at the line peak (the higher count rates are obtained as we approach the conditions for BEC, low temperatures and high densities). For these counts the fractional shot noise would be 16 to 3% of the signal. With the laser power controlled we may have variations of 1% in power which would add a noise of 2% in the signal. Alignment variations have been estimated in Section 5.3 and should typically contribute about 4% under the present conditions. The laser frequency jitter of about 2 kHz, in spectral linewidths of less than 5 kHz, is by far the dominant source of noise in our high count rate scans.

Our detection efficiency could be improved by three orders of magnitude with a redesign of the experiment. At count rates approaching $10^5 s^{-1}$, with sub-kHz resolu-

tion, if systematics can be held below 10 Hz, the spectroscopy of trapped hydrogen

should provide one of the best fractional accuracies of the known frequency standards.

Chapter 6

Conclusion and Suggestions

This work opens a new window through which we can "see" cold hydrogen atoms held in a magnetic trap. We can observe them oscillating in the trap and cause them to jump a few energy levels. We can choose to interact with the fast atoms or the slow ones. We can measure their collective temperature down to $200\mu K$ or even inquire about the lack of a temperature. We can measure their lifetime when in the excited state under no light or we can observe the excited state decay under light. We also believe that we could see 10^7 or more of these atoms sharing a single state, in a Bose condensate.

While we have superficially explored these new frontiers, a few improvements in the theory that we have developed and in the experimental setup should allow precise measurements and an in depth study of many of the phenomena discussed throughout this thesis, especially in Chapter 5.

6.1 Improvements on the Experiment

Most of the urgently needed experimental improvements were discussed in Chapter 3 and 5. They are basically three: laser frequency stability, detection efficiency and atom loss by He vapour. For the laser frequency stability, one should be able to obtain an order of magnitude improvement by relocating and better isolating the reference cavity and by cancelling the Doppler shift between the laser and the atoms with a servo system. The easiest gain on the detection efficiency, without redesigning the cell and trap, is to electronically switch the MCP gain on and off. By switching the MCP, one could replace the L_α filter by a MgF_2 window, therefore increasing the detection efficiency by at least 6. Improvements by a factor of 20 in the detection efficiency may be possible by placing an aluminum coated L_α mirror in the cell or by turning the cell walls into a L_α reflector. One has to address possible implications to the loading of the trap and evaporation, due to the superconductivity of Al below the critical field, before embracing such idea. For solving the atom loss problem, we advocate using a surface-node high-reflector mirror inside the cell as discussed in Chapter 4.

Besides these improvements related to the optical experiment there are fundamental questions on loading and evaporative cooling in our setup that need to be addressed. While the improved optical setup should provide excellent diagnostics, a few changes in the cell-discharge-film pump lines system may provide quicker answers. Whether or not we obtain better loads of the trap, we are very close to the conditions for Bose-Einstein condensation and a careful search for the transition should be pursued.

6.2   Possible Extensions to the Theory

For the trap oscillations spectra there are questions that were not addressed. What is the spectrum when the laser beam is off-centered? When does the selection rule change from jumping a multiple of two trap states to being able to jump one trap state? Can we use the spectrum to center the laser beam with respect to the trap? What is the expected spectrum for an actual, not harmonic, trap shape?

When one considers a more general trap shape, the following suggestion may help computing the frequency spacing. One can calculate the oscillation frequency (Ω_{osc}) to go across the trap for a given energy by integrating the period. Then I claim that the level spacing at that energy is simply $\hbar \times \Omega_{osc}$. This is probably equivalent to the WKB approximation, but in this case the knowledge of the energies of the levels is unimportant and so are the wavefunctions. All one cares about is the local, energetically speaking, level spacing.

Jamieson, Dalgarno and Doyle[15] predict a shift in the 1S-2S transition frequency that is dependent on the local density due to 2S-1S elastic collisions. If we verify this theory or measure a different shift, it would be interesting to incorporate this effect into the lineshape calculation since it may induce line asymmetries.

Saturation and photoionization remain to be fully accounted for in a thermal spectrum. We also have not computed a spectrum due to Bose-Einstein statistics above the transition line. The reason for choosing the Boltzmann distribution is that it is separable in all dimensions, i.e., $exp(-\beta E) = exp(-\beta E_x) \times exp(-\beta E_y)...)$, while the Bose-Einstein distribution is not. We also do not expect much difference between

the two results unless one is already in the quantum regime $n\lambda^3_{deBroglie} \approx 1$, i.e., quite close to BEC.

Some of these question are not urgent but others are important for the accurate measurement of the transition frequency.

Bibliography

[1] T.J.Greytak and D. Kleppner, "Lectures on Spin-Polarized Hydrogen", in *New Trends in Atomic Physics - Les Houches*, G.Grynberg and R.Stora, eds. (North-Holland,Amsterdan,1984)

[2] I.F. Silvera and J.T.M.Walraven, in *Progress in Low Temperature Physics*, D.Brewer, Ed. (North-Holland, Amsterdan,1986), vol.10, Chap.D.

[3] T.J.Greytak, Bose-Einstein Condensation, A.Griffin, D.W.Snoke, R.Stringari, Eds. (Camb.U.Press,1995), p.131

[4] Proceedings of the Fifth Symposium on Frequency Standards and Metrology, Woods Hole, october 1995, in print

[5] D.J.Berkeland, et al., PRL **75**, 2470 (1995)

[6] M.Weitz, et al., PRL **72**, 328 (1994)

[7] K.Pachucki, Phys. Rev. A **52**, 1079 (1995)

[8] M.H.Anderson, J.R.Ensher, M.R.Matthews, C.E.Wienman, and E.A.Cornell, Science **269**, 198 (1995)

[9] C.C.Bradley, C.A.Sackett, J.J.Tollett, and R.G.Hulet, PRL **75**, 1687, (1995)

[10] K.Davis et al., PRL **75**, 3969, (1995)

[11] J. Doyle, MIT thesis (1991), unpublished

[12] W.Stwalley and L.Nosanow, PRL **36**, 910 (1976)

[13] H.Hess, PRB **34**,3476 (1986)

[14] D. Pritchard, PRL **51**,1336 (1986)

[15] Jamieson, Dalgarno and J.Doyle, preprint (1995)

[16] For a general idea of the field see the special issue "Laser Cooling and Trapping of Atoms", JOSA B **6** (1989); and "Laser Manipulation of Atoms and Ions : Varenna on Lake Como", E.Arimondo, W.D.Phillips and F. Strumia, eds. (North-Holland, Amsterdan, 1992)

[17] F. Diedrich, J. Bergquist, W. Itano, and D. Wineland, PRL **62**,403 (1989)

[18] C.Monroe, D.Meekhof, B.King, S.Jefferts, W. Itano, D. Wineland, and P.Gould, PRL **75**,4011 (1995)

[19] C. Bordé, C.R.Acad.Sc.Paris, t.282 (1976)

[20] F. Biraben, M. Bassini and B. Cagnac, J.Physique **40**,445 (1979)

[21] A. Yariv, "Quantum Electronics", Wiley

[22] see for instance: C. Cohen-Tannoudji, J. Dupont-Roc and G. Grynberg, "Atom-photon interactions", Wiley

[23] H.Bethe and E. Salpeter, "Quantum Mechanics of One- and Two-Electron Atoms", Plenum/Rosetta

[24] V.P.Chebotaev, Proceedings of the International School of Physics "Enrico Fermi", T.W.Hansch and M.Inguscio Eds., Varenna on Lake Commo, Italy,1992; North=Holland (1994)in *High Resolution Spectroscopy*

[25] C.Zimmermann, R.Kallenbach, and T.W.Hansch, PRL **65**, 571(1990)

[26] G. Arfken, "Mathematical methods for physicists", Academic Press

[27] F. Bassani, J Forney and A. Quattropani, PRL **39**,1070, (1977)

[28] J. Sandberg, MIT thesis (1993), unpublished

[29] B.Sviatunov and G.Shlyapnikov, Sov. Phys. JEPT **70**, 460 (1990)

[30] H.D.Politzer, PRA **43**, 6444 (1991)

[31] J.Javanainen, PRL **72**, 2375 (1994)

[32] J.Javanainen, PRL **72**, 2375 (1994)

[33] Li You, et al., PRL **50**, R3566 (1994)

[34] Li You, et al., PRL **50**, R3566 (1994)

[35] O. Morice, Y. Castin, and J.Dalibard, PRA **51**, 3896 (1995)

[36] S. Klarsfeld, Phys.Lett. **30A**,382 (1969)

[37] J.H.Tung, et. al., PRA **30**, 1175 (1984)

[38] I. Cirac, talk at Workshop on Quantum Field Theory of Cold Atoms, JILA, Boulder, Colorado (1994), unpublished

[39] J.Dalibard, talk at the Research Conference on Bose-Einstein Condensation, Strasbourg, France(1995), unpublished

[40] T.Hijmans, et al., in Bose-Einstein Condensation, A.Griffin, D.W.Snoke, R.Stringari, Eds. (Camb.U.Press,1995)

[41] R. Beausoleil, PhD thesis, Stanford University (1986), unplublished

[42] H.Stoof, et al., PRB **38**, 4688 (1988)

[43] I.Albert Yu, MIT PhD thesis (1993), unpublished

[44] Coherent Laser Products Division; Palo Alto, California

[45] Our source of Coumarin 102 is Exciton, Inc.; Dayton, Ohio

[46] G.Bjorklund, Opt. Lett. **5**, 15 (1980)

[47] D.McIntyre, PhD thesis, Stanford University (1987), unpublished

[48] J.D.Gillaspy and C.J.Sansonetti, JOSA B **8** 2414 (1991)

[49] T.W.Hansch and B.Couillaud, Opt. Commun. **35** 441 (1980)

[50] Galileo Electro-Optics Co.; Sturbridge, Massachusetts

[51] J.Cariou and P.Luc, *Atlas du Spectre d'Absorption de Molecule Tellure* (Laboratoire Aime-Cotton, CNRS UU, Orsay, France, 1980)

[52] A. Folch, C.Peters, J.Tejada, and M.Wrighton, "Electron beam deposition of gold nanostructures in a reactive environment", Appl. Phys. Lett. **66**, 2080 (1995)

[53] D.Fried, et al., to be published

[54] D.Bitko, MIT undergraduate thesis (1990), unpublished

[55] Acton Research Co., Acton, Massachusetts

[56] Opthos Instruments, Inc; Rockville, Maryland

[57] Hamamatsu Co., Bridgewater, New Jersey

[58] T.Killian, Private Communication

[59] UDT Sensors, Inc.; Hawthorne, California

[60] We got the substrate from Precision Optical, Costa Mesa, California; and had it coated at Lambda Research Optics, Santa Fe Springs, California

[61] EDO Corp., Salt Lake City, Utah

[62] Minicircuits, Brooklyn, New York

[63] Precision Monolithics Inc., Santa Clara, California

[64] M.Abramowitz and I.A.Stegun, Handbook of Mathematical Fucntions, Dover, New York, 1970

[65] I.Setija, et al., PRL **12**, 2257 (1993)

[66] D.Pritchard, et al., Proceedings of the Eleventh ICAP, S.Haroche, J.Gay, and G.Grynberg(World Scientific, Singapore, 1989)